XE/D_2 CROSS SECTION RATIO FROM MUON SCATTERING AT 490 GEV/C

Stephen Magill, Ph.D.
Department of Physics
University of Illinois at Chicago
Chicago, Illinois (1990)

The ratio of cross sections for inelastic muon scattering from nucleons in xenon and "free" nucleons (in deuterium) was studied in the region of low x_{Bj} ($0.001 < x_{Bj} < 0.2$) for Q^2 values of $0.1\ (GeV/c)^2 < Q^2 \leq 40\ (GeV/c)^2$.

Corrections were made for trigger acceptance, scattered muon reconstruction efficiency, the non-isoscalarity of the xenon target, empty target event subtraction, and radiative corrections. The separation of the radiative background from inelastic scattered events was accomplished using 3 independent methods - restricted kinematic cuts, a calorimeter energy cut, and calculation of the radiative contributions to the measured cross section using standard quantum electrodynamic theory. These 3 methods yielded results which were consistent well within the statistical errors reported for the analysis.

The ratio of cross sections was determined as a function of x_{Bj}, Q^2, and ν. The ratio dependence on x_{Bj} and ν shows shadowing at low x_{Bj} and over the entire range of ν. These results can not distinguish between the two general types of models used to explain the shadowing phenomenon - vector dominance models (including generalized vector dominance) and parton (including QCD) models. However, the Q^2 dependence of the ratio indicates that where shadowing exists in the low x_{Bj} region, the Q^2 dependence is flat, supporting a parton model (or QCD) approach to explain the shadowing phenomenon.

XE/D_2 CROSS SECTION RATIO
FROM
MUON SCATTERING AT 490 GEV/C

BY

STEPHEN MAGILL
B.S., University of Maryland, 1976
M.S., DePaul University, 1979

THESIS

Submitted as partial fulfillment of the requirements
for the degree of Doctor of Philosophy in Physics
in the Graduate College of the
University of Illinois at Chicago, 1990

Chicago, Illinois

ACKNOWLEDGEMENT

I would like to thank the members of my thesis committee; Professor Mark Adams, Professor Clive Halliwell, Professor Donald McLeod, and Professor Uday Sukhatme, of the University of Illinois at Chicago; and Dr. Jorge Morfin of the Fermi National Accelerator Laboratory; for their time spent reviewing this thesis and their helpful comments which have been incorporated.

I would especially like to thank my advisor, Professor Clive Halliwell, for directing me to both software and hardware projects which kept me focussed on the steps necessary for bringing this analysis to completion. Also, I am indebted to Professor Mark Adams for his willingness to include me in the development of the Small Angle Trigger, for his guidance in the design, construction, and testing of the PSA wire chamber, and for his help in characterizing and analyzing the data.

The first run of the E665 Muon Scattering Experiment at Fermilab was a success due to the hard work of the over 80 collaborators involved. The support of the Fermilab staff and postdocs was also invaluable to the experiment and especially to me personally. I am especially grateful for the chance I had to work with the dedicated group of fellow graduate students on this experiment. As we go our separate ways now, I know I can look forward to seeing all of you again in about 10 years in Texas!

Most importantly, I could not have done any of this work without the support of my wife Judy and my two children, Katie and Andrew. You were more important than you know for providing me with some balance while I was working on this experiment - Thanks, guys!

SRM

TABLE OF CONTENTS

CHAPTER PAGE

TABLE OF CONTENTS (continued)

CHAPTER PAGE

TABLE OF CONTENTS (continued)

LIST OF TABLES

LIST OF FIGURES

LIST OF FIGURES (continued)

FIGURE PAGE

LIST OF FIGURES (continued)

LIST OF FIGURES (continued)

FIGURE PAGE

LIST OF FIGURES (continued)

FIGURE PAGE

LIST OF FIGURES (continued)

FIGURE | PAGE

LIST OF ABBREVIATIONS

QCD	Quantum Chromodynamics
EMC	European Muon Collaboration
DIS	Deep Inelastic Scattering
RAM	Random Access Memory
QED	Quantum Electrodynamics
SLAC	Stanford Linear Accelerator Laboratory
FNAL	Fermi National Accelerator Laboratory
VMD	Vector Meson Dominance
GVMD	Generalized Vector Meson Dominance
CCM	Chicago Cyclotron Magnet
CVM	Cern Vertex Magnet
MWPC	Multi-wire Proportional Chamber
SAT	Small Angle Trigger
RF	Radio Frequency
TF	Track Fitting

SUMMARY

The ratio of cross sections for inelastic muon scattering from nucleons in xenon and "free" nucleons (in deuterium) was studied in the region of low x_{Bj} ($0.001 < x_{Bj} < 0.2$) for Q^2 values of $0.1\ (GeV/c)^2 < Q^2 \leq 40\ (GeV/c)^2$. The purpose of this study was to examine the effect on the structure of a nucleon in the low x_{Bj} region where the contribution to the scattering cross section comes mainly from the quarks and anti-quarks making up the parton sea. The phenomenon of "shadowing" (depletion in the cross section per nucleon in nuclei compared to the cross section per nucleon in a free nucleon) was observed as a function of the variables x_{Bj}, Q^2, and ν in order to distinguish between the many models which try to explain the origin of shadowing.

Shadowing is clearly observed as a strong function of x_{Bj} and as a somewhat weaker function of ν. Observed as a function of x_{Bj} or ν, the results of this analysis do not distinguish between the two general types of shadowing models - vector dominance models (including generalized vector dominance) and parton (including QCD) models. However, the Q^2 dependence of the ratio taken by restricting the x_{Bj} range indicates that where shadowing exists in the low x_{Bj} region, the Q^2 dependence is flat, supporting a parton model (or QCD) approach to explain the shadowing phenomenon. The range in the variable Q^2 was such that this dependence was observed over a total range an order of magnitude greater than any previous measurement.

1. INTRODUCTION

In the meson theory of nuclear interactions, the constituents of nuclei, protons and neutrons, are surrounded by clouds of virtual mesons which mediate the nuclear force between the nucleons. The mechanism is similar to the way in which the photon mediates the electromagnetic force between charged particles. The massive mesons, however, can only be exchanged over short distances of the order of the size of a nucleus, as opposed to the infinite extent of the electromagnetic force. It was this model which led to the search and eventual discovery of the pion as the candidate for the mediating meson.

As it became apparent that the nucleons were themselves made up of other particles, this relatively simple view of the nucleus needed revision, at least at the nucleon level. The Quark-Parton Model was introduced, which described nucleons and mesons in terms of their constituent partons or quarks as they eventually became known. To describe the interactions between quarks, the theory of Quantum Chromodynamics (QCD) was developed which included the gluon as the carrier of the "color" force mediating the quark interactions.

In order to more efficiently use the high-energy particle probes provided by accelerators such as the Tevatron at the Fermi National Accelerator Laboratory (FNAL), nuclear targets were used to provide the probe particle with many nucleons to study. However, the use of nuclear targets also yielded surprises such as the "EMC Effect", discovered in 1983 [10]. Comparison of muon scattering using nuclear targets (with their bound nucleons) to deuterium targets (in which the nucleons are essentially free), showed that the structure of the nucleon itself was different in these two cases. That there is such an effect is not unreasonable given that quarks associated with a nucleon in a nucleus are about the same distance apart as they are from quarks in a neighboring nucleon. Since the discovery of the EMC Effect, the number of models which attempt to explain the nuclear dependence of the quark distributions in nucleons has proliferated, as well as the detail in which the various effects are treated. It now seems apparent that a description of the nucleus in terms of the constituents of the nucleons themselves is necessary to explain the experimentally observed effects - a model of nuclear chromodynamics.

The purpose of this thesis is to report on research that compared the structure of nucleons in a heavy nucleus to free nucleons in order to help understand the nature of the observed differences. The kinematic region of interest for this analysis is commonly called the "low x_{Bj}" region, referring to the variable which describes the fraction of the nucleon's momentum carried by the parton involved in the scattering process.

1.1 Deep Inelastic Scattering

In order to observe the structure of a nucleon, a suitable probe is needed. A particularly good probe is the virtual photon produced by scattering a lepton from a nucleon or nuclear target. By varying the 4-momentum transfered to the target from the virtual photon, different kinematic regions of the target structure can be observed. Also, since the probe contains no inherent structure and is absorbed completely, there is no background in the event from the probe itself. Thus, lepton-induced Deep Inelastic Scattering (DIS) provides a clean, well-understood probe to observe the structure of the nucleon.

The most easily produced lepton, the electron, has been used to provide virtual photons, but has some disadvantages which limit its use :

- In order to probe the distances of < 1 *fermi* inside the nucleon, the 4-momentum transfer must be large. This requires a high energy beam of incident electrons which is hard to make due to the loss of energy in an electron beam by synchrotron radiation (energy loss $\propto (E^4/Rm_e{}^4)$ resulting from acceleration of the beam particles in a curved path. Thus, high energy electron beams must be produced in a linear accelarator ($R \rightarrow \infty$) to avoid this energy loss, and the cost and size of these devices limits their use.

- Electrons radiate photons when traveling through a dense medium. The deep inelastic scattering cross section of electrons incident on a nuclear target is very small compared to the cross section for an electron to radiate a photon ($d\sigma_{DIS} \propto 1/M_P E_e, d\sigma_{brems} \propto Z^2/Am_e{}^2$).

Both of these problems can be overcome by using leptons with higher mass, i.e., muons. High energy muons can be made by producing pions and kaons in high energy proton - nucleus interactions and allowing them to decay weakly ($\pi \rightarrow \mu\nu, k \rightarrow \mu\nu$, etc.) into muons. The resulting muons can be formed into a beam which typically lasts for many kilometers ($\sim$ 3000 km for a 500 GeV/c muon). The principle of muon - electron universality (electrons and muons participate in electromagnetic interactions in identical ways except for their masses), has been verified in many experiments and is now accepted as a fundamental principle.

The lowest order (in $\alpha_{em} \equiv e^2/\hbar c$) process describing deep inelastic scattering is shown in Figure 1.1, and is used to define the kinematic variables used in this analysis. The leptonic (muon) vertex of this single virtual photon exchange diagram is described exactly by the theory of Quantum Electrodynamics (QED) and contains all of the information needed to predict the cross sections in the inclusive process $\mu N \rightarrow \mu X$.

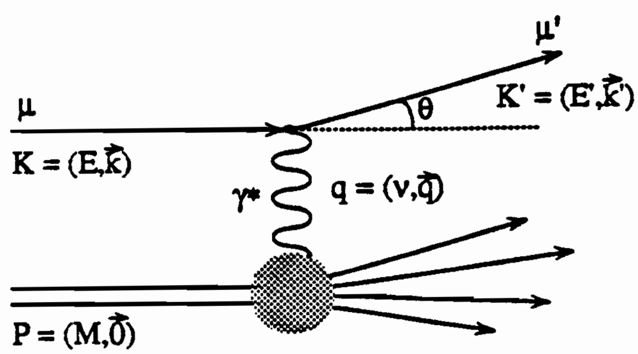

Figure 1.1: Single virtual photon exchange Feynman diagram for deep inelastic muon scattering.

The quantities E and $\vec{k}$ in Figure 1.1 refer to the incident muon energy and 3-momentum respectively, with its 4-momentum given by $K = (E, \vec{k})$. Likewise, the scattered muon 4-vector is denoted by $K' = (E', \vec{k'})$ where again E' refers to its energy and $\vec{k'}$ to its 3-momentum. The

Lorentz-invariant quantities Q^2 and ν are defined as :

$$Q^2 = -q^2 = -(K - K')^2 = -2m_\mu{}^2 + 2EE' - 2\vec{k}\vec{k'}cos\theta \tag{1.1}$$

$$\nu = E - E' \tag{1.2}$$

where θ is the angle of the scattered muon with respect to the incident muon as measured in the lab frame and m_μ is the muon rest mass. It is convenient to define dimensionless variables :

$$x = \frac{Q^2}{2M\nu} \tag{1.3}$$

$$y = \frac{\nu}{E} \tag{1.4}$$

in terms of the kinematic variables of the muon vertex. The 4-vector of the target nucleon is given by $P = (M, 0)$ in the lab frame where the target is at rest, and the invariant mass of the hadronic final state is given by :

$$W^2 = (P + q)^2 = M^2 - Q^2 + 2M\nu \tag{1.5}$$

A kinematic map of the $Q^2 - x$ plane is shown in Figure 1.2 with some lines of constant θ, $y = \nu/E$, and W overlayed.

The line defined by $W^2 = M^2$ and $Q^2 = 2M\nu$, or $x = 1$, represents elastic scattering of the muon from a nucleon. In the region where $Q^2 < 2M\nu$, or $x < 1$, some of the energy lost by the incident muon is used to break up the target nucleon, defining the inelastic scattering process. The limits of acceptance of a deep inelastic scattering experiment are determined by the kinematic constraints of $y, x \leq 1$ and in practice by the resolution limits imposed by the detector geometry on the variables Q^2, ν, and x.

Using the diagram of Figure 1.1, an expression for the double differential cross section can be written as :

$$\frac{d^2\sigma}{dQ^2 d\nu} = \frac{4\pi\alpha^2}{Q^4}\frac{E'}{E}L_{\mu\nu}W^{\mu\nu} \tag{1.6}$$

where $L_{\mu\nu}$ denotes the electromagnetic current at the top (leptonic) vertex and $W^{\mu\nu}$ the current at the bottom (hadronic) vertex. The value of the electromagnetic current, $L_{\mu\nu}$, is described

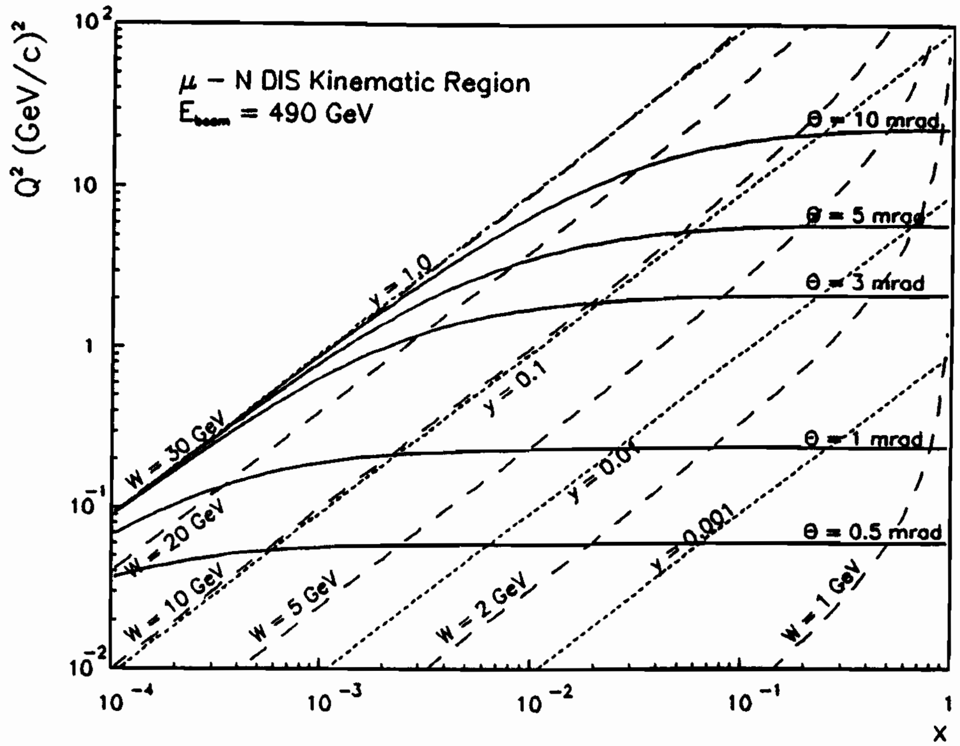

Figure 1.2: Kinematic region in the $Q^2 - x$ plane defining the deep inelastic scattering process.

exactly using QED and when averaged over initial state spins and summed over final state spins is given by :

$$L_{\mu\nu} = 2\left(k'_\mu k_\nu + k_\nu k'_\mu + \frac{q^2}{2} g_{\mu\nu}\right) \tag{1.7}$$

Since the exact form of the hadronic current is not known, the following most general form can be constructed :

$$W^{\mu\nu} = -W_1 g^{\mu\nu} + \frac{W_2}{M^2} p^\mu p^\nu + \frac{W_3}{M^2}(p^\mu q^\nu - q^\mu p^\nu) + \frac{W_4}{M^2} q^\mu q^\nu + \frac{W_5}{M^2}(p^\mu q^\nu + q^\mu p^\nu) \tag{1.8}$$

The W_3 term represents a contribution to the scattering from the parity-violating weak interaction and, therefore, does not contribute to the cross section involving only the electromagnetic interaction. By requiring gauge invariance, the hadronic tensor $W^{\mu\nu}$ can be written in terms of just two structure functions, W_1 and W_2 as :

$$W^{\mu\nu} = W_1\left(-g^{\mu\nu} + \frac{q^\mu q^\nu}{q^2}\right) + \frac{W_2}{M^2}\left(p^\mu - \frac{p \cdot q}{q^2} q^\mu\right)\left(p^\nu - \frac{p \cdot q}{q^2} q^\nu\right) \tag{1.9}$$

Contracting with the leptonic tensor, the double differential cross section becomes :

$$\frac{d^2\sigma}{dQ^2d\nu} = \frac{4\pi\alpha^2}{Q^4}\frac{E'}{E}\left[2W_1(\nu,Q^2)sin^2\frac{\theta}{2} + W_2(\nu,Q^2)cos^2\frac{\theta}{2}\right] \tag{1.10}$$

The two structure functions, W_1 and W_2, contain all of the information about the structure of the target nucleon.

An alternative viewpoint is to consider the deep inelastic scattering as an interaction between a beam of virtual photons and the target. The cross section for absorption of the virtual photon can be written in terms of its polarization states - transverse (helicity = ± 1) and longitudinal (helicity = 0). The double differential cross section can be written as :

$$\frac{d^2\sigma}{dQ^2d\nu} = \Gamma(\sigma_T(Q^2,\nu) + \varepsilon\sigma_L(Q^2,\nu)) \tag{1.11}$$

where σ_T and σ_L are the contribution to the total cross section from transverse and longitudinally polarized photons respectively. The parameter Γ is the flux factor for transverse photons and is given by :

$$\Gamma = \frac{\alpha}{2\pi}\frac{K}{Q^2E^2}\frac{1}{(1-\varepsilon)} \tag{1.12}$$

where the polarization parameter ε is given by :

$$\varepsilon = \left[1 + 2\left(1 + \frac{\nu^2}{Q^2}\right)tan^2\left(\frac{\theta}{2}\right)\right]^{-1} \tag{1.13}$$

The energy (K) required to produce a final state with invariant mass W is defined as $K = (W^2 - M^2)/2M$. For real photons, $K = \nu$, and for virtual photons, $K = \nu + (q^2/2M)$. By comparing (1.10) and (1.11), the structure functions, W_1 and W_2, can be written in terms of σ_T and σ_L as :

$$W_1 = \frac{K}{4\pi\alpha^2}\sigma_T \ , \ W_2 = \frac{K}{4\pi\alpha^2}\left[\frac{Q^2}{Q^2+\nu^2}\right](\sigma_L + \sigma_T) \tag{1.14}$$

The ratio of longitudinal to transverse cross sections is given by :

$$R(Q^2,\nu) = \frac{\sigma_L(Q^2,\nu)}{\sigma_T(Q^2,\nu)} = \frac{W_2}{W_1}\left(1 + \frac{\nu^2}{Q^2}\right) - 1 \tag{1.15}$$

Objects with spin $\frac{1}{2}$ can only absorb transverse photons ($\sigma_L = 0$), which leads to $R(Q^2,\nu) = 0$. In contrast, spin 0 objects can not absorb transverse photons ($\sigma_T = 0$), leading to $R(Q^2,\nu) = \infty$.

For virtual photons with small wavelengths, i.e. large Q^2, the cross section (1.10) behaves like elastic scattering from spin $\frac{1}{2}$ point particles. The structure functions can then be written as :

$$2mW_1(\nu, Q^2) = \frac{Q^2}{2m\nu}\delta\left(1 - \frac{Q^2}{2m\nu}\right) \tag{1.16}$$

$$\nu W_2 = \delta\left(1 - \frac{Q^2}{2m\nu}\right) \tag{1.17}$$

where m is the mass of the point-like scatterer. Bjorken [18, 19] showed that in the kinematic limit $Q^2 \to \infty$ and $\nu \to \infty$, the structure functions are no longer separately dependent on Q^2 and ν, but instead become functions of the finite dimensionless variable $Q^2/2M\nu$ where M is the mass of the nucleon. The structure functions W_1 and W_2 can then be rewritten in terms of the scaling variable as :

$$MW_1(\nu, Q^2) \to F_1\left(\frac{Q^2}{2M\nu}\right) \tag{1.18}$$

$$\nu W_2(\nu, Q^2) \to F_2\left(\frac{Q^2}{2M\nu}\right) \tag{1.19}$$

Note that by defining the variable x in terms of the nucleon mass M instead of m (the mass of the point-like constituent), the relationship between x and the elastic scattering limit ($Q^2 = 2m\nu$) is now $x = m/M$. The scattering object can be viewed as providing a fraction x of the nucleon's mass. This variable, now called x_{Bj}, the Bjorken scaling variable, displays no inherent physical scale, such as mass or length. That Bjorken scaling holds (approximately) was demonstrated by experiments at the Stanford Linear Accelerator Laboratory (SLAC) [20, 21], and it was found that the scaling behavior was valid even down to $Q^2 \simeq 1\ (GeV/c)^2$. Therefore, the constituents of the nucleon, called partons by Feynman [35], appeared to be point-like, spin $\frac{1}{2}$ particles, and eventually came to be known as quarks [39].

The scaling variable, x_{Bj}, takes on added significance when the deep inelastic scattering is viewed in a frame of reference in which the target nucleon has very large momentum. The deep inelastic scattering interaction in this frame, called the infinite momentum frame, is shown in Figure 1.3.

When a quark of momentum xP absorbs the virtual photon with momentum q, conservation

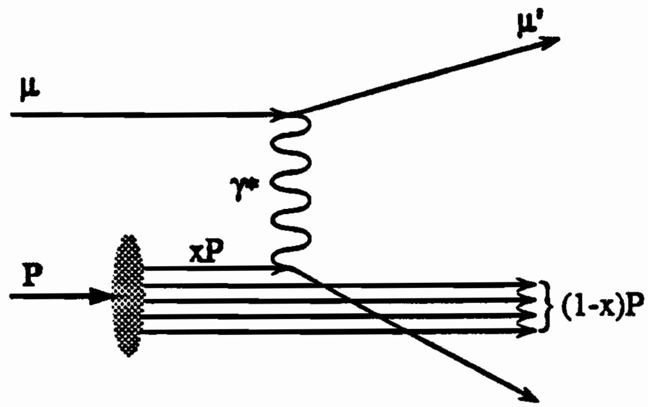

Figure 1.3: Feynman diagram for deep inelastic scattering in the infinite momentum frame of reference.

of energy and momentum requires :

$$(xP + q)^2 = m^2 \tag{1.20}$$

where m is the mass of the struck quark. Solving (1.20) for x, the fractional value of the nucleon momentum becomes :

$$x = \frac{q \cdot q}{2P \cdot q} = \frac{Q^2}{2M\nu} \equiv x_{Bj} \tag{1.21}$$

if $Q^2 \gg m^2, x^2P^2$. Therefore, the scaling variable, x_{Bj}, is equivalent to the fraction of momentum carried by the struck quark at sufficiently high Q^2. This understanding of the role of the quarks in the deep inelastic scattering process forms the basis of the Quark-Parton Model. In terms of the quark constituents of the nucleon, the structure functions in (1.18) and (1.19) can be written as :

$$F_1(x) = \frac{1}{2}\sum_i q_i(x){e_i}^2 \tag{1.22}$$

$$F_2(x) = \sum_i x q_i(x){e_i}^2 \tag{1.23}$$

where $\sum_i$ is the sum of all quark flavors, ${e_i}^2$ is the charge of the quark, and $q_i(x)$ is the probability for quark i to have momentum fraction x. Comparing (1.22) and (1.23) yields the relation :

$$2xF_1(x) = F_2(x) \tag{1.24}$$

which is called the Callan-Gross relation and is a consequence of the quarks having spin $\frac{1}{2}$.

The structure of the proton is viewed as being made up of 3 valence quarks surrounded by a sea of quark - anti-quark pairs. In addition, the carrier of the "color" force which binds quarks in nucleons, the gluon, is also present, accounting for the $\sim$ 50% of the total momentum fraction not seen in the quark and anti-quark distributions. The individual quark and gluon structure functions $xq_i(x)$ and $xg(x)$, can be extracted from deep inelastic scattering data. Figure 1.4 shows the results for the quark and antiquark structure functions inside a proton as a function of x_{Bj} obtained from the global fit of Morfin and Tung [50]. These are also shown arranged as valence quark and sea quark structure functions with the gluon distribution superimposed.

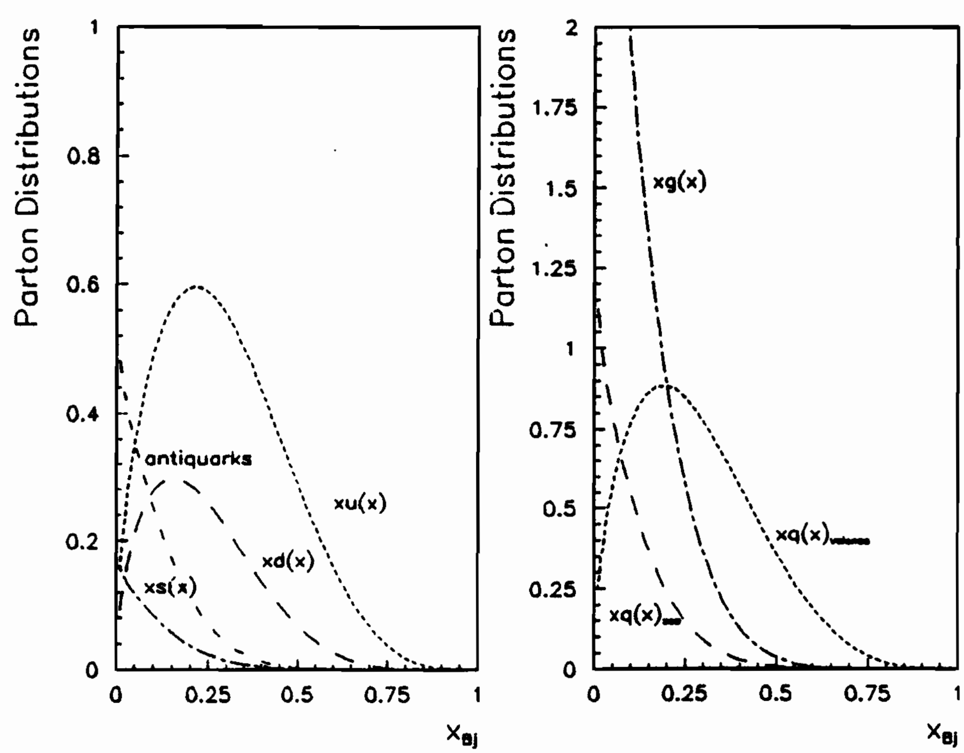

Figure 1.4: Parton structure functions as a function of x_{Bj}. Figure a shows the quark and anti-quark distributions in a proton, and Figure b shows the parton structure functions according to type - valence, sea, and gluon.

The success of the Quark-Parton Model in explaining some of the gross features of nucleon structure was followed very shortly by the observation that its fundamental principle, Bjorken

Scaling, while approximately true, was not perfect. Experimental evidence showed a small Q^2 dependence ($\propto logQ^2$) of the structure functions in addition to the observed dependence on x_{Bj}. Figure 1.5 shows evidence for Q^2 as well as x_{Bj} dependence in the structure function F_2 from several experiments as shown in reference [13].

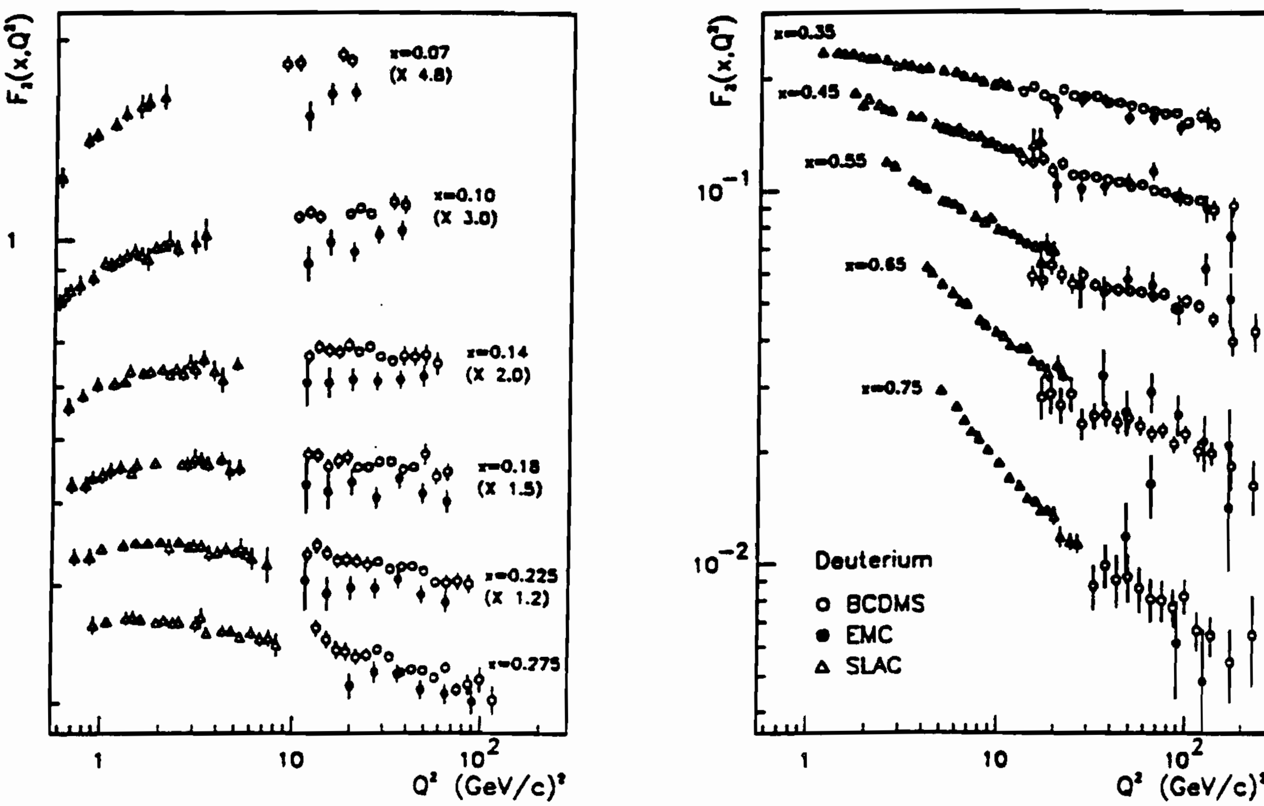

Figure 1.5: Q^2 and x_{Bj} dependence of F_2 as measured by the BCDMS Collaboration and compared to EMC and SLAC.

The theory of Quantum Chromodynamics so far offers the best explanation for the interactions of quarks and gluons in nucleons and explains the Q^2 dependence of the structure functions as well as other features not contained in the Quark-Parton Model. Including the additional Q^2 dependence, the deep inelastic scattering cross section (1.10) becomes :

$$\frac{d^2\sigma}{dQ^2dx} = \frac{4\pi\alpha^2}{Q^4}\left[y^2F_1(x,Q^2) + (1-y)\frac{F_2(x,Q^2)}{x}\right] \tag{1.25}$$

where $y = \nu/E$, $cos^2\frac{\theta}{2} \simeq 1$, $d\nu/\nu = dx/x$, and the structure functions F_1 and F_2 have been written to include both x and Q^2 dependence. Using (1.15), (1.18), and (1.19), R can be written in terms of x and Q^2 as :

$$R(x,Q^2) \equiv \frac{\sigma_L}{\sigma_T} = \frac{(1+\frac{4M^2x^2}{Q^2})F_2(x,Q^2) - 2xF_1(x,Q^2)}{2xF_1(x,Q^2)} \tag{1.26}$$

The differential cross section can now be written in terms of the two structure functions F_2 and R as :

$$\frac{d^2\sigma}{dxdy} = \frac{4\pi\alpha^2}{Q^4}2ME\left[1-y+\frac{y^2}{2(1+R(x,Q^2))}\right]F_2(x,Q^2) \tag{1.27}$$

The structure function $R(x,Q^2)$ has been measured and found to grow as x_{Bj} [13] and Q^2 [30] decrease as shown in Figure 1.6.

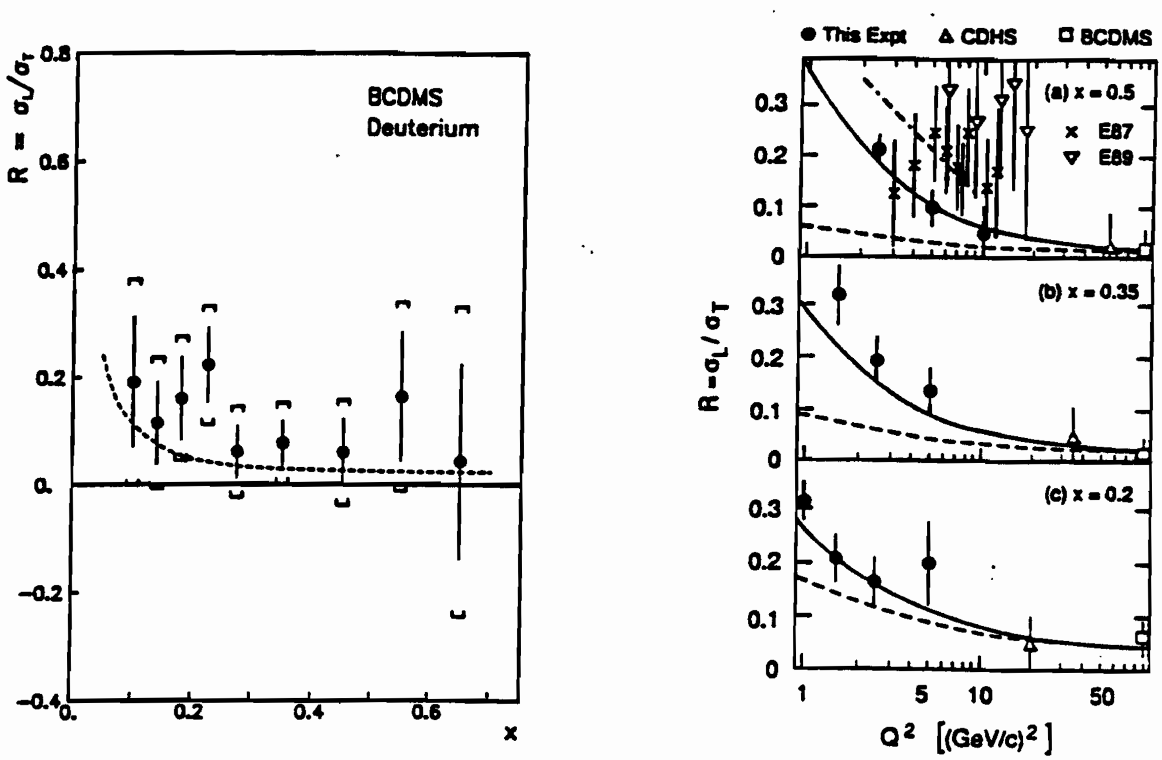

Figure 1.6: x_{Bj} and Q^2 dependence of $R = \sigma_L/\sigma_T$ as measured by the BCDMS and SLAC E140 Collaborations.

It is predicted by QCD that R should increase as x_{Bj} and Q^2 decrease, but the observed growth is larger than the prediction. The top curve on Figure 1.6b is generated by including additional target mass contributions to the QCD calculation. The fact that $R(x,Q^2) > 0$ at low x_{Bj} and Q^2 indicates that the cross section includes a longitudinal component, or that scattering is occuring from spin 0 (composite) objects inside the nucleon. A model of scattering and structure at low x_{Bj} and low Q^2 is needed to understand the presence of composite objects inside the nucleon.

1.2 Lepton-Nucleon Scattering at Low x_{Bj}

The emphasis will now switch to regions where the value of x_{Bj} is very small, i.e., the virtual photon is absorbed by a constituent of the nucleon which carries a small fraction of the nucleon's total momentum. For an experiment such as E665, with a fixed beam momentum distribution and limits on the momentum resolution of the scattered muon, lower x_{Bj} values also imply lower Q^2. Therefore, the following discussion of low x_{Bj} scattering processes will include and sometimes be dominated by the effects of scattering at low Q^2 (and high ν) as well.

Strictly speaking, the equivalence of the defined parameter $x \equiv Q^2/2M\nu$ and the fraction of the momentum carried by the struck object in the nucleon x_{Bj}, is only valid when $Q^2 \gg x^2M^2$. Figure 1.7 shows the difference between the parameter x and x_{Bj} as a function of Q^2 for constant x values.

Since, for the kinematic range of this analysis the maximum fractional difference between x and x_{Bj} is $< 0.5\%$, the variable x will be referred to as x_{Bj}.

Using the uncertainty principle, a physical picture of the scattering region can be constructed as a function of x_{Bj} and Q^2. In the infinite momentum frame, where x_{Bj} represents the fraction of momentum carried by the struck object, the uncertainty principle yields an estimate of the longitudinal (along the momentum axis) extent of the scattering process since $\Delta x_{Bj}P \cdot \Delta l \simeq \hbar$. It must be remembered that in this frame, the longitudinal size (z_n) of the nucleon is Lorentz contracted by an amount $\sim M/P$ where M is the mass of the nucleon and P its momentum. Figure 1.8 shows $\Delta l/z_n$ as a function of x_{Bj}.

The 4-momentum transfer, Q, can be related to the transverse size of the scattering region since $Q^2 = -(K - K')^2$, which defines the perpendicular component of momentum produced in the scattering process. Using the uncertainty relation, the transverse size of the scattering region is given by $\Delta Q \cdot \Delta r \simeq \hbar$, where Δr is plotted versus Q^2 in Figure 1.9.

It can be seen that at low x_{Bj}, scattering occurs from sea quarks (and indirectly from gluons)

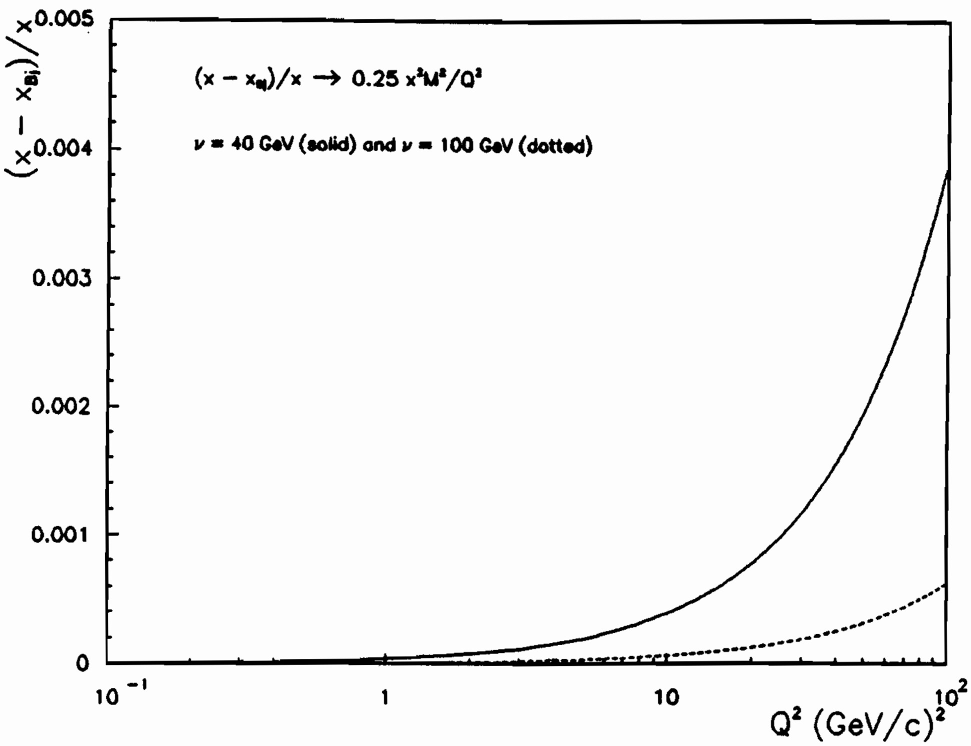

Figure 1.7: Difference between x and x_{Bj} as a function of Q^2 for various ν values. The plot shows the maximum difference (at $\nu = 40\ GeV$) for the x and Q^2 range of this analysis.

since the valence quark distribution is very small in the low x_{Bj} region. The sea quark and gluon distributions grow very large ($\propto 1/x_{Bj}$) as $x_{Bj} \rightarrow 0$. At a fixed, high Q^2 ($Q^2 > 1\ (GeV/c)^2$), low x_{Bj} scattering implies hard scattering from the small momentum fraction components of the nucleon, i.e., the quarks and anti-quarks in the sea. In other words, the virtual photon is able to resolve the cloud of quarks and anti-quarks present in the nucleon since $1/Q$ is small. For the low x_{Bj} events used in this analysis, the transverse size is somewhat smaller than the size of a nucleon ($\Delta r \sim 1.2$ *fermi* at $Q^2 = 0.1\ (GeV/c)^2$). However, the longitudinal size of this region, which is $\propto 1/x_{Bj}P$, is much larger than a nucleon size ($\Delta l/z_n \sim 100$). Therefore, the virtual photon can not resolve individual quarks in the nucleon. This means that the scattering center may be a composite structure, i.e., the pion cloud surrounding the nucleon. This is also indicated by the Q^2 and x_{Bj} dependence of $R = \sigma_L/\sigma_T$ described in Section 1.1, which would

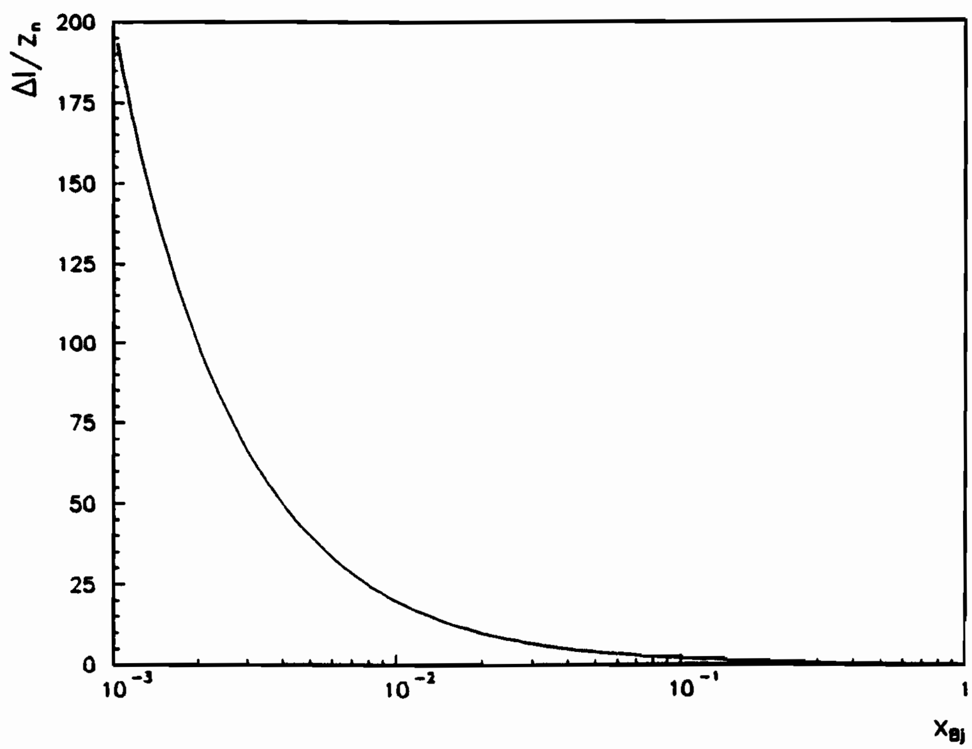

Figure 1.8: Longitudinal extent of parton distributions as a function of x_{Bj} compared to the Lorentz-contracted nucleon size.

suggest that scattering occurs from spin 0 objects at low x_{Bj} and low Q^2.

As a final summary of muon - nucleon scattering at low x_{Bj}, a model put forth by Gribov et al. [42], is described here. At high x_{Bj} and high Q^2, the virtual photon "sees" a distribution of essentially free partons which look like point particles. This has been likened to particles in the gas phase and called a quark gas. At low x_{Bj} and low Q^2, the partons appear "swollen", and crowd the space in the nucleon. This is analogous to a liquid state and therefore Gribov et al. call this phase state the region of quark liquid. The main feature of the quark liquid is the process of recombination, i.e., interactions among partons so as to reduce their total number. The parton distributions in a nucleon at low x_{Bj} are thus modified. This is expected to occur in nuclei also, as will be explained later, and is the mechanism that leads to the prediction of shadowing.

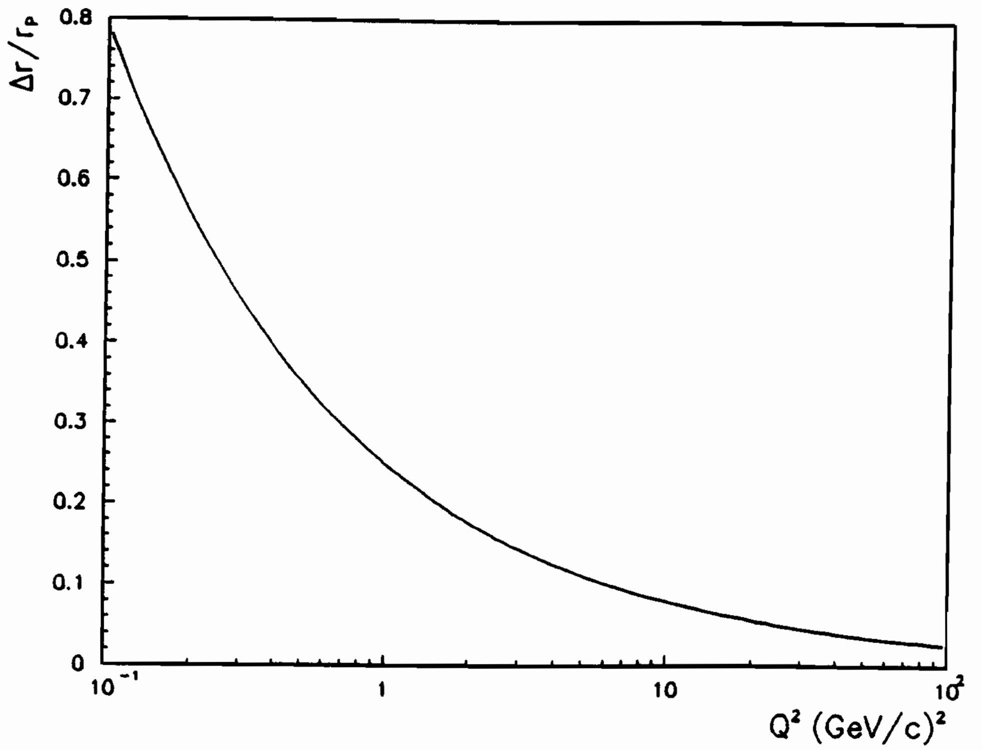

Figure 1.9: Transverse size of the scattering region as a function of Q^2 compared to the radius of the proton charge distribution.

1.3 Lepton-Nucleus Scattering at Low x_{Bj}

Now the emphasis will switch to scattering from nuclear targets instead of nucleons. The most striking feature seen in the comparison of scattering from bound nucleons to free nucleons is the phenomenon called "Shadowing". Although this term was originally used to describe a specific model dependent process seen in hadron - nuclear scattering, it is now used to describe the general phenomenon of a nuclear cross section being less than A times the corresponding cross section for nucleon scattering. It has been expressed as the ratio of cross sections per nucleon, $R = \sigma_A / A\sigma_N (\equiv A^{eff}/A)$, or as $\sigma_A = \sigma_N A^{\alpha}$, where σ_A is the cross section for nuclear scattering, σ_N is the cross section for nucleon scattering, and A^{α} is the atomic mass number for the nucleus raised to the power α with $\alpha < 1$ implying shadowing and $\alpha = 1$ implying no shadowing. Also, the case where $\alpha > 1$ has been studied, and this is referred to as "anti-shadowing". From now on, the depletion of the nuclear cross section compared to A times the nucleon cross section will be referred to as shadowing.

Shadowing was predicted in 1967 [57] in the context of vector meson dominance (specifically ρ dominance). This approach will be discussed, along with more recent models based on generalized vector dominance and the parton model.

1.3.1 Vector Meson Dominance Picture

At high energy, electromagnetic interactions involving real or virtual photons display some properties similar to hadronic interactions. This has been studied in many experiments [41]. The scale of the electromagnetic cross section is smaller than that for hadronic interactions by the factor α_{em}, but the exchange of a photon or a hadron with the same quantum numbers as a photon has the same energy dependence and momentum transfer dependence. The Vector Meson Dominance (VMD) Model, with its many variations, takes into account the hadronic structure of the photon. In this model, the structure of the physical (real or virtual) photon is shown in Figure 1.10.

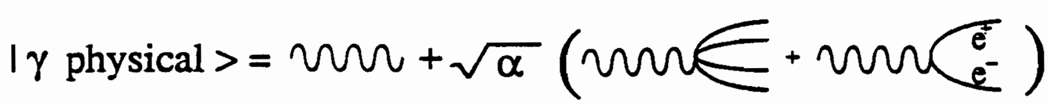

Figure 1.10: Photon structure amplitudes.

The dominance of the hadronic structure of the photon results from the observation that if the e^+e^- state interacts, an additional $\sqrt{\alpha_{em}}$ is required as opposed to an $\sqrt{\alpha_S}$ for the hadronic interaction. The modification to the basic deep inelastic scattering diagram for the case of the hadronic component of the virtual photon is shown in Figure 1.11.

Stodolsky [57] predicted that the total nuclear cross section would be smaller than A times the nucleon cross section by assuming that photon - nuclear interactions at high energy are actually dominated by interactions of the nuclear targets with vector mesons (ρ, ω, and ϕ). The photon - nucleus scattering amplitude is determined by considering its two dominant terms :

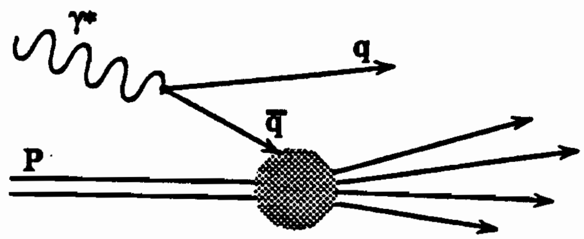

Figure 1.11: Feynman diagram for deep inelastic scattering in the Vector Meson Dominance picture.

1. A one-step Compton scatter of a bare photon in the nucleus.

2. A two-step scatter which starts with the transformation of the photon into a vector meson on one nucleon scattering center, the propagation of the meson through the nucleus, and the transformation back to a photon on a second nucleon.

While the one-step process by itself yields a cross section dependence proportional to A, the nuclear volume, inclusion of the two-step cross section introduces a term which interferes directly to cancel the one-step contribution, leaving only a term proportional to $A^{2/3}$, or the nuclear cross sectional area. Therefore, Stodolsky predicted that the total nuclear cross section would have an A-dependence which would be in the range $A^{2/3} < A^{\alpha} < A$. The term "shadowing" was used since the photon only "sees" nucleons on the surface of the nucleus; interior nucleons remain in the "shadow" of the surface nucleons and are not seen.

The picture of shadowing in the vector dominance model depends on the relative sizes of 3 characteristic lengths :

1. The nuclear radius - given by $R = r_0 A^{1/3}$, with $r_0 = 1.12$ *fermi*.

2. The mean free path for a hadron through nuclear matter. This is given by $\lambda = 1/n\sigma_{hN}$, where n is the nuclear density ($n = 0.17$ $fermi^{-3}$), and σ_{hN} is the hadron - nucleon cross section ($\sigma_{\rho N} = 25$ mb). Therefore, the mean free path of ρ mesons through nuclear matter is $\lambda = 2.4$ *fermi*.

3. The fluctuation distance d for a real or virtual photon to be in a hadronic state. This is determined by applying the uncertainty principle assuming that the photon momentum is large. The relationship becomes $d \simeq \Delta t = \hbar/\Delta E$, where ΔE is the energy difference between the hadron energy $\sqrt{\nu_2 + m_v{}^2 + Q^2}$ where m_v is the mass of the vector meson and the photon energy ν. This yields $d = .4\nu/(Q^2 + m_v{}^2)$ where d is in units of $fermi$ for ν, Q, and m_v in GeV.

The necessary condition for shadowing to occur in this geometrical description of the interaction processes is :

$$d \gg R > \lambda \tag{1.28}$$

This condition ensures that the hadronic state exists for a long enough time for it to extend well beyond the size of a nucleus, and that when it does exist, it remains inside the nucleus long enough to be absorbed in the interaction. For this analysis, the values of the 3 characteristic lengths are $d \sim 2 \rightarrow 1200\ fermi$, $R = 5.6\ fermi$ for xenon, and $\lambda = 2.4\ fermi$ for ρ mesons. Therefore, the condition (1.28) is satisfied for high ν and low Q^2 events in the xenon data, or in the language of the parton model, low x_{Bj}. It can be seen that the fluctuation distance is dependent on $1/Q^2$, and so in the vector dominance picture, the shadowing condition (1.28) goes away as Q^2 increases. Furthermore, this diminishing of shadowing should occur at Q^2 values of $\sim 1\ (GeV/c)^2$ (for $m_v < 1\ GeV$), since $d \simeq R$ above this value.

In addition to this simple picture of vector dominance in which the dominant effects are seen through photon fluctuations into ρ mesons which then interact as $\rho N \rightarrow \rho N$, similar models classified as generalized vector meson dominance (GVMD) models [16, 17, 56] have been developed which allow higher mass vector mesons (diagonal GVMD) as well as interactions of the form $\rho N \rightarrow \omega N$, for example (off-diagonal GVMD). The same geometrical considerations apply in these models, but with the increased mass term in the denominator of the fluctuation distance d, the "turn-off"of shadowing as a function of Q^2 is somewhat diminished.

1.3.2 Quark-Parton Model and Quantum Chromodynamics

Presently, our understanding of the internal structure of nucleons is expressed in the theory of Quantum Chromodynamics. This model includes the "color" force as the strong interaction between quarks - the partons of the Quark-Parton Model. The carrier of this force is the gluon. Since the constituent gluons account for about half of the nucleon's momentum, they may play a major role in the interactions of nucleons inside a nucleus. This is especially true since the internuclear spacing of nucleons in a nucleus is of the same order as the size of the nucleon itself. Therefore gluons and quarks of one nucleon may actually find themselves closer to the gluons and quarks of a different nucleon than the one they originally belonged to. Models have been developed to describe the interactions of these gluons and quarks which lead to modified parton distributions for nucleons inside nuclei.

The first suggestion that shadowing could be due to nucleon parton distributions was made by Nicolaev and Zakharov [52]. They suggested that because of the large longitudinal distances involved in low x_{Bj} interactions (see Section 1.2), the partons of one nucleon are actually closer to the partons from other nucleons in a nucleus. Interactions between partons, or "parton fusion", result in a depletion of low x_{Bj} partons and an enhancement of those at medium x_{Bj}. The enhancement is a result of parton sum rules requiring momentum conservation in the structure function (or total parton) distribution. This assumes no exchange of momentum between quarks and gluons (gluons were not considered by these authors), which was shown to be true much later by others [28]. At x_{Bj} values < 0.1, the cross section for scattering is a tube which extends across nucleons (and nuclei), resulting in a cross section proportional to $A^{2/3}$ (surface interactions). Therefore, this model predicts shadowing at low x_{Bj} which is in qualitative agreement with the vector dominance models, but, in addition, it also predicts anti-shadowing at intermediate x_{Bj} as a result of momentum conservation of partons.

This model has been expanded to include gluons and quantified by many authors [51, 53, 14, 22, 25, 26, 29, 36, 59]. In particular, Mueller and Qiu [51] have developed the parton recombination model extensively, including modifications to the Altarelli-Parisi evolution equations which make possible quantitative predictions of the x_{Bj} and Q^2 dependence (as well as A dependence) of shadowing.

The basic idea of parton recombination, or fusion, has been used by many authors; it was first expressed in quantitative form by Mueller and Qiu. As in the Nicolaev and Zakharov approach, low x_{Bj} partons recombine because they occupy the same space according to the uncertainty principle. The recombination of partons begins as soon as the x_{Bj} value is low enough to allow partons from different nucleons to overlap spatially, i.e. when $\Delta l > z_n$ (see Section 1.2). Qiu [53] used the mass and radius of a nucleon to determine Δl and therefore determined that the onset of shadowing should be A independent, and should occur at $x_{Bj} \simeq 0.1$. In collaboration with Berger [14], however, Qiu obtained an A-dependent expression for the x_{Bj} value of the onset of shadowing by including a change in the nucleon separation by an amount proportional to the nuclear radius (or $A^{1/3}$). The result was a dependence which showed a slight increase in the x_{Bj} of the onset of shadowing with A. In addition, the uncertainty principle was used to predict the x_{Bj} value at which shadowing should saturate, i.e., the cross section ratio would reach a minimum value. This value was given by $x_{Bj} = .2/(2mR_A)$, where m is the nucleon mass, and R_A is the nuclear radius. That saturation should occur seems reasonable, since at this point, the parton overlap is total and no more recombination can occur by lowering x_{Bj}.

Parton recombination at low x_{Bj} modifies F_2 in nuclei by the 4 processes shown in Figure 1.12.

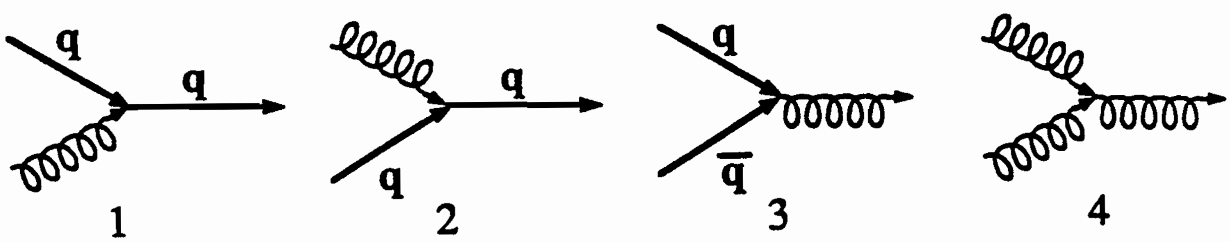

Figure 1.12: Parton recombination diagrams contributing to the modification of parton distributions in bound nucleons.

These processes are characterized by :

1. Gluons "leaking" from one nucleon to another and being absorbed by quarks. The quark distribution at all x_{Bj} is boosted in momentum fraction. This leads to a a slight enhance-

ment of F_2 in nuclei at all x_{Bj}.

2. Quarks leaking from one nucleon to another and being boosted to higher x_{Bj} values by absorption of gluons, again leading to a slight enhancement of F_2 in nuclei at all x_{Bj}.

3. Quarks(antiquarks) leaking from one nucleon to another and annihilating with an antiquark(quark), thus reducing the quark and antiquark content in nuclei at all x_{Bj}. The quarks which leak are predominantly sea quarks with low x_{Bj} values, which, because of the uncertainty principle, are more likely to overlap another nucleon's sea. This results in a depletion at low x_{Bj} values.

4. Gluons from different nucleons interacting, forming a resultant gluon with a higher momentum fraction. This results in a depletion of low x_{Bj} gluons.

According to Qiu, the first 3 contributions will always result in a net enhancement of F_2 at all x_{Bj}, or anti-shadowing. However, the gluon distribution itself is modified by both 1) and 2); and also by the 4) gluon - gluon fusion term which dominates the modification of the overall gluon distribution. The net result for the gluon distribution of nucleons in nuclei is that it is highly depleted at low x_{Bj}, which means that the sea quark distribution is reduced as well in this range since the gluons are the source of the sea. Therefore, when the reduction of sea quarks caused by the depletion in the gluon distribution is included in the calculation of F_2, the net result is shadowing at low x_{Bj}.

As in the vector dominance models, an important element in the shadowing picture is the Q^2 dependence. Qiu [53] states that if shadowing occurs at some x_{Bj} value, then it will always be there, independent of Q^2. This is because of the above mentioned gluon recombination mechanism - the depletion caused by gluon - gluon fusion is always present at low x_{Bj}, and since the growth of the gluon distribution as a function of Q^2 occurs at the same rate independent of its starting point ${Q_0}^2$, there will always be a depletion at $Q^2 > {Q_0}^2$ if there was one at ${Q_0}^2$. According to Qiu, gluons "remember" recombination effects occuring at low x_{Bj} for all Q^2. For example, if shadowing is observed in the ratio of two nuclei at some x_{Bj} and Q^2 value, evolving to higher Q^2 at the same x_{Bj} value will result in an increase in the number of gluons in both nuclei, but the relative value will not change because the slopes of the two evolution curves are the same. Therefore, this mechanism predicts a flat Q^2 dependence for shadowing - very different from the prediction of vector dominance models.

In the first parton model description of shadowing by Nicolaev and Zakharov described previously, momentum conservation of quarks was implicitly assumed. The argument was that since momentum must be conserved, if shadowing was present in one x_{Bj} region (i.e. a depletion of low x_{Bj} quarks), there must be a corresponding increase somewhere else - or anti-shadowing. Close et al. [28] show that even when including gluons, the total momentum fraction carried by quarks (and anti-quarks) is conserved in the quark distributions, while the gluons conserve their fraction separately as well. The authors find that the maximum amount of momentum sharing between quarks and gluons is $< 0.1\%$.

In summary, the quark and gluon recombination models which have sprung from the early Quark-Parton Model and more recently the theory of QCD are able to predict the presence of shadowing at low x_{Bj} with anti-shadowing at higher x_{Bj} (parton model including quarks only). This, in itself, does not distinguish these types of descriptions from those of vector meson dominance, however, the Q^2 dependence of shadowing in the vector dominance models is much stronger in all cases than that from the QCD models which predict a very small Q^2 (or even flat Q^2) dependence of shadowing at fixed x_{Bj} values. The Q^2 dependence of shadowing will therefore be very crucial in the determination of the most likely model candidate for the shadowing explanation.

1.4 Experimental Evidence for Shadowing

Experiments in which shadowing has been observed have traditionally been classified into two types - those which use real photons as probes and those which use virtual photons (electron - nucleus and muon - nucleus deep inelastic scattering). Recently, results from a Drell-Yan experiment which can be interpreted as shadowing have been presented [5]. In this section, shadowing results from the various types of experiments will be shown.

1.4.1 Real Photon Shadowing

Several investigations of photon - nuclear interactions have been done [23, 24] and shadowing has been observed as a function of the photon energy. Figure 1.13 shows A^{eff}/A as a function of photon energy E_γ for carbon/deuterium and lead/deuterium ($45\ GeV < E_\gamma < 82\ GeV$) and for copper/deuterium ($20\ GeV < E_\gamma < 185\ GeV$).

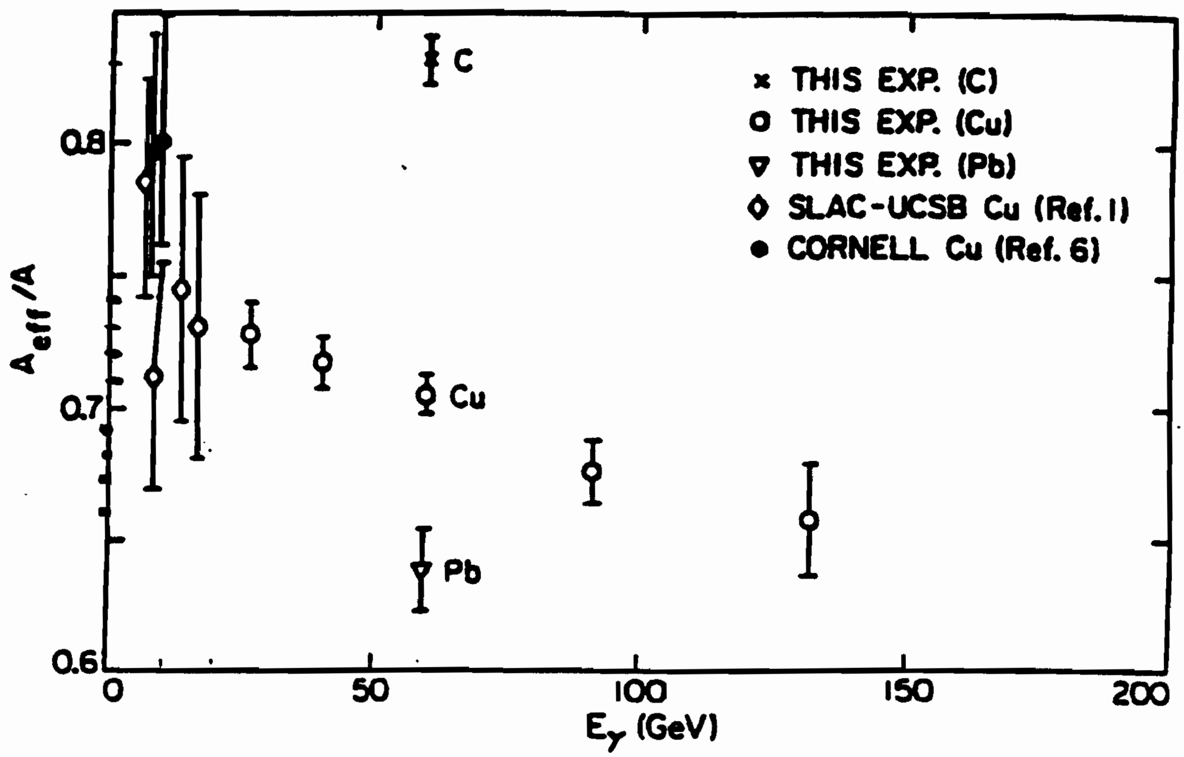

Figure 1.13: Shadowing in photon - nucleus interactions.

From the ν dependence of the Cu data, the authors [24] conclude that the naive vector dominance model (as well as VMD models including "near diagonal" terms) does not adequately explain their data, and that more complex off-diagonal GVMD models may be needed.

1.4.2 Virtual Photon Shadowing

The virtual photon group consists of deep inelastic lepto-production experiments using electrons [32, 33, 11, 37] or muons [45, 47, 40, 9, 6] to provide the virtual photon probe, and recently, results have been presented from Drell-Yan proton - nucleus interactions [5] which also show shadowing.

Shadowing in Deep Inelastic Scattering

The first experiment to investigate the nuclear effects in deep inelastic scattering was done at SLAC [32] in which beryllium, aluminum, copper, and gold targets were compared to deuterium, showing results consistent with no shadowing and very different from the real photon results. Later, additional results [33, 11, 37, 45] on a wide variety of nuclear targets (C, Al, Cu, Ta, Be, Co, Nb, U, Si, Sn, and Pb) seemed to indicate that shadowing occured for virtual photon scatters as well as for real photons. However, the evidence for shadowing from these early experiments was not as compelling as in the real photon results. The first unambiguous shadowing results came from two muon - nucleus scattering experiments [47, 40] on the nuclear targets carbon, aluminum, copper, tin, and lead. Figure 1.14 shows the results reported in reference [40] for carbon, copper, and lead.

Since the shadowing persists to high Q^2 values ($Q^2 > 5\ (GeV/c)^2$), these results were the first that were not consistent with a vector dominance model interpretation of shadowing.

More recently, the European Muon Collaboration (EMC) has studied shadowing in muon - nucleus deep inelastic scattering [9, 6] using the nuclear targets, carbon, calcium, and tin. The results of these experiments are shown in Figure 1.15.

Once again, shadowing persists to high Q^2 values ($Q^2 > 5\ (GeV/c)^2$ for the Sn data), favoring the parton model approach over the vector dominance model.

Shadowing in the Drell-Yan Process

One of the more recent experiments in which shadowing has been seen in nuclei is in dimuon production by the proton - nucleus Drell-Yan process. An experiment at FNAL [5] has studied the nuclear dependence in the Drell-Yan continuum region (dimuon mass range between the J/ψ and the Υ) for carbon, calcium, iron, and tungsten targets. Figure 1.16 shows the results of this experiment for the cross section ratios as a function of x_t, the fraction of target momentum carried by the struck quark - analogous to x_{Bj} in deep inelastic scattering.

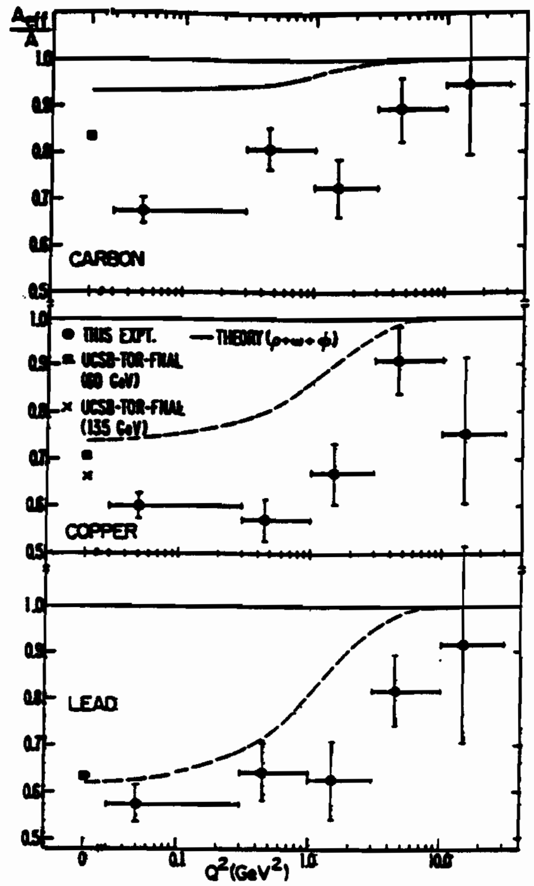

Figure 1.14: A^{eff}/A vs Q^2 for C, Cu, and Pb compared to D_2.

nuclei, but the mass range of the Drell-Yan results (analogous to Q in DIS) is much higher than that in the NA28 data which used some of the same targets.

The results shown here will be compared with the results from this analysis in Chapter 7.

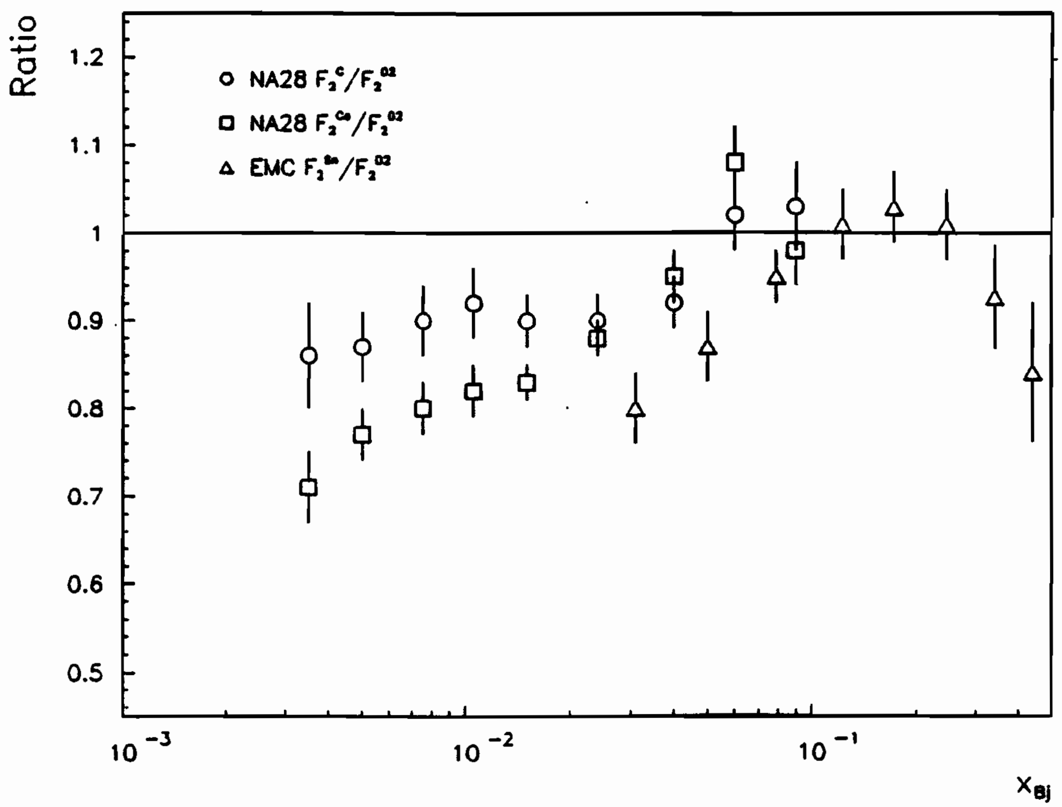

Figure 1.15: $F_2(A)/F_2(D)$ **results from EMC for various nuclei compared to** D_2.

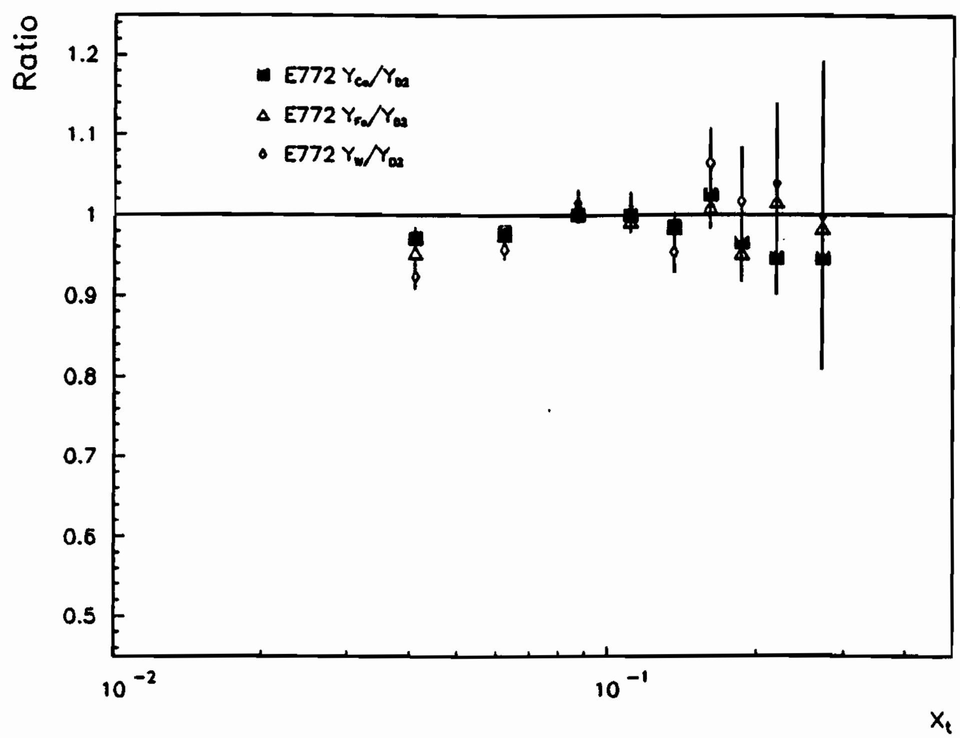

Figure 1.16: Event yields per nucleon in Drell-Yan dimuon production for various nuclei compared to D_2.

2. E665 MUON DEEP INELASTIC SCATTERING

The first run of the E665 Muon Scattering Experiment was part of the 1987-88 Fixed Target Experimental Program at FNAL. Protons for the fixed target experiments were available from approximately August 1987 to February 1988. Since this was the first run for the experiment, the commissioning of the apparatus and triggers took several months to complete. The bulk of the muon scattering data was taken between October 1987 and February 1988. For this analysis, however, the deuterium data was taken between December 1, 1987 and December 8, 1987; and the xenon data was taken between December 9, 1987 and January 7, 1988.

In this section, the parts of the apparatus used in this analysis are described. A more complete description of the entire apparatus and 1987-88 running configuration is contained in reference [1].

2.1 Fermi National Accelerator Laboratory Tevatron

The FNAL Tevatron delivered up to 1.8×10^{13} protons at 800 GeV/c to the secondary beam lines over a 20 *sec* spill period of which nominally 22% were allocated for the muon beamline. During normal fixed target operation, the spill cycle of the Tevatron was 1 spill per minute. The total number of protons accelerated during the 1987-88 run was 2.192×10^{18}. Figure 2.1 shows the arrangement of the fixed target experimental areas at the Tevatron.

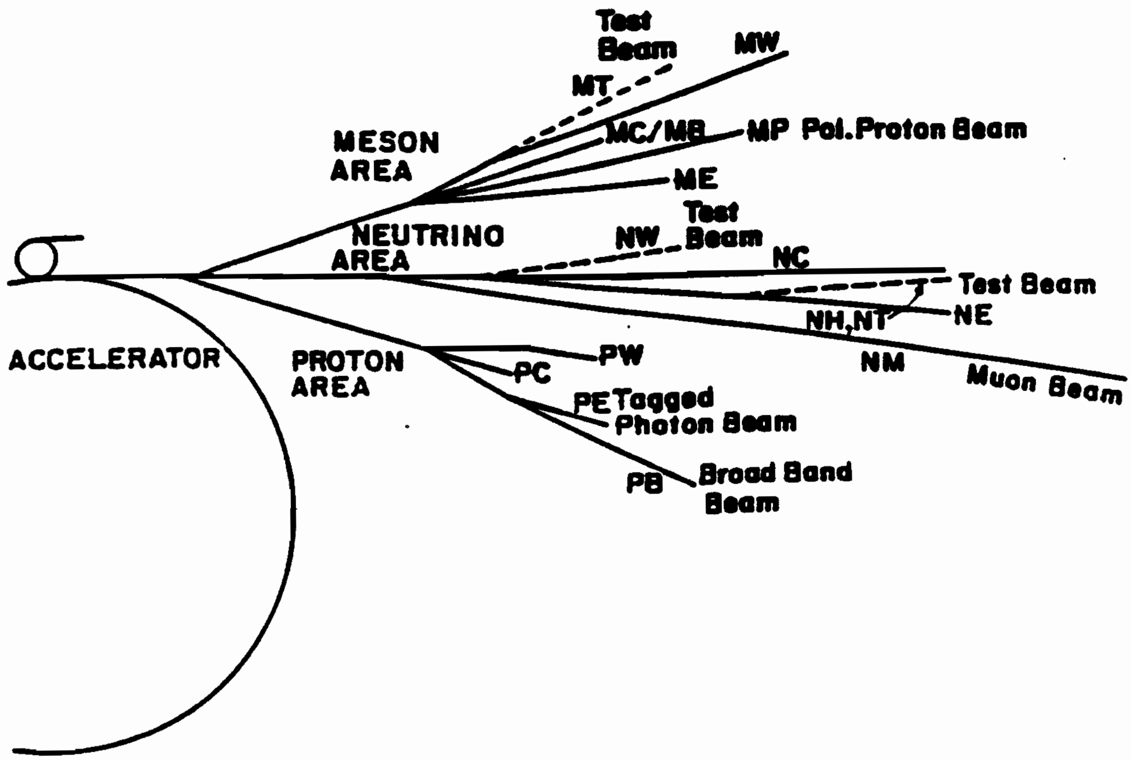

Figure 2.1: FNAL Tevatron and fixed target experimental area designations.

2.2 Muon Beamline

High energy muons for E665 were produced from the in-flight decays of pions and kaons resulting from proton - beryllium interactions. The design of the muon beam-forming apparatus and the muon production procedure are described in detail elsewhere [44]. A schematic diagram of the muon beamline (FNAL designation NM) is shown in Figure 2.2.

The key elements used in the production and transport of muons in this beamline are :

- a 48.5 cm primary interaction beryllium target for the 800 GeV/c protons from the accelerator,
- primary proton dumps to absorb non-interacting protons,
- a 1.1 km decay channel with alternating focussing and defocussing quadrupole magnets (Decay FODO),

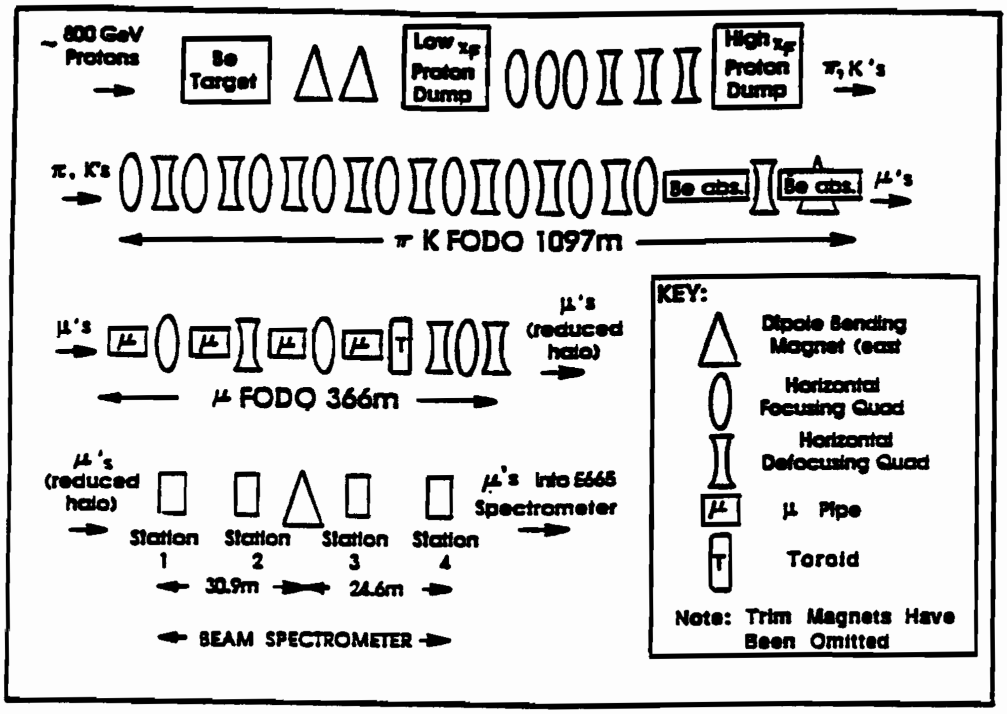

Figure 2.2: FNAL muon beamline schematic diagram.

- an 11 m beryllium absorber to absorb any hadrons left after traversing the Decay FODO,
- a 366 m Muon FODO channel including a total of 33 m of magnetized Mupipe around the beam and 15 m of toroids which steer the muon beam and reduce the halo (un-useable beam) content of the transported muons, and
- a 55 m beam spectrometer used to measure the momentum of individual beam muons.

The NM beamline was tuned to provide a high intensity, high momentum muon beam with a small halo contribution. By tuning the beamline elements, the muon/incident proton ratio (normally $\sim 0.5 \times 10^{-5}$) could be adjusted to provide as many as 3.5×10^{7} muons per 20 sec spill at $< P_\mu >= 490\ GeV/c$. The halo content was also minimized by tuning and normally made up less than 15% of the total beam intensity. Although it represented lost luminosity to the experiment, the halo muons were used to align some of the large wire chambers and to calibrate regions of the calorimeter not seen by the focussed beam. The NM beamline was also used during the run to produce and transport electrons and positrons which were used to measure the alignment properties and calibrate various components of the E665 Beam and Forward Spectrometers.

2.3 Local Coordinate System

The coordinate system for E665 was defined with the center of the Chicago Cyclotron Magnet (CCM) as the origin. The right-handed coordinate axes were chosen as; $\hat{X}$ along the beam direction which is approximately north, $\hat{Y}$ the horizontal axis with positive Y to the west, and $\hat{Z}$ the vertical axis with positive Z up. All of the magnetic fields are dipoles with the field in the $+\hat{Z}$ or $-\hat{Z}$ direction, thereby bending positively charged particles moving along the $+\hat{X}$ axis in the $-\hat{Y}$ or $+\hat{Y}$ direction respectively. The terms "upstream" and "downstream" refer to the negative X and positive X directions respectively.

2.4 Muon Beam Spectrometer

At the end of the NM beamline, a 4-station beam tagging spectrometer was used to define the beam portion of the trigger for the experiment [48]. It also measured the trajectory and momentum of individual incoming muons. Figure 2.3 shows the Beam Spectrometer arrangement of hodoscopes and wire chambers.

The 4 beam tagging stations were arranged around a central dipole bending magnet which produced a bend of 2.92 $mrad$ in the horizontal plane for a 500 GeV muon (corresponding to a transverse momentum kick of 1.46 GeV/c). Each beam tagging station consisted of segmented hodoscope planes (SBT's) for providing a fast signal to define the beam part of the trigger and multi-wire proportional chambers (PBT's) for reconstructing the beam muon track. The following section will describe these components and their performance during the run.

2.4.1 Beam Spectrometer Trigger Hodoscopes

As shown in Figure 2.3, each Beam Spectrometer station has a Y (bend-plane) view hodoscope plane and stations 1, 3, and 4 have Z (non-bend-plane) views. The size of the 13 individual counters in each plane was chosen so that the counting rate in each finger was approximately

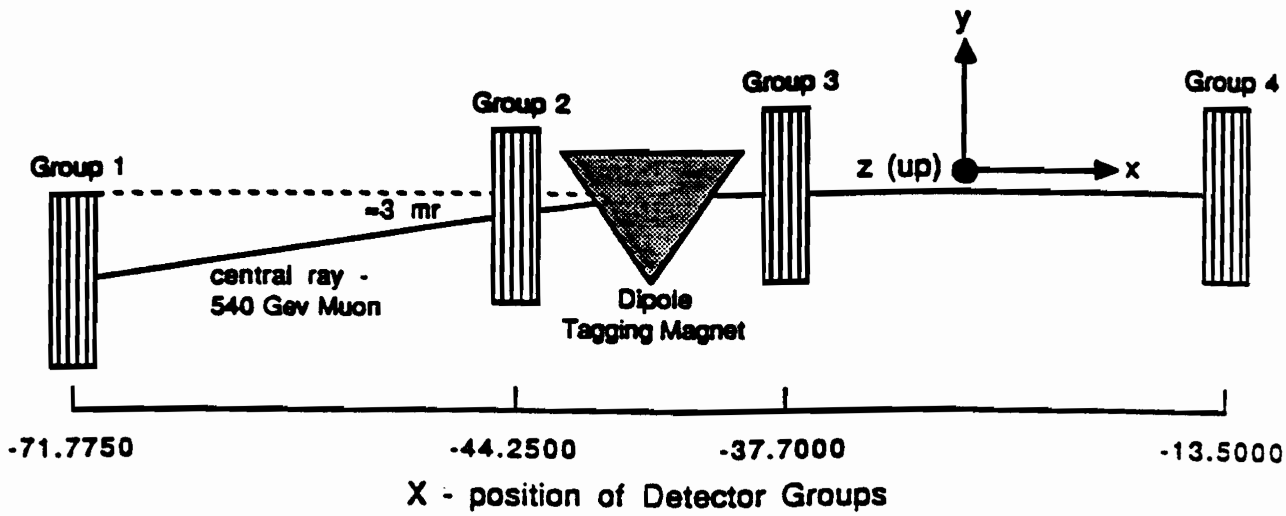

Figure 2.3: E665 muon beam tagging spectrometer configuration.

equal. This was not done for the Z view of station 1, which had 16 counters of equal size in order to accomodate the requirements of the E665 Small Angle Trigger (see Chapter 3). The active area defined by the coincidence of the two planes at each station (except, of course, station 2) was about 14 $cm \times 14$ cm. The 3.2 mm thick individual counters in each plane of each view were arranged in two overlapping layers. Alternating counters in each view had an overlap of 1.6 mm. Figure 2.4 shows the scintillator element configuration of a 13 counter hodoscope plane.

Although designed primarily to form a beam definition as input to the various E665 triggers, the SBT hodoscope signals were also latched and used to mask the hits on tracks found by the MWPC's in the Beam Spectrometer, thereby providing timing information on the beam tracks (see Section 4.1).

The efficiencies of the SBT hodoscopes were estimated to be $> 99\%$ for in-time beams.

2.4.2 Beam Tracking Multi-wire Proportional Chambers

The Beam Spectrometer PBT chambers were constructed from a standard FNAL design for beamline wire chambers [34]. Each of the 4 Beam Spectrometer stations contained 6 planes

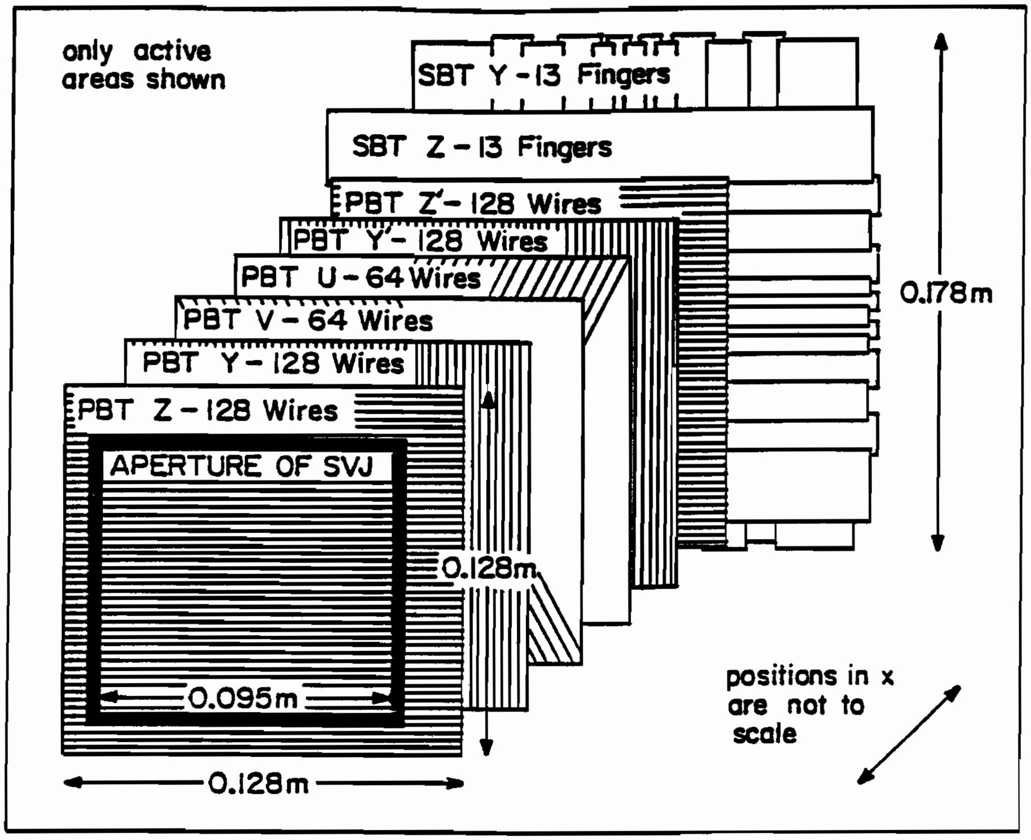

Figure 2.4: Scintillator hodoscope plane and wire chamber configuration for a beam tagging spectrometer station.

of MWPC's with 1 *mm* wire spacing and orientations U (+30° from vertical), Z, Y, V (−30° from vertical), Z' (0.5 *mm* nominal offset), and Y' (0.5 *mm* nominal offset). In addition to the scintillator counter configuration, Figure 2.4 shows an exploded view of the 6 PBT planes in each station.

Each of the Y view and Z view planes had 128 wires and each of the slant planes (U and V view) had 64 wires. The planes were arranged in two groups of 3 planes each with a Y, Z, and slant view in each 3-plane group. The active area of the combined 6-plane group was a diamond shape with a major axis of 12.8 *cm* in the vertical direction and a minor axis of 6.8 *cm* in the horizontal direction. The cathode planes were operated at +3.0 *kV* and the gas mixture used was a 50% argon - 50% ethane mix bubbled through ethanol at 0° C. Figure 2.5 shows typical wire maps of the Y and Z view PBT chambers at Beam Spectrometer station 4.

The efficiencies of the 24 individual PBT wire planes were measured and found to be

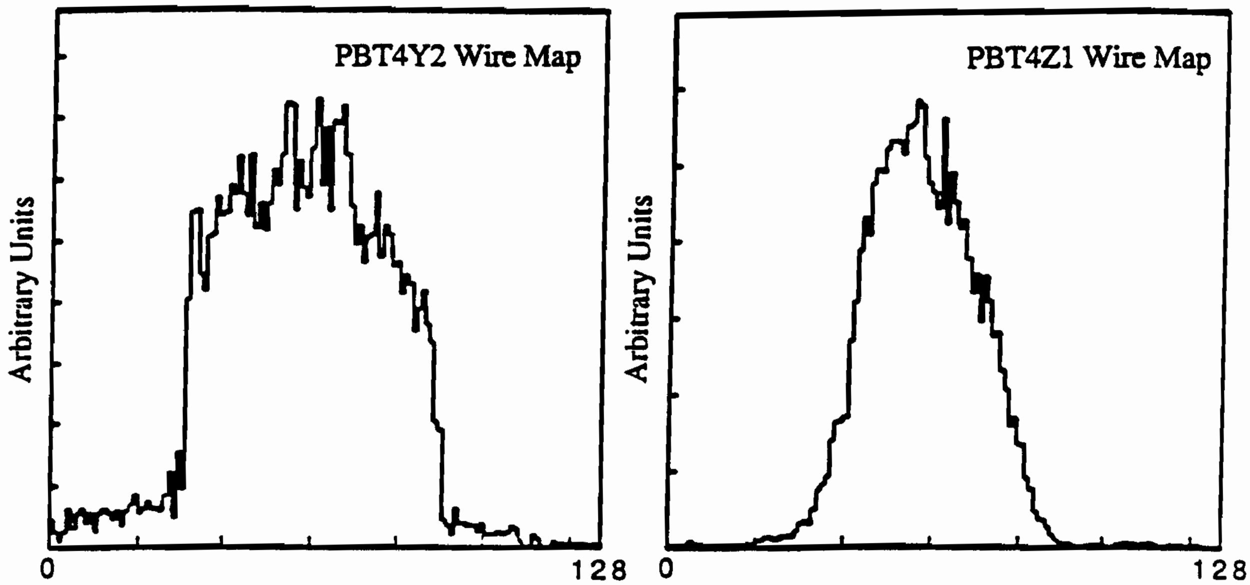

Figure 2.5: PBT Y and Z view wire maps at Station 4. This is the last beam spectrometer station and is closest to the target (~ 5 m upstream of the position of the center of the target).

constant during the majority of the 1987-88 run. The efficiencies varied from $\sim 50\%$ to $> 99\%$ for individual planes. Due to the redundancy of views and planes in each beam station package, however, the efficiency for forming a spacepoint from the individual wire plane hits was $> 98\%$ in each beam station for the entire run.

2.5 Deep Inelastic Scattering Targets

Data were taken using 3 different targets – xenon, deuterium, and hydrogen. The deuterium and hydrogen were in liquid form and used the same target vessel. The xenon was in high pressure gaseous form (~ 210 PSI) and, therefore, used a different target vessel. The target vessel parameters and target properties are shown in Table I.

The length of the target vessels was limited by the size of the streamer chamber enclosure to be ~ 1 m for both vessels. In addition, the high electric field environment of the streamer

TABLE I: E665 TARGET PROPERTIES

Target	Z/A	Length (cm)	Diameter (cm)	Thickness (g/cm^2)	L/L_R	X/X_N
Xe	54/131.3	113	7.1	8.5	1.00	0.05
D_2	1/2.0	115	8.9	16.0	0.13	0.29
H_2	1/1.0	115	8.9	7.0	0.11	0.14

chamber constrained the choice of target materials to be non-metallic. The amount of xenon was limited by the strength of the target vessel and the radiation length fraction presented to the beam. Note that the xenon target represented ~ 1 full radiation length. The limitation on the amount of deuterium and hydrogen was determined by the size of the target vessel. Also, since one of the major goals of E665 was to study the final-state hadrons, the nuclear interaction length fraction (X/X_N) of the targets was kept small so as to minimize interactions of these hadrons in the target. Note that this fraction for all of the targets was less than 0.30.

For the source of "free" nucleons, the deuterium target was used, since the neutron and proton are loosely bound with a binding energy of 2.22 MeV. Each nucleon actually has about the same probability of being outside (unbound) the potential well as inside (bound). With a binding energy of $\sim$ 8.5 $MeV/nucleon$, the xenon target provided a source of bound nucleons.

In addition to the data taken with the target vessels full of their respective material, empty target data for both the xenon target vessel and the deuterium/hydrogen target vessel were taken. In this way, effects of the target material present in the ends of the target could be subtracted from the final data sample.

2.6 Forward Spectrometer

The Forward Spectrometer consisted of two large superconducting dipole magnets (designated CVM - Cern Vertex Magnet, and CCM - Chicago Cyclotron Magnet, reflecting their respective origins) to provide momentum analysis of charged particles with momentum > 10 GeV/c in the forward direction ($x_F > 0$) and to form a favorable geometric condition for triggering on the scattered muon. The following section will describe the Forward Spectrometer as it was used in this configuration, with emphasis on the the tracking chambers used for reconstruction of the scattered muon track. Figure 2.6 shows the plan view of the E665 Forward Spectrometer.

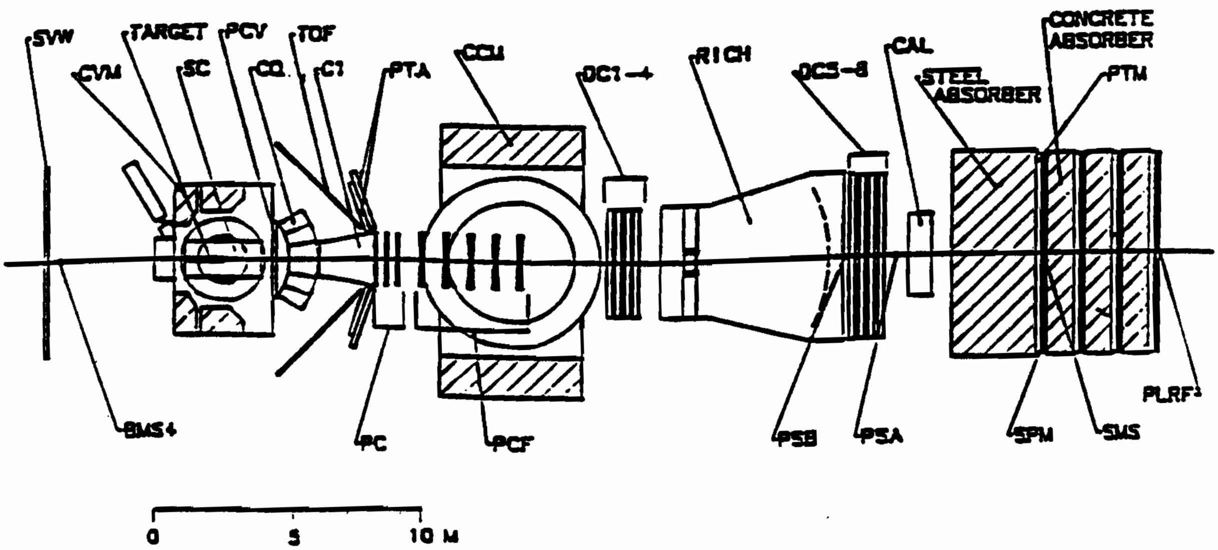

Figure 2.6: E665 Forward Spectrometer plan view.

2.6.1 Double Dipole Spectrometer Configuration

As mentioned above, the two superconducting dipole magnets provided for a high resolution momentum measurement for charged particles of momentum ranging from $\sim$ 500 MeV/c up to the muon beam energy of $\sim$ 500 GeV/c. More importantly, the two magnets, with their fields lined up in opposite directions, provide a favorable geometrical condition which simplified triggering on a scattered muon. For this study, which relied on detecting muons which scattered through angles as small as 0.5 $mrad$, knowledge of the position of the unscattered muon was crucial to the operation of the trigger. The configuration of each magnet was such that the field integrals were inversely proportional to the distance of the magnet from the first muon detection plane behind the steel muon absorber. The integral $\int B \cdot dl$ for these magnets was 4.3 Tm (Tesla-meters) for the CVM and -6.7 Tm for the CCM. This configuration provided a focussing condition where the position of the scattered muon in the first muon plane depended only on the scattered angle and was approximately independent of the energy of the scattered muon. This condition is shown in Figure 2.7.

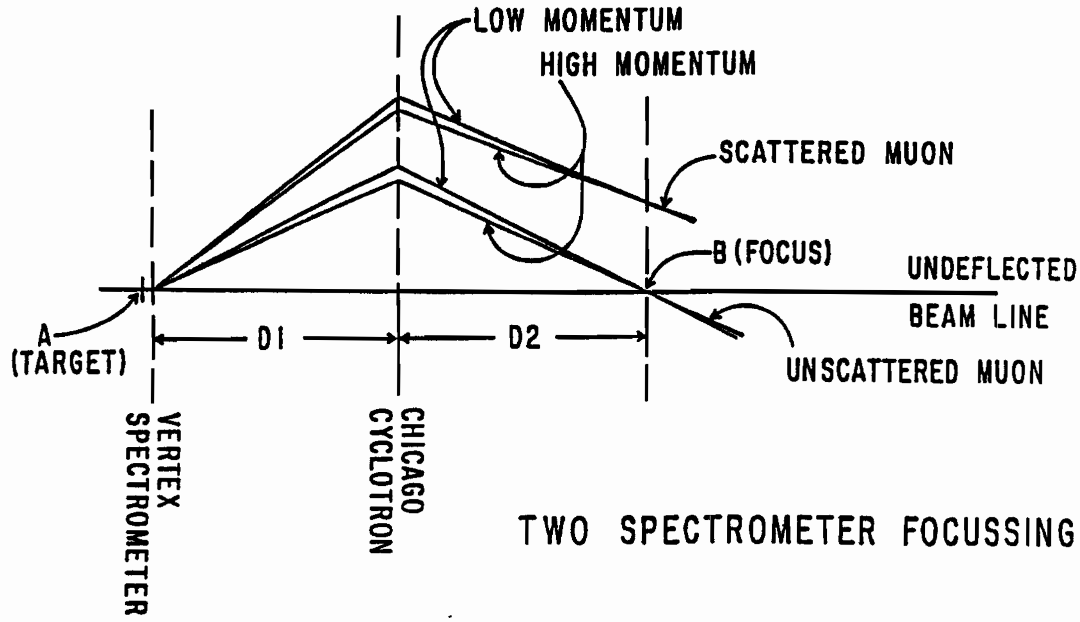

Figure 2.7: Double dipole focussing condition defined by the opposite field magnets CVM and CCM.

Unscattered muons were detected in the same position in the muon detectors as they would have been in the absence of magnetic fields. However, since the targets were placed inside of the first magnet, because of their length (1 m compared to the CVM field region of 2.5 m), the focussing condition was not completely independent of energy. This was the cause of a major source of background in the triggered events (see Section 5.6).

2.6.2 Scattered Muon Tracking Chambers

For inclusive cross section measurements, only the muon need be reconstructed; the properties of the beam and scattered muon were sufficient to measure the deep inelastic cross section. In this section, the tracking chambers used to reconstruct the scattered muon will be described.

Table II lists the relevant chambers and their respective nomenclature with which they will be referred.

TABLE II: E665 SCATTERED MUON TRACKING DETECTORS

Wire Chambers					
Name	Type	Aperture Z × Y (m)	Number/View of Planes	Wire Spacing	Gas
PCV	MWPC	1.0 × 2.8	Y,U,U′,V,V′,Y	2 mm	Ar-Isobutane
PC	MWPC	2.0 × 2.0	3 × (Y,Z,V,U)	3 mm	Ar-Isobutane
PCF	MWPC	1.0 × 2.0	5 × (U,V,Z)	2 mm	Ar-CO_2
DC1-4	Drift	2.0 × 4.0	4Z,2U,2V	1 cm	Ar-Ethane
DC5-8	Drift	2.0 × 6.0	4Z,2U,2V	1 cm	Ar-Ethane
PSA	MWPC	0.13 × 0.13	Z,Y,Z′,Y′,U,V,U′,V′	1 mm	Ar-Ethane
PTM	Prop Tube	3.6 × 7.2	4 × (Y,Z)	1.27 cm	Ar-Ethane
Scintillation Counters					
Name	Material	Thickness (cm)	Aperture Z × Y (m)	Number of Planes	Elements per Plane
SMS	NE110	1.3	0.2 × 0.2	4 × (Y,Z)	16Y,16Z

As can be seen from Table II, the chambers consist mainly of Multi-wire Proportional Chambers (MWPC's), with drift chambers for wide angle scattered muons and small hodoscopes for muon identification and matching behind the steel absorber (see Figure 2.6). The chambers will be divided into 4 groups for description;

1. PCV and PC MWPC's upstream of the CCM,

2. PCF MWPC's inside the CCM,

3. DC's and PSA downstream of the CCM and upstream of the steel absorber,

4. SMS hodoscopes and PTM proportional tubes downstream of the steel absorber.

Figure 2.8 shows an event display of a typical SAT event with the scattered muon track characterized by its projection downstream of the steel absorber.

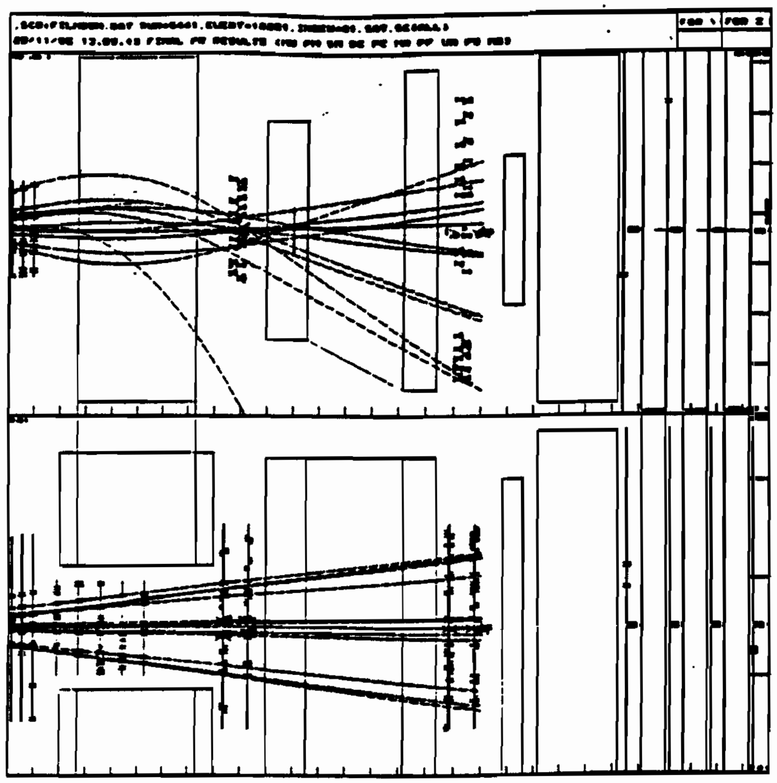

Figure 2.8: E665 event display of a typical SAT event showing the scattered muon projection linked with a Forward Spectrometer track and hadrons tracked through the CCM magnet.

PCV and PC Multi-wire Proportional Chambers

The two sets of MWPC's, PCV and PC, form the upstream (of the CCM) lever arm of the scattered muon track. For the scattered muon, a straight line segment was formed from wire hits in these two sets of chambers in the field-free region between the two magnets.

The PCV chamber group, built from a design used in a previous experiment [38], was located immediately downstream of the CVM and was necessary to provide good vertex and momentum resolution of the scattered muon in the target. The 6 wire planes were oriented as follows : Y - vertical wires; U - wires at $+45°$ from vertical; U′ - wires at $+18.5°$ from vertical; V - wires at $-18.5°$ from vertical; V′ - wires at $-45°$ from vertical; and Y - vertical wires. The wire spacing was 2 mm with an 8 mm gap from anode wire to cathode plane. The cathode planes were graphite and mylar coated Rohacell to minimize the amount of material in the detector. The cathodes were normally operated at $\sim 4.3\ kV$. The PCV planes used a gas mixture of 71.8% argon, 28% isobutane, and 0.14% freon which was bubbled through isopropyl alcohol, sometimes referred to as "magic gas".

The efficiencies of the PCV planes were measured to be $\sim 90\%$ for 5 of the 6 wire planes. The 6^{th} plane was consistently lower in efficiency ($\sim 75\%$).

The PC chamber group was used previously [31] and was brought intact to the E665 Experiment. Each of the 3 chamber groups consisted of 4 wire planes oriented in the following manner: Z - horizontal wires; Y - verical wires; U - wires at $+28°$ from vertical; and V - wires at $-28°$ from vertical. The wire spacing was 3 mm with an anode wire - cathode plane separation of 6 mm. The cathode planes were graphite-coated plastic with one cathode plane serving two anode wire planes and were normally operated at 2.9 kV. The gas used was the same mixture as in the PCV chambers.

As mentioned previously, the PCV chambers were crucial for good vertex resolution of the scattered muon in the target, but were not necessary for the successful reconstruction of these tracks. The PC chambers, however, were the starting point for scattered muon as well as hadron reconstruction in the forward spectrometer. While there were several algorithms used in the pattern recognition program to reconstruct scattered muons, the presence of at least some of the PC planes on a track was necessary for all of the methods (see Section 4.3).

The efficiencies of the PC's were measured and found to be strongly position and time dependent (see Section 5.3). During its best operating period, the PC chambers averaged $\sim 90\%$ efficient with efficiency variations between individual planes from $\sim 65\%$ to $\sim 95\%$.

PCF Multi-wire Proportional Chambers

The 5 groups of 3-view PCF MWPC's [15] were designed to operate in a high magnetic field environment, and were used to provide information on the track curvature in the CCM. For Small Angle Trigger events, these planes represented the last tracking information on the majority of the scattered muons until the track reached the PSA planes ($\sim 13\ m$ from the center of the CCM). Because of this situation, all of the scattered muons which traversed the PSA chambers were required to have at least 8 PCF planes with hits on the track. Because they were crucial to tracking scattered muons as well as hadrons in the interactions, several different pattern recognition algorithms were used to maximize the track-finding abilities of these chambers. Straight line projections, projections with knowledge of the magnetic field, and spacepoints were all utilized in the PCF MWPC pattern recognition algorithms (see Section 4.3).

The 5 chamber groups each consisted of the following orientations of wire planes : Z - horizontal wires; U - wires at $+15°$ from vertical; and V - wires at $-15°$ from vertical. The wire spacing in each anode plane was 2 mm with an anode - cathode gap of 6.4 mm. The cathode planes were made of aluminized Kapton with styrofoam backing to have as little material as possible in the active area. High voltage on the cathode planes was typically set at 3.8 kV. Support wires were included in the planes which deadened those regions, however, they were offset in different planes to avoid a common dead region. The gas mixture used was 80% argon, 19.7% CO_2, and 0.3% freon.

The PCF plane efficiencies were also found to be position dependent due to the presence of support wires which, fortunately, were not in the way of the scattered muons used in this analysis. The average efficiency of the 15 PCF wire planes was $\sim 95\%$.

DC Drift Chambers and PSA Multi-wire Proportional Chambers

To form the downstream (of the CCM) lever arm of the scattered muon track, two large groups of drift chambers, the DC's [46], and a set of 8 MWPC's, the PSA's [2], were used. The DC's provided a straight line segment which was linked to the segment from the PC planes in one algorithm, and were also used as targets for projections of lines found in the PCF planes in order to pick up hits on a track.

The DC's were arranged in two groups of 4 chamber packages. Each group of 4 packages contained drift wires in the following configuration : 4 Z planes - horizontal wires; two U planes - wires at $+5.758°$ from vertical; and two V planes - wires at $-5.758°$ from vertical. The drift cells were 50.8 mm wide in the drift direction and 9.6 mm wide along the beam direction. The drift field achieved was 492 V/cm and with the gas mixture of 50% argon - 50% ethane bubbled through ethanol at $0° C$, resulted in a drift velocity of $\sim 4\ cm/\mu sec$.

Away from the beam region, the average measured efficiency for the DC's was found to be $\sim 95\%$ using halo muons.

arranged vertically; Z - 16 hodoscope elements arranged horizontally. The individual elements of each plane were 13.2 mm wide for the central 14 elements with the two end elements cut at a 19.6 mm width. The scintillator was cut with beveled edges to provide an overlap of 0.3 mm between individual hodoscope elements.

The efficiency of the SMS hodoscopes was measured using beam triggers and found to be $> 98\%$.

2.7 Wire Chamber Alignment

The individual detectors used to measure the trajectory of the incident and scattered muons were nominally positioned at the beginning of the run with their centers aligned with the position of the unscattered beam. This position was determined by calculation and the detector positions verified by surveying. During the run, various configurations of magnets on and off were used in conjunction with beam and halo triggers to determine the relative alignment between chambers. Also, in the normal data-taking mode, the same beam and halo triggers could be used with all the magnets on to determine local alignment parameters and as a check on the change in alignment as a function of time. Table III lists the types of dedicated alignment runs used at various times during the data-taking period.

TABLE III: ALIGNMENT RUN CONFIGURATIONS

Beam Tagging Magnet	CVM	CCM	Trigger	Alignment Purpose
off	on	on	beam halo	relative alignment of
off	on	off	beam	beam spectrometer and
off	off	off	beam halo	forward spectrometer
off	off	off	beam	wire chambers
on	off	off	beam halo	relative alignment of
on	off	off	beam	forward spectrometer

2.8 Electromagnetic Calorimeter

The final piece of the E665 apparatus to be described is the Electromagnetic Calorimeter [3]. While this piece of the apparatus did not contribute directly to the scattered muon reconstruction, it was crucial in the selection of deep inelastic events in the low x_{Bj} region due to the large amount of electromagnetic background present especially in the xenon target interactions. A typical muon-xenon bremsstrahlung event is shown in Figure 2.10 with the Electromagnetic Calorimeter response shown in quadrant 4.

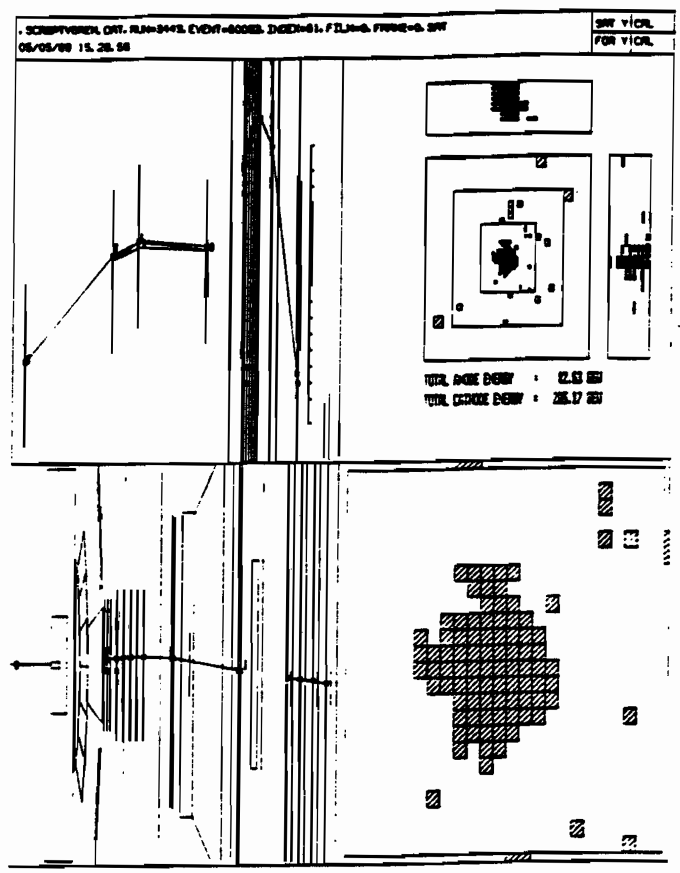

Figure 2.10: Muon-xenon bremsstrahlung production event with Electromagnetic Calorimeter response.

Note the large cluster of energy deposited in the central region of the calorimeter, and that although offset slightly in the Y view, the cluster is centered around $Z = 0$. This shows the typical small angle deflection of the muon when generating a bremstrahlung photon, but with a large energy loss in the presence of the CVM magnetic field which destroys the focussing

3. SMALL ANGLE TRIGGER

The purpose of the Small Angle Trigger (SAT) was to accept and record DIS events at low x_{Bj} and low Q^2, i.e., $x_{Bj} \leq 0.01$ and Q^2 less than 3.0 $(GeV/c)^2$. This was accomplished by allowing the scattered angle of the incident muon to be small since the Q^2 of the interaction and the scattering angle are related by

$$Q^2 \cong EE'\theta^2$$

for energies much greater than the mass of interacting particles and at small angles. Since small angle scatters result in the scattered muon remaining within the phase space of the beam, each beam muon trajectory must be evaluated individually by the trigger processor to determine if it scattered or not. In this section, the SAT and RSAT (beam trigger) components and configurations will be described.

3.1 Small Angle Trigger Components

An SAT event consisted of a selected incoming beam as measured in the Beam Spectrometer hodoscopes (SBT's), and the absence of a signal in the projected beam region of the Small Muon Scintillator hodoscopes (SMS's). The projected beam region was not fixed, but was determined for each beam muon by a pre-determined combination of SBT hodoscope elements. Also included was the 53 MHz RF time structure provided by the Tevatron which defined 18.9 $nsec$ width time "buckets" containing muons, and a system busy (SB) gate of $2-3$ $msec$

number of triggers to be $\sim 80/sec$, representing a 20% deadtime. In addition, a positive muon signal was defined behind the absorber, but was not used as part of the SAT trigger for this analysis.

3.1.1 Small Angle Trigger Beam Definition

Beam Trigger Matrix Elements

The two beam components of the trigger, BY (horizontal or bend plane) and BZ (vertical or non-bend plane), were made from hodoscope element combinations of SBT2Y, SBT3Y, SBT4Y, and SBT1Z, SBT3Z, SBT4Z, respectively. The appropriate beam combinations were generated before the data run started using a Gaussian beam distribution of energy 500 ± 75 GeV as input to the E665 Monte Carlo program. Relative hodoscope plane alignment was taken from the survey information contained in the E665 Level 1 constants. Only the central 5 elements (hodoscope counters $5 \rightarrow 9$) contributed to the beam definition from SBT3Y, SBT4Y, SBT3Z, and SBT4Z. This was necessary to achieve uniform spatial resolution in the downstream SMS hodoscopes from the projection of the SBT beam combinations. All of the counters ($1 \rightarrow 13$) were allowed to contribute from SBT2Y since it was not used in the beam projection, and from SBT1Z, since all of the counters were of equal width. The resulting beam hodoscope element combinations were stored as a 3-dimensional matrix in each view (Y,Z), where each dimension corresponded to one of the 3 contributing SBT planes. These matrices, containing all of the allowed beam hodoscope element combinations for BY and BZ, were down-loaded into RAM chips in the SAT Beam Trigger Matrix modules.

Clean Beam Selection

In an attempt to isolate beam muons from a single RF time bucket, the beam selection by the Trigger Matrix modules was "cleaned" by vetoing signals in adjacent RF time buckets. This was necessary because the signals from the SBT hodoscopes were ~ 3 buckets wide. Also, a veto was formed by signals from counters outside the central region of the beam projection planes whenever they ocurred with an acceptable BY or BZ contribution.

The adjacent RF bucket veto was formed by creating an ORed signal of the 7 SBT planes, sending it 1 RF bucket early to the trigger-forming module to make a late bucket veto, and delaying it by 1 RF bucket to form an early bucket veto.

The outside counter veto was formed in the ECLline cable by removing the central 5 counter signals and ORing the remaining signals, forming a veto in the trigger RF bucket if any outside counters were on. Three such "cable vetos" were used on signals from SBT3Y, SBT4Y, and SBT4Z.

The combination of these two vetos, which helped to eliminate multiple beams from the SAT and RSAT triggers; along with the BY and BZ trigger matrix beam definitions, formed the SATBEAM signal :

$$BY \bullet BZ \bullet \overline{CLEAN}$$

The SATBEAM signal was latched and scaled, and when counted in coincidence with the live time (or system busy veto) of the experiment and the RF strobe, formed the beam normalization for SAT triggered events. The subset of muons selected by the SAT beam definition represented $\sim$ 12% of the total beams used by the experiment.

3.1.2 Veto from Beam Projections

Veto Trigger Matrix Elements

The two veto components of the trigger, VY and VZ, were made from hodoscope element combinations of SBT3Y, SBT4Y, SMS1Y OR SMS2Y, and SBT1Z, SBT4Z, SMS1Z OR SMS2Z, respectively. The hodoscope elements contained in the 2 SBT planes of each veto matrix were by definition part of a valid 3-plane BY or BZ trigger matrix hodoscope element combination. The SMS counter for the 2-plane beam combination was found by projecting the two SBT contributions to the X-position of SMS plane 1. To form the resulting veto matrix, one additional SMS hodoscope element was added to each side of the projected counter, making the veto width equal to 3 SMS hodoscope counters ($\sim$ $3cm$ wide). The beam-veto hodoscope element combinations were then stored as a 3-dimensional matrix in each view (Y,Z) and down-loaded into RAM chips in the SAT Veto Trigger Matrix modules.

Veto Matrix Modifications

After the 1987-88 data run started, and as the SAT trigger was implemented, the combination of real muon beams and actual relative hodoscope plane alignment required modifications to be made to the veto trigger matrices. Several "holes" were discovered by the real beam which were subsequently corrected by the addition of new beam-veto hodoscope element combinations; and an additional SMS counter was added to the edge of the overall veto matrices. The resultant veto width in the SMS counters for the VY trigger matrix was 5 hodoscope counters wide for events with a single hit in each of the SBT projection planes. One 6-counter effective width for a single hit combination was caused by the addition of counters at the edge of the matrix. The presence of multiple SBT hodoscope element hits in the beam projection planes ($\sim 50\%$ of the time since the overlap was half the counter width for the central 5 elements) caused the actual veto region to be widened slightly. For both the deuterium and xenon data used in this analysis, the average veto width for all SAT triggers was 5.5 SMS counters wide ($\sim 5.5cm$).

3.1.3 Muon Signals

The two muon components, MY and MZ, were formed from the OR of like counters from SMS1Y, SMS2Y, and SMS1Z, SMS2Z, respectively. The resulting two 2-dimensional matrices (diagonal) were down-loaded into RAM chips in the Muon Trigger Matrix modules. The muon requirement was not included in the SAT Trigger for the data used in this analysis, but the signals from the Muon Trigger Matrix modules were latched and recorded in the event scalers. Since the muon signal was not required in the trigger, SAT events could be used to monitor the efficiency of other E665 triggers and the efficiency of the muon detectors.

3.2 Trigger Configurations

The interaction trigger, SAT, and the beam trigger used for normalization, RSAT, were formed by strobing the appropriate raw trigger signal with the RF timing signal and the system busy veto. In this section, the various trigger configurations used in the 1987-88 data run are described.

3.2.1 RSAT Beam Monitor Trigger

The RSAT Trigger was the prescaled beam trigger for the SAT interaction trigger. The following configuration was used to form RSAT :

$$BY \bullet BZ \bullet \overline{CLEAN} \bullet PSRF \bullet \overline{SB}$$

The elements BY, BZ, and $CLEAN$ were described previously, forming the SATBEAM definition. Although $CLEAN$ evolved during the run, its final and most used configuration consisted of the following components :

- For the ± 1 RF bucket veto, a 7 out of 7 SBT plane coincidence.
- For the "cable veto", outside counters $1 \rightarrow 4$ and $10 \rightarrow 13$ were used from planes SBT3Y and SBT4Y, and outside counters $1 \rightarrow 3$ and $11 \rightarrow 13$ were used from SBT4Z.

$PSRF$ was the RF timing signal randomized and divided by a pre-determined factor in order to select a random, well-known percentage of the available beam candidates. SB was the system busy gate described earlier in this chapter.

The resulting RSAT trigger was a beam which satisfied the Beam Trigger Matrix module combinations and was not accompanied by any other beams in adjacent RF buckets or in the same RF bucket outside the defined SAT beam region. The total number of RSAT triggers was determined by the pre-scale factor which related the number of RSAT triggers to the total number of SATBEAM counts.

3.2.2 Small Angle Physics Trigger

The SAT Trigger was the interaction trigger defined for events in which the incoming beam muon scattered at a small angle which remained within the total beam phase space but which was outside the beam region defined by the SAT Veto Trigger Matrix. The following configuration was used to form SAT :

$$BY \bullet BZ \bullet \overline{CLEAN} \bullet \overline{(VY, VZ)} \bullet (MY, MZ) \bullet RF \bullet \overline{SB}$$

For most of the 1987-88 run, the veto signal (VY, VZ) was VY only, however, some data (early D_2 and 100 GeV/c beam momentum) were taken with the veto as $(VY + VZ)$. Although indicated here as part of the SAT trigger, the muon signal (MY, MZ) was not required for any of the data taken.

Therefore, the SAT Physics Trigger consisted of a "clean" beam signal and the absence of a veto in the beam projection during the live time of the experiment.

3.3 Small Angle Trigger Rates

The following table shows trigger rates pertaining to the SAT and RSAT triggers for the xenon and deuterium targets and trigger configurations used during the 1987-88 run. The * items represent data not used in this analysis, but are presented here for completeness. The first entry, D_2 (early), represents the commissioning of the experiment and initial data-taking which was done with the deuterium target in place. During this time, the beam and veto definitions of the SAT trigger evolved towards their final configurations.

TABLE IV: TRIGGER RATES FOR THE 1987-88 RUN

Target	Beam Energy	RSAT/SATBEAM	SAT/SATBEAM
D_2 (early)*	500 GeV	1.80×10^{-5}	1.05×10^{-4}
D_2 (full)	500 GeV	2.57×10^{-5}	1.75×10^{-4}
Xe (full)	500 GeV	2.47×10^{-5}	1.79×10^{-4}
Xe ($\frac{1}{2}$ full)	500 GeV	2.37×10^{-5}	1.50×10^{-4}
Empty (liquid)	500 GeV	1.90×10^{-5}	1.31×10^{-4}
Empty (gas)	500 GeV	2.24×10^{-5}	1.48×10^{-4}
D_2 (full)*	100 GeV	1.84×10^{-5}	5.91×10^{-4}
Xe (full)*	100 GeV	2.14×10^{-5}	4.05×10^{-4}
Empty (liquid)*	100 GeV	1.93×10^{-5}	3.73×10^{-4}
Empty (gas)*	100 GeV	2.46×10^{-5}	3.50×10^{-4}

4. SMALL ANGLE TRIGGER EVENT RECONSTRUCTION

The E665 Spectrometer was designed to study nuclear effects in the initial muon - nucleus interaction and in the formation of hadrons as a result of this interaction. The spectrometer is a powerful tool for the identification and reconstruction of the final-state hadrons produced in DIS interactions as well as the initial beam - scattered muon vertex. All of the information necessary for the study of the inclusive muon - nucleus interaction is contained in the beam muon and scattered muon kinematics. For this analysis, the focus will be on the reconstruction of the muon - muon vertex, and only those parts of the apparatus used in this reconstruction will be described.

4.1 Beam

In order to determine the momentum transferred from the incident muon to the target in a deep inelastic event, the properties of the beam muon must be known accurately since errors in the beam energy measurement contribute directly to the event kinematics through the energy transfer variable ν. The E665 Beam Spectrometer was designed to measure the incident muon's momentum to within 0.5% at 500 GeV/c, and the position of the beam muon to within 300 μm in the Y and Z views. The following section describes the pattern recognition and track fitting algorithms necessary to provide this precision in measurement.

4.1.1 Beam Pattern Recognition

As described previously, the Beam Spectrometer included 4 stations of 1 *mm* pitch MWPC's. The duplicity and redundancy in the views of these 6-plane stations were ideally suited to the determination of a spacepoint which contained the spatial information (Y, Z) of the incident muon at each station. The pattern recognition of the beam track began with an algorithm which formed spacepoints from the allowed 3-view combinations of planes in each station. The following is a brief description of the spacepoint-finding algorithm :

- Initialize by determining the allowed 3-view wire plane combinations suitable for the detector geometry.
- Form a sum of the coordinates of all hits in the allowed 3-view combinations which represents the spatial extent of the "point" formed by the 3 wire coordinates.
- Combine 3-view combinations with other combinations when two out of the 3 wire coordinates are shared.
- In this way, build up 3-view combinations into a maximum of 6-plane spacepoints by combining combinations.

Since the beam muon's trajectory was perpendicular to the wire planes to within 1 *mrad*, and the extent of the 6-plane chamber package was just 12.5 *cm* in the X direction, only the (Y, Z) position of the incoming muon could be obtained by the spacepoint algorithm at each station. Figure 4.1 shows the distribution of the 3-plane sums for a typical single beam event.

The spacepoint algorithm was developed with the PBT MWPC's in mind, but it was sufficiently generic such that with only a few modifications, the same algorithm was used everywhere spacepoints were called for. This also included retention of multi-track separation capability which facilitated its use elsewhere. The MWPC's which used this algorithm and contributed to the reconstruction of the muon track were the PBT, PSA, PCF, and PCV chambers.

The spacepoints in the 4 beam spectrometer stations were then linked in the Z view (non-bend-plane) by fitting straight lines to all of the candidate spacepoint combinations. Since

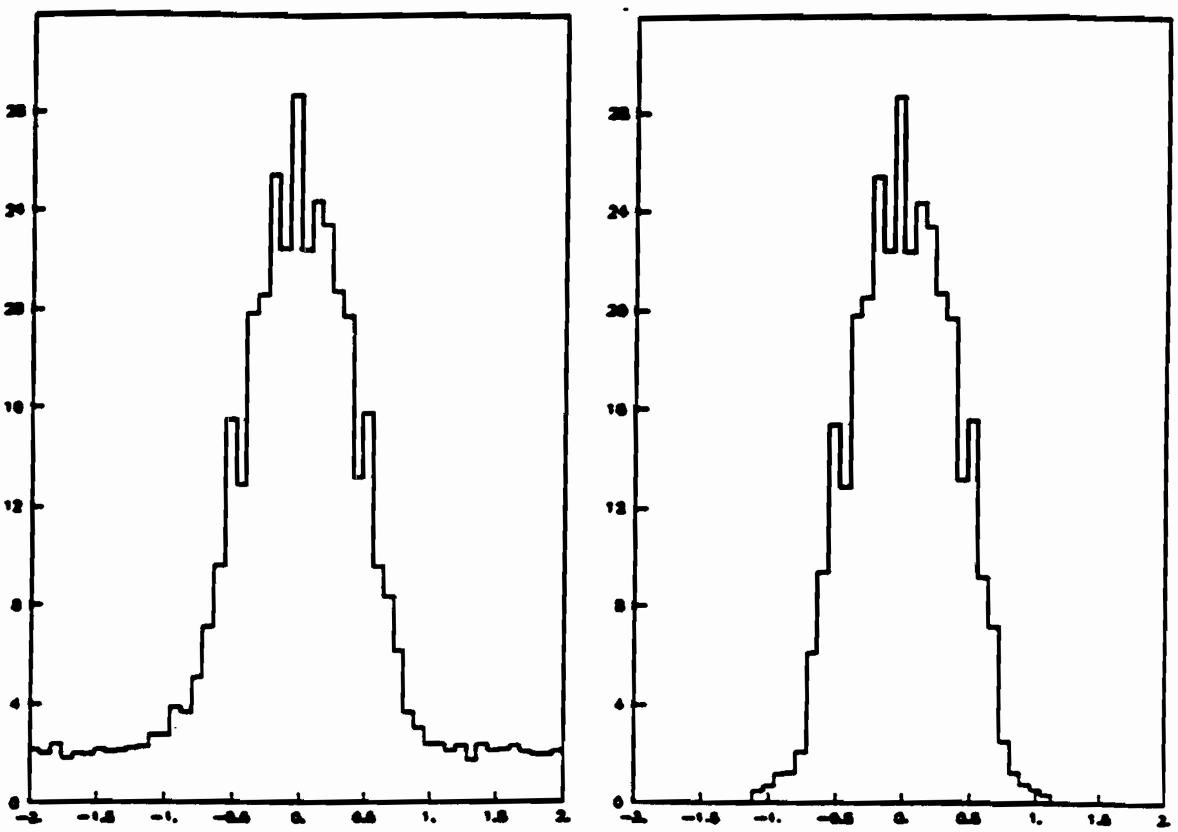

Figure 4.1: 3-Plane sums from the beam pattern recognition spacepoint algorithm.

information from both transverse coordinates (Y, Z) were contained in the spacepoints linked by the straight line fit, the resulting space-line was, in principle, a fully reconstructed track. However, since multiple beam reconstruction was important in order to determine the timing of SAT events (see Section 4.4), these space-line candidates were then checked by fitting straight-line segments before and after the beam spectrometer dipole magnet in the Y view, requiring that the two segments meet in the middle of the magnet - a necessary condition for constant field dipole magnets. This check enabled lines which shared coordinates and/or slopes in the Z view to be separated by the Y view bend. A successful beam muon track candidate passed both line requirements.

The wire coordinates of successful track candidates were then stored by the computer in a machine-independent bank format named LLIN (the bank that was used to contain the results of all final pattern recognition results).

4.1.2 Beam Track Timing Information

After the formation of the individual beam track (or tracks) by the pattern recognition algorithm, information from the latched SBT hodoscopes was used to determine the timing properties of each reconstructed beam track. Since a sizeable fraction of the beam halo is close to the beam itself, and the live time of the PBT's ($\sim$ 150 *nsec*) spans many RF timing buckets, it was possible to reconstruct beam muons which were present in the chambers, but which did not contribute to the trigger. For SAT events, with specific beam hodoscope combinations and associated projected veto regions, it was especially important to determine that at least one of the reconstructed beam tracks could have caused the trigger.

A software processor (denoted SB) was written to provide a timing label for each beam track found by the PB pattern recognition processor. This processor linked latched hodoscope elements with corresponding beam track positions in each of the 4 beam stations. The presence of a hodoscope element which could be linked to a spacepoint in the MWPC package was used to determine that beam track's timing. The hodoscope live times and efficiencies were such that only a beam track with all 7 hodoscope planes having an element linked to that track were in-time with the trigger RF bucket. Out-of-time tracks were those that did not have the full complement of hodoscope elements associated with them, and a third category called unknown time was used to describe tracks where not enough information was present to determine the timing. Table V shows the number of SAT events according to their beam track timing properties for a representative sample as determined by this processor.

TABLE V: SAT BEAM TIMING PROPERTIES

SB Timing		In-time Beams per Event 0	1	2	3+	Total
Out-of-time Beams per Event	0	40	12518	440	14	13012
	1	617	1927	64	2	2610
	2	145	272	9	0	426
	3+	33	22	1	0	56
	Total	835	14739	514	16	16104

These values are typical of the beam muons used by the SAT for both the xenon and deuterium data. The results of the SB processor were stored in a permanent bank named LHOD which linked hodoscope elements to the wire coordinates contained in the LLIN banks.

4.1.3 Beam Track Fitting and Momentum Determination

All of the beam LLIN banks representing reconstructed lines in the beam spectrometer were used as input to the Track Fitting (TF) program. A fit was made to each LLIN bank which generated a new bank named LSTF containing the properties of the fit, including the track's momentum. Figure 4.2 shows typical results from the TF Program for SAT beams.

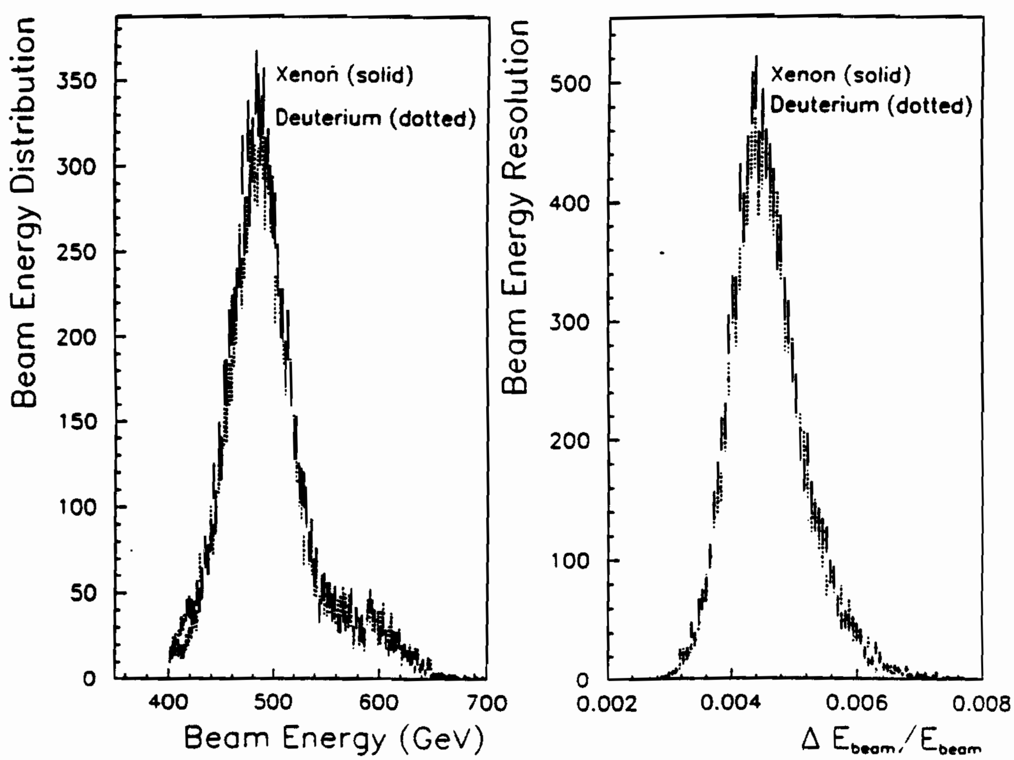

Figure 4.2: SAT beam properties from the results of the track fitting program.

The beam reconstruction and track fitting performed up to the level of its design. The parametrization of the measured momentum resolution was given by the track fitting results to be $\Delta p/p = p$ (in GeV/c) $\times 10^{-5}$. This contributed $\sim 25\%$ to the error in measurement of ν.

4.2 Scattered Muon

The identification of the scattered muon was accomplished by placing the muon detection hodoscopes (SMS and SPM) and the proportional tubes (PTM) behind a thick (3 m) steel absorber. The absorber effectively eliminated all charged tracks except those associated with muons from appearing in the detectors. The muon track candidates were reconstructed along with tracks associated with other charged particles in the MWPC's and drift chambers of the Forward Spectrometer. Linking projections in the muon detectors behind the absorber to a reconstructed track in the Forward Spectrometer completed the identification and reconstruction of a muon. The Vertex Processor determined whether any of the identified muon tracks were consistent with an interaction of the beam muon, thereby forming the scattered muon. The design of the forward spectrometer tracking chambers and muon detectors was chosen to give a precise measurement of the momentum of the scattered muon ($\Delta p/p \simeq 2.5\%$ at 500 GeV/c). The following sections describe in detail the identification and reconstruction of the scattered muon.

4.2.1 Muon Projections

The first part of the scattered muon pattern recognition was the determination that a particle had penetrated the 3 m steel absorber and was recorded in the SMS hodoscopes or the PTM proportional tubes (or an overlap of the two). Three software processors, PM, SM, and OV, were written to reconstruct projections in the Y and Z views in the PTM's, SMS's, and overlap region respectively. At least 3 of the 4 stations were required to have hits in a particular view to form a projection which was stored in the permanent bank named LPRO. The number of LPRO banks included projections found in the 3 processors in each view. The PTM chamber efficiencies were measured to be $> 95\%$ in each of the 8 planes and the SMS efficiency was measured to be $> 98\%$ in each of the 8 hodoscope planes. Normally, only one projection was found in each view, representing the path of one muon through the SMS or PTM detectors. Figure 4.3 shows the multiplicity of projections in the Y and Z views with the different regions indicating the relative number of projections of each type (SMS only, PTM only, or SMS-PTM overlap).

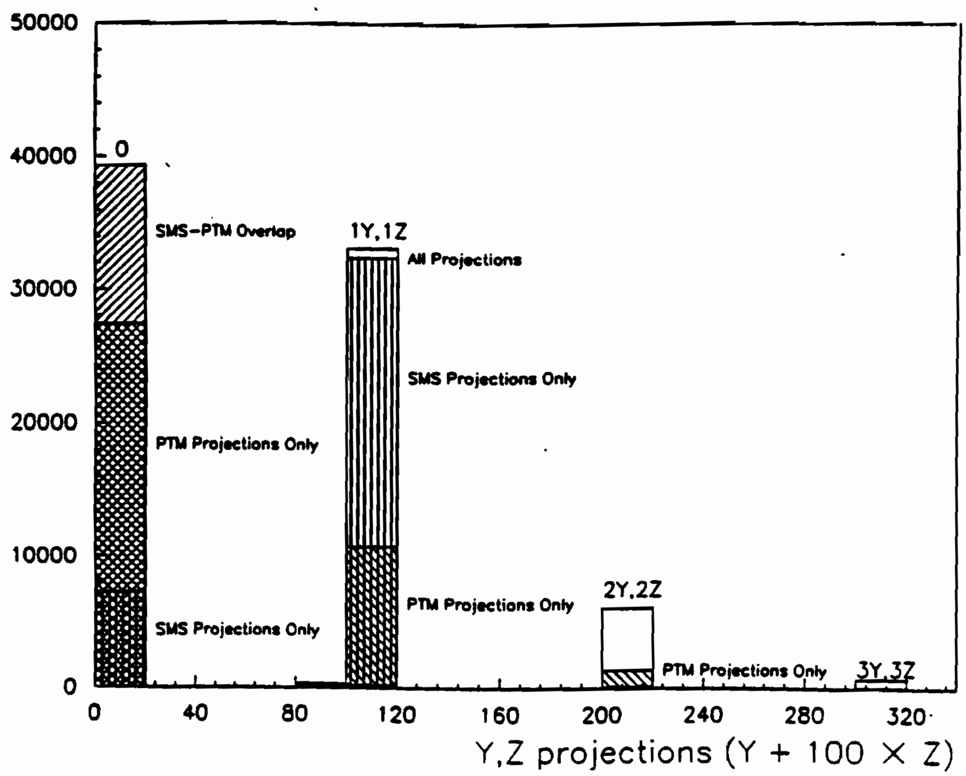

Figure 4.3: Multiplicity of projections in the muon detectors. The solid line is for SMS only, the dotted line is for PTM only, and the dot-dash line is for SMS-PTM overlap projections.

Notice that the overall percentage of projections is $\sim 75\%$ in the SMS with $\sim 25\%$ in the PTM for these SAT events with one muon projection in each view. The fraction of SMS-PTM overlap events is less than 1%. The overall loss in events due to inefficiencies in the post-absorber hardware and software has been estimated to be $< 1\%$. The loss in events due to multi-muon signals in this region is also $< 1\%$.

The efficiency of muon projection reconstruction is estimated to be $\sim 99\%$, since both the PTM and SMS detectors individually had high efficiencies. The reconstruction efficiency of small angle scattered muon projections could be measured by using RSAT triggered events. Since RSAT events represented the beam part of the SAT trigger, there was no requirement in the SMS veto region. However, for these events, the signal in the SMS counters was latched, showing the veto region defined by the SAT trigger matrix projections. Knowing which SMS counter should have fired according to the beam projection stored in the trigger matrix, the

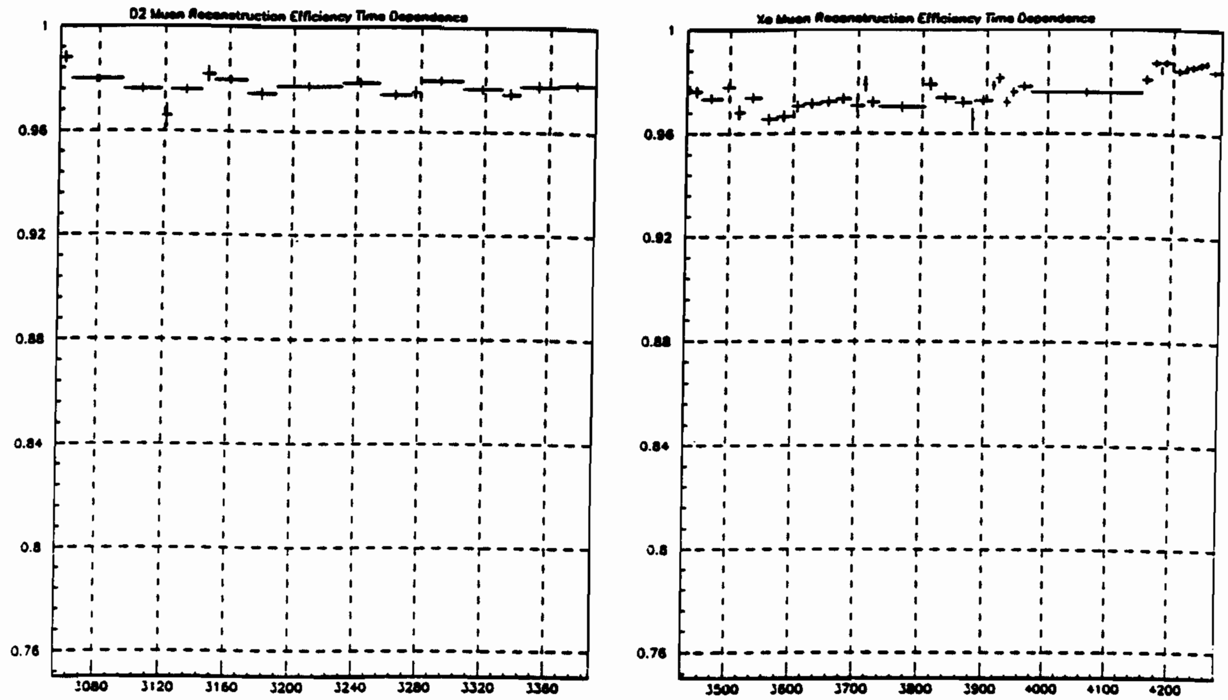

Figure 4.4: SMS muon projection reconstruction efficiency versus time.

efficiency of an individual SMS counter could be measured for all combinations of beam-veto projections. The measurement of muon projection reconstruction from this method yielded an overall SMS reconstruction efficiency consistent with the individual plane efficiency estimate of $> 98\%$. Figure 4.4 shows the SMS reconstruction efficiency measured by RSAT triggers as a function of time in both the deuterium and xenon running periods.

The measurement of projection reconstruction efficiency in the PTM and overlap region could not be done with data alone. The results from Monte Carlo simulation which included the measured plane efficiencies, however, yielded a projection reconstruction efficiency of $\sim 98\%$, very similar to the SMS measurement. Therefore, the overall muon projection reconstruction was estimated to be $> 98\%$ efficient.

4.2.2 Forward Spectrometer Pattern Recognition

The identification of the scattered muon track in the forward spectrometer began with pattern recognition of wire hits in the various chambers. The pattern recognition software incorporated two passes : 1) "Muon" phase which nominally reconstructed the track of the scattered muon, and 2) "Hadron" phase which completed the track finding by using all the hits not used in the first pass. While the two passes have names which suggest the type of particles found in each, they are the result more of definition than of content. The primary distinction between the two passes was the type of cuts used - the "Muon" phase generally had tighter spatial cuts and road widths than those corresponding to the "Hadron" phase. This presumably found "stiffer" tracks in the first pass and allowed less stiff tracks to be found in the second. While most of the muons in SAT events were found in the "Muon" phase, the number of hadrons found in the two passes was approximately the same. Even though some of the cut parameters and the input wire hits were different in the two passes of pattern recognition, the algorithms used (including the order of implementation) were identical. Therefore, only the "Muon" phase of the pattern recognition program will be referred to in the following description.

The forward spectrometer pattern recognition algorithm consisted of the following "local" pattern recognition processes arranged in the indicated order :

- formation of straight line segments in the DC's.
- formation of straight line segments in the PC MWPC's.
- attempt to match the line segments from the previous processors using wire hits in the PCF's through the CCM field.
- formation of spacepoints in the PSA MWPC's.
- formation of line segments consisting of PC line segments (not matched to DC line segments) and PCF wire hits using knowledge of CCM magnetic field.
- projection of PC-PCF line segments to the PSA including a bending approximation, matching the line segment with a PSA spacepoint.

- projection of PC-PCF line segments to the DC's including a bending approximation, matching the line segment with DC hits.
- formation of line segments from spacepoints made from unused hits in the PCF's.
- projection of PCF line segments to pick up wire hits in th PC, PSA, and DC chambers.
- formation of straight line segments in the PCV MWPC's.
- projection of line segments formed with a PC plane as its starting point back to the PCV, matching with a PCV spacepoint.
- storing of all found line segments in the bank, LLIN.

All "tracks" found by the pattern recognition which were considered scattered muon candidates included wire hits from the PC MWPC's in the LLIN bank.

For SAT events, most of the scattered muons were located in the central region of the forward spectrometer MWPC's and were seen downstream of the CCM in the PSA planes covering the hole in the DC's. Since the PSA's were located $\sim 13\ m$ from the last wire plane recording the muon's path (PCF station 5), the projection of the found line segment in the PC-PCF chamber groups to the PSA was crucial for finding and identifying the scattered muon. Figure 4.5 shows the transverse (Y, Z) distribution of scattered muons at the PSA X position.

As shown in the above pattern recognition description, several algorithms were developed to find line segments which included wire hits from the PC and PCF MWPC's. These algorithms employed many methods to associate hits including straight line projections, spacepoints, and projections which included knowledge of the magnetic field or geometrical fits to non-linear trajectories. In any case, the result after employing these algorithms was a line segment which ended typically at the chamber group designated as PCF5 - the last PCF group, which was located approximately in the center of the CCM magnetic field. For the case of small angle scattered muons, the next piece of tracking information was a spacepoint in the PSA group $\sim 13\ m$ from PCF5. The spacepoint in the PSA was found by the same algorithm as used in the PBT MWPC's, and the multiplicity of spacepoints in the PSA for SAT events is shown in Figure 4.6.

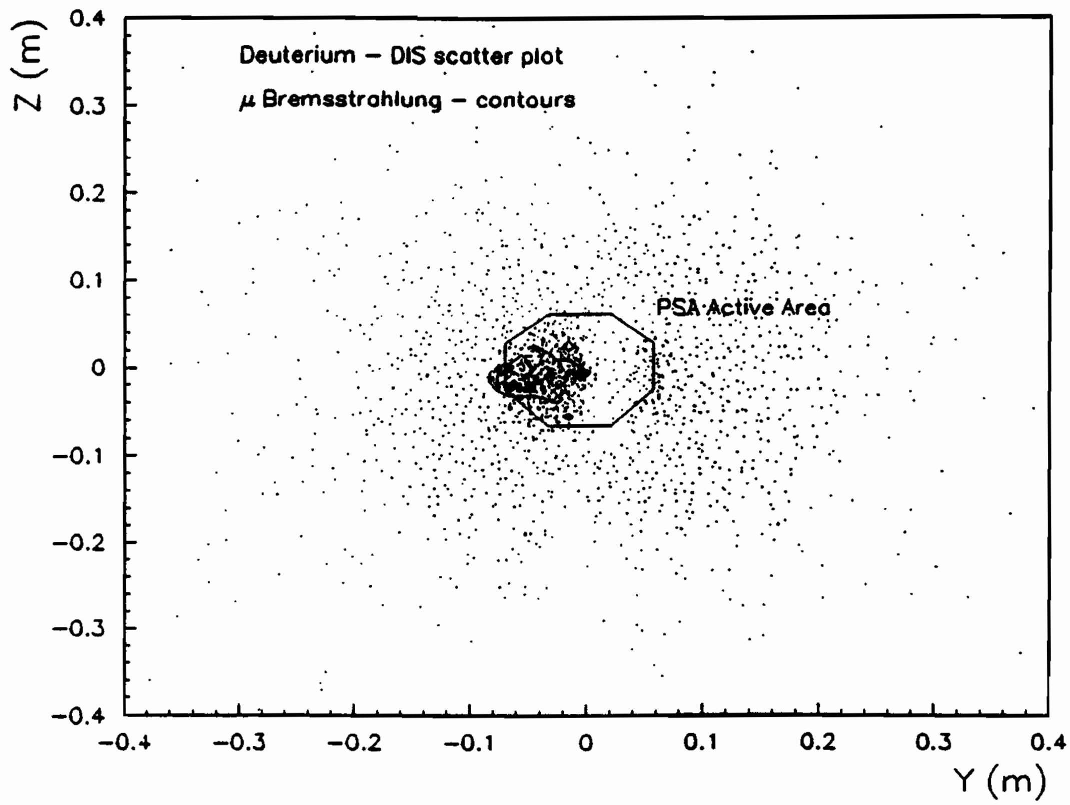

Figure 4.5: Transverse distribution of scatttered muons at the X position of the PSA MWPC's.

Note that the average multiplicity given by this figure also includes the scattered muon. The 8 planes of the PSA were separated in the X direction by only 8.3 *cm*, and since the slope of scattered muon trajectories was small (< 2 *mrad*), only the Y and Z coordinates of the track were included in the reconstructed spacepoint.

A processor was developed which projected the line segment found in the PC-PCF detectors through the remaining portion of the CCM magnetic field and then to the PSA, forming a window in (Y, Z) which was used as a mask for any PSA spacepoints. No knowledge of the actual field components was used in the fit, however, the extent of the field in the X direction (along the beam) was estimated to determine how much of the fit was non-linear. The shape of the fit through the remaining part of the CCM was parabolic, which is a good approximation of the actual path of high-energy scattered muons through the real magnetic field. The approximation of parabolic shape was not good for charged particles with momentum

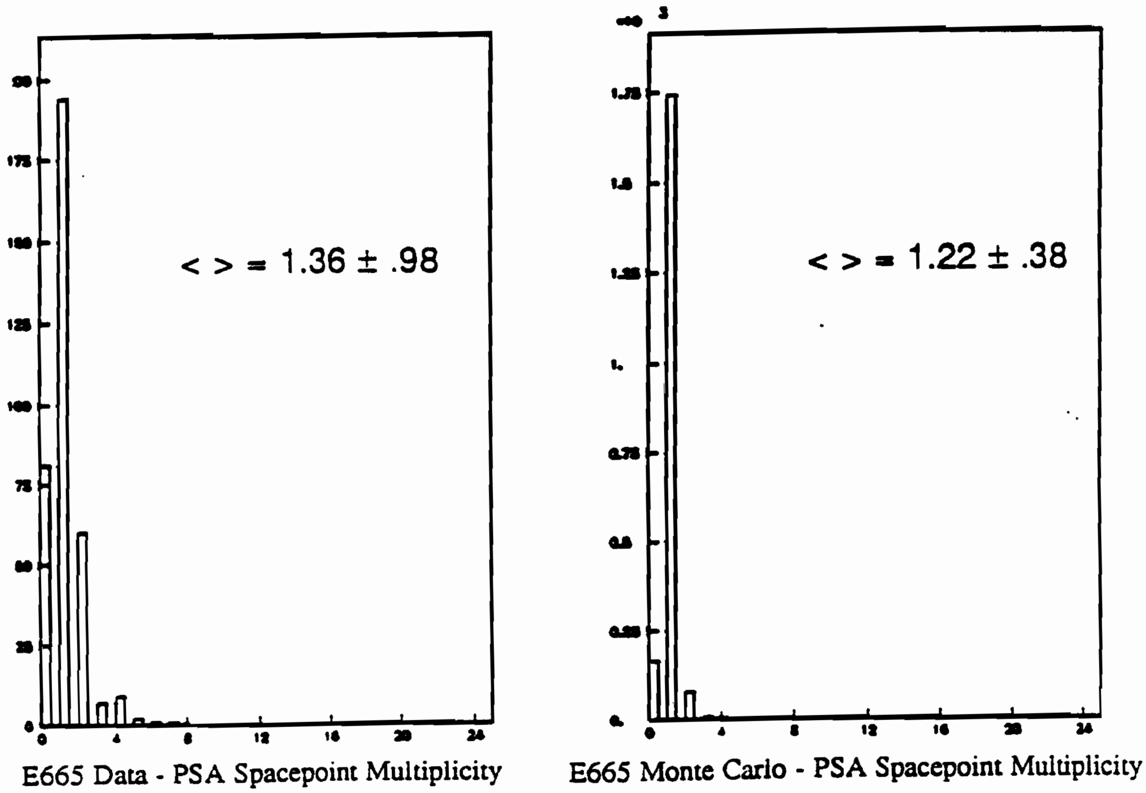

Figure 4.6: PSA spacepoint multiplicity for SAT events.

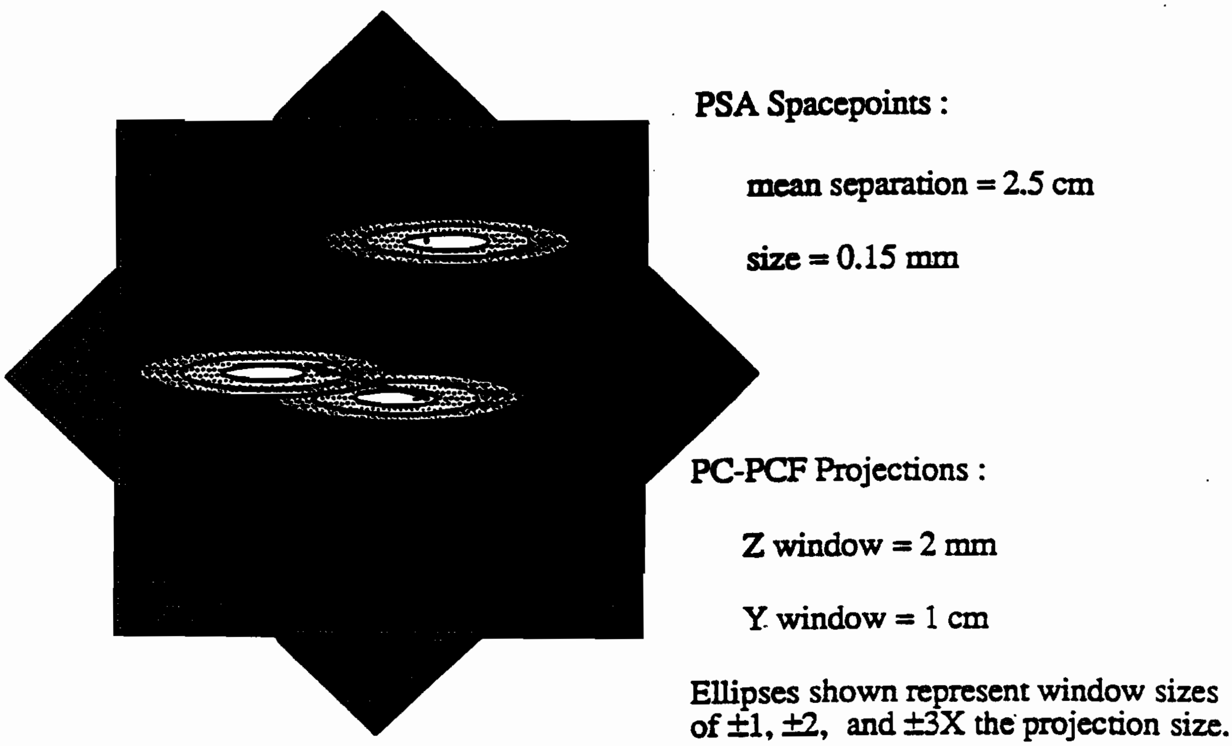

Figure 4.7: Results of the small angle scattered muon pattern recognition program.

less than 10 GeV/c or for particles with large slopes in the Z view. The fit was used since it not only projected the line segment found in the field region, but also yielded a χ^2 value indicating the quality of the fit and an error matrix which formed the basis of the PSA window. The results of the parabolic fit were reported just downstream of the CCM magnetic field region. The parameters of the fit, including the errors on the positions and slopes were then projected to the PSA, yielding a projected position in (Y, Z) and a σ_y and σ_z at that point. The window size at the PSA was then determined by including $\pm 3\sigma$ distances in each view resulting in a confidence level for including the true spacepoint of better than 99% (assuming Gaussian distributed errors). The results of this algorithm are shown in Figure 4.7.

The beam muon reconstruction efficiency in the Forward Spectrometer could be measured using RSAT events similar to the method used to estimate the muon projection efficiencies described earlier. This method yielded a reconstruction efficiency in the beam region of the

Forward Spectrometer of 94%, which agreed with the Monte Carlo estimate of 95% in the same region.

4.2.3 Track Fitting and Momentum Determination

The Track Fitting program used as input lines found by the pattern recognition and stored in the permanent bank - LLIN. Normally, wire hits from PCV $\rightarrow$ PSA were present in LLIN banks representing scattered muon candidates. The track fitting algorithm was a fit of these coordinates using the Quintic Spline method. The 5 parameters returned by the fitting technique for each track were the two transverse coordinates - Y, Z; the slope of the track Y', Z'; and the momentum 1/p; reported at a position along the X-axis near the target. The banks used to store the results of the track fitting were designated LSTF.

While in principle, all LLIN banks representing lines found by the pattern recognition were fit, some quality testing was done as part of the track fitting algorithm. Goodness of fit was determined by evaluating the χ^2 probability of the fitted lines.

4.2.4 Forward Spectrometer - Muon Projection Matching

The purpose of the muon match processor was to determine which of the muon candidates found by the forward spectrometer pattern recognition and track fitting algorithms matched the projections found behind the steel absorber in the PTM and SMS muon detectors. The reason that this processor was run after track fitting was that in order to include the possibility of multiple scattering in the steel absorber, the momentum of the candidate track must be known. In the muon match algorithm, multiple scattering in both the steel absorber and the lead of the calorimeter was allowed to occur. The multiple scattering contributed to the error in measurement of the slope (or angle of incidence) and the position of the candidate track. The following formulas show how this error contribution was determined :

$$\delta\theta_{\mathrm{rms}}{}^{\mathrm{plane}} = ((0.0141\ GeV/c)/P)(\sqrt{L/L_R})(1+\frac{1}{9}\log(L/L_R)) \tag{4.1}$$

$$\delta\mathrm{Position}_{\mathrm{rms}}{}^{\mathrm{plane}} = (\mathrm{L}/\sqrt{3})(\delta\theta_{\mathrm{rms}}{}^{\mathrm{plane}}) \tag{4.2}$$

where P is the momentum of the particle, L is the length of material, and L_R is the radiation length of the material. A match "χ^2" is formed according to the following formula :

$$\chi^2_i = (C_i(\mathrm{LSTF}) - C_i(\mathrm{LPRO}))/((\delta M_i)^2 + (\mathrm{LPRO\ error})_i{}^2) \qquad (4.3)$$

where the C_i refers to the two coordinates (Y, Z) and their respective slopes (Y', Z'), the δM_i refers to the multiple scattering contributions to the error for each item, and the (LPRO error)$_i$ to the appropriate error matrix element in the LPRO projection. Cuts were made on this χ^2 separately for each view in position and slope. If an LSTF and an LPRO(Y) and LPRO(Z) passed the cuts, then the LSTF was designated a muon, and an LMUN bank was filled with the appropriate LPRO information.

In addition to the above algorithm, allowance was made after performing the above test for large angle scattering of muons in the steel or lead planes of the calorimeter. An algorithm which tested for an intersection of a forward spectrometer LSTF fitted track and LPRO's was run if any projections were left after the first pass. If an intersection was established, then the LSTF bank was flagged as a muon and the appropriate LPRO's included in a LMUN bank.

The muon match processor was very efficient at linking LSTF banks with LPRO projections. Monte Carlo studies indicate that for the properly found LSTF fitted tracks and LPRO projections, the efficiency of the muon match was $> 99\%$. Also, the loss rate due to multiple muons appearing in the muon detectors was $\ll 1\%$.

4.3 Vertex Processor

The vertex finding and fitting program used in E665 was developed specifically to find vertices in magnetic field regions. The method of determining the vertex position was to find the point of closest approach for a set of tracks, and by fitting these, determine if they were consistent with a scattering interaction at that point. Full knowledge of the track parameters including momentum was needed since vertices occurred both inside and outside of magnetic field regions. For this analysis, only the vertex designated as "primary" was important, since this was the vertex that contained the beam and scattered muon. A special algorithm was used to find these types of vertices for which one track was already known, i.e., the beam track. A different algorithm was used to find, for instance, neutral particle decays for which none of the associated tracks were known. The following sections describe the vertex fitting algorithm for primary vertices and the method of calculation used to determine the event kinematics.

4.3.1 Beam - Scattered Muon Vertex Fitting

Vertex finding and fitting is considerably simplified if some knowledge of its location and/or content is known. Such was the case for the primary vertex in this experiment.

The vertex processor began by searching for a beam muon - scattered muon vertex. All combinations of a beam track and a muon track as determined by the muon match processor were fitted, keeping acceptable vertices based on the χ^2 of the fit. Additional tracks were tested by fitting each one separately with the muon - muon vertex, flagging tracks to be included based again on the χ^2 of the fit. After checking all possible Forward Spectrometer tracks, the vertex was once again fitted, this time including all of the tracks which were flagged in their separate fits. If the χ^2 value was acceptable, the vertex was reported along with all of the associated tracks. If the χ^2 value was too large, associated tracks were systematically dropped, starting with the one which had the largest χ^2 from the previous test. After a track was dropped, a new fit was performed, again evaluating the χ^2. The vertex fit parameters were stored in the bank LVTX, and the associated track parameters were stored in individual LTKV banks which were linked to the LVTX bank.

4.3.2 Event Kinematics Determination

Once the primary vertex was identified, the calculation of the event kinematics using the 4-momentum vectors of the beam and scattered muon was done. In addition, the errors on the kinematic variables were also calculated using the measurement errors on the 4-vector components. The results of these calculations were stored in a permanent bank designated LEVF.

4.4 Small Angle Trigger Event Selection

The selection of events used in the final analysis was accomplished in several production steps. After splitting events on the raw data tapes onto tapes containing only one trigger type, i.e. SAT, preliminary analysis showed that there were many "bad" events contained in the raw sample. Table VI shows the characterization of raw SAT events from the xenon and deuterium targets.

TABLE VI: SAT RAW EVENT CHARACTERIZATION

SAT Event Type	Xenon	Deuterium
"Bad" Triggers		
• SBT - PBT mismatch	19 %	19 %
• Others	4 %	6 %
Non-interacting Beams		
• No μ behind absorber	16 %	19 %
• μ scatter in absorber	34 %	37 %
Target Events		
• $\mu - e$ and $\mu - \gamma$	23 %	7 %
• Deep inelastic	4 %	10 %

The "bad" triggers were caused by several hardware problems which were fairly constant during the data taking period. The SBT - PBT mismatch events were those in which the beam muon traveled through a hodoscope element which was not used in the SAT trigger, but an acceptable beam trigger matrix combination was generated by the random firing of a "hot" hodoscope element in the same station. These events were found after pattern recognition of the beam muon was done and the correlation between the beam track and the latched hodoscopes was determined; in these cases, the latched hodoscope element did not match the position of the beam track in the PBT MWPC's. Other "bad" triggers were due mainly to timing problems caused primarily by the presence of an out-of-time beam or halo muon which confused the SAT beam definition.

As can be seen in the table, most of the un-desirable events were characterized as non-interacting beams. The first type in this category, no μ behind the absorber, was a part of the

SAT sample because no muon was required in the trigger. Some of these were leftover hadrons, i.e. π's, in the beam. The hadron contamination was measured and found to be $\sim 0.5\%$. The largest contribution to this category were muon scatters in the steel absorber. These scatters caused the muon to be seen in the SMS or PTM detectors outside of the SAT veto region.

The last category, target events, contained the DIS events used in the final analysis. In addition, there was a significant contribution from electromagnetic events, especially muon bremsstrahlung from the xenon target.

In summary, if only target events were kept, the reduction in the number of events to be analyzed was a factor of ~ 4 in the xenon sample and ~ 5 in the deuterium sample. The following section describes an intermediate production stage called the SAT Event Filter which was developed to obtain these reduction factors and reduce the number of tapes used in the full analysis program.

4.4.1 Small Angle Trigger Event Filter

To gain the factor of 4 or 5 in reduction of non-target events as described above, a preliminary production stage in the event analysis called the "Event Filter" was run which used as input the raw events stored on the SAT "split" tapes. For SAT triggered events, the biggest single reduction was non-interacting beams which scattered in the hadron absorber, thus escaping the projected veto region in the SMS hodoscopes as described above. The goal of the filter was to gain as large as possible reduction factor while keeping all events which originated in the nuclear target.

The SAT Event Filter included 6 tests for raw events. These tests were included in the following general categories :

1. Trigger testing and selection.
2. Non-interacting beam selection.
3. Electromagnetic background flagging.

The tests included in the first category, Trigger testing and selection, were applied to both the SAT and RSAT event samples. The results of the RSAT filtering were required to modify the beam counting by the event scalers (see Section 5.1). This was done to guarantee that both event samples contained the same beams for normalization.

Several tests were performed on an event to determine whether it was consistent with the timing and matrix selection requirements of the SAT. As mentioned previously, the timing of the SBT latches was such that in-time events were characterized by 7/7 SBT hodoscope planes contributing. Therefore, the first test required that the event contained hits in all 7 SBT hodoscope planes. The timing of the SAT events was such that this test rarely ($\ll 1\%$) caused an event to be cut from the final sample. The filter code, however, contained a minor problem which made this test ineffective for both SAT and RSAT production jobs. For the RSAT data, which contained a significant fraction of out-of-time events ($\sim 30\%$), the results of this test did not represent correctly the SBT latch conditions. However, the out-of-time events, which passed through the first test, were rejected by the in-time requirement for reconstructed beams (see below). The next test used the results of the beam pattern recognition, requiring that at least one track be reconstructed in the Beam Spectrometer. This requirement caused $\sim 7\%$ of events to be cut from SAT data and $\sim 2\%$ to be cut from the RSAT data, the difference due to the presence of more multiple beams in the SAT data sample which confused the trigger. Following this, the timing properties of the reconstructed beams were determined using the SB processor (see Section 4.1). For SAT and RSAT events, only one in-time beam must have been identified. Any number of out-of-time or unknown-time beams were allowed in an event. For SAT events, 9% of the remaining events at this level were cut by this test. For RSAT data, $\sim 37\%$ of the remaining events were cut due to the large fraction of out-of-time events recorded. This requirement was made so that the SAT trigger configuration for the in-time beam could be determined unambiguously which was the final test in the first category. The validity of the SBT hodoscope combinations linked to the in-time beam track was checked by comparing the appropriate elements to the SAT Beam Trigger Matrices (see Section 3.2). The event was cut if the hodoscope element combinations did not represent a valid SAT beam. This requirement caused $\sim 25\%$ of the remaining events to be cut from SAT data depending on the target and rejected $\sim 4\%$ of the remaining RSAT events.

The remaining tests in the last two categories were applied only to SAT events. A simplified version of the Forward Spectrometer muon phase pattern recognition was run to identify tracks in the beam region. If no tracks were reconstructed, the event was kept in the final sample and no further testing to cut the event was done. If more than one track was found, the event was also kept, since this could indicate hadron production in the event. If only one track was found, however, tests were performed comparing the Forward Spectrometer track to the in-time beam track. The beam track was projected through the CVM field to the position of the first chamber hits on the Forward Spectrometer track. This projection used the same algorithm for swimming tracks through the CVM field as the Vertex Processor, reporting the position (Y, Z), slope (Y', Z'), and momentum (1/p) of the beam track at the same location in X of the Forward Spectrometer track. The two tracks were compared, testing ΔY, ΔZ, $\Delta Y'$, $\Delta Z'$, Δp, ΔR, and $\Delta\theta$, where $\Delta R = \sqrt{(Y_{beam} - Y_{FS})^2 + (Z_{beam} - Z_{FS})^2}$, and $\Delta\theta = \sqrt{(Y'_{beam} - Y'_{FS})^2 + (Z'_{beam} - Z'_{FS})^2}$. Figure 4.8 shows the SAT and RSAT event samples with the non-interacting beam cuts superimposed.

Events inside the cut region were eliminated from the final SAT sample, resulting in a rejection of $\sim$ 60% of the remaining events in the xenon data and $\sim$ 50% of the deuterium data. Note that almost all of the RSAT events lie inside the cut region.

The final category was not a cut, but a flag used to classify the event according to its electromagnetic properties determined by the electromagnetic calorimeter. Since a large source of the background in the SAT sample was due to muon - nucleus bremsstrahlung events, a selection criteria based on the total energy deposited in the calorimeter was used to identify these. The events were not cut from the sample since they could, in principle, be corrected by using radiative correction calculations (see Section 5.6). Improvements in the calorimeter calibration and analysis code also enabled a more reliable cut to be used on the final SAT sample (see Section 5.6) when radiative corrections were not used.

Table VII shows the results of filtering on representative SAT and RSAT raw data samples. The numbers in parentheses indicate the fraction of input events passed by a particular filter type. The * indicates that the represented number of events was flagged only and no events were cut from the sample as described above. The last two filter tests were not performed on the RSAT data sample as indicated. Note that the RSAT data is not classified according to

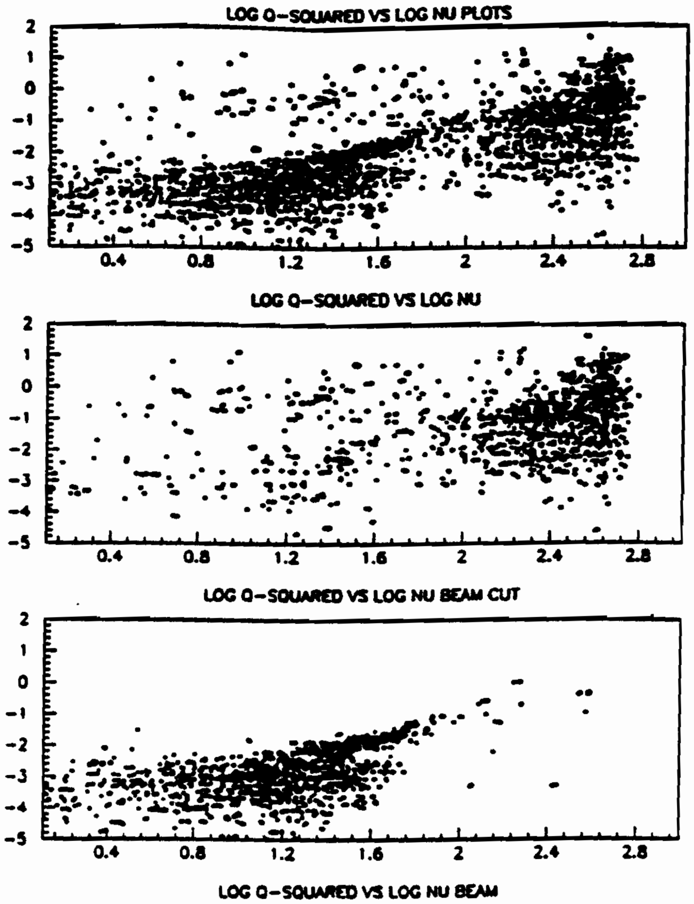

Figure 4.8: Non-interacting beam cuts from the SAT Event Filter program.

target type - that this was unnecessary was expected (since RSAT events are beam triggers) and verified during the filter production.

4.4.2 Pre-Analysis Event Selection

The full event reconstruction program was run on the remaining $\sim$ 35% of the events which survived the filter. This sample still contained events with topologies not consistent with a scatter in the target. An additional program was run to further reduce the number of events and tapes used for the final analysis. The requirements for an event to remain in the sample were that it have a primary vertex located "near" the target, and that it satisfy some minimum kinematic restrictions. The target cut allowed the vertex to be within 1.5 m of either end of the target to be included. The kinematic cuts were very loose cuts on minimum values for Q^2 (> 0.001 $(GeV/c)^2$) and ν (> 10 GeV). These requirements reduced the data sample by an

TABLE VII: EVENT FILTER RESULTS

Filter Type	Xe SAT		D_2 SAT		RSAT	
	Cut	Passed	Cut	Passed	Cut	Passed
SBT Latch	1	23531 (1.0)	1	24993 (1.0)	1	27090 (1.0)
Beam LLIN	1337	22194 (.94)	1670	23323 (.93)	497	26593 (.98)
In-time Beam	1865	20329 (.92)	2068	21255 (.91)	9822	16771 (.63)
SAT Trigger	5698	14631 (.72)	4598	16657 (.78)	753	16018 (.96)
Beam-FS Match	5697	8934 (.61)	8526	8131 (.49)	–	–
Calorimeter	3974*	4960* (1.0)	2352*	5779* (1.0)	–	–
Total	14598	8934 (.38)	16863	8131 (.33)	11073	16018 (.59)

additional factor of ~ 4 since many vertices were formed far from the target and for the SAT trigger, energy loss in the CVM field caused events with very low Q^2 to be accepted.

Also, from the analysis, it was determined that there occured in the data several run periods in which one or both of the analyzing magnets tripped off. Since the full field values were needed for proper trigger configurations, these run block periods were removed from the final sample. In addition, a preliminary intensity monitor analysis program showed that there were run periods in which the beam event scaler information was lost from the tape. These run blocks were also dropped from the final sample, causing a loss in DIS events of $\sim 2.5\%$. Since the corresponding beams were also lost, no correction was needed for either of these cuts. At the same time as the run block filter was run, both the beam (RSAT) and SAT samples had a minimum beam momentum cut of 400 GeV/c applied. This was done to remove from both samples any low momentum beams caused by SBT-PBT mismatches passed through the Event Filter.

4.4.3 Deep Inelastic Scattering Event Selection

Final selection of DIS events was made on the basis of the beam muon - scattered muon vertex kinematics. Non-interacting beams which managed to escape cuts by the SAT Event Filter were characterized by very low values of ν and Q^2 as described in the last section. The final kinematic cuts were made to eliminate these events. Also, position requirements for the vertex were made in the Event Filter. Cuts were also made keep only those events with vertices in the target.

For this analysis, the final cuts used were the following :

- $-11.80\ m < X_{vertex} < -10.4\ m$
- $Q^2 > 0.1\ (GeV/c)^2$
- $\nu > 40\ GeV$
- $x_{Bj} \geq 0.001$
- $y = \nu/E \leq 0.75$

Figure 4.9 shows the distribution of SAT events from the xenon target which satisfy the target X_{vertex} position cut.

The Q^2 cut of $> 0.1\ (GeV/c)^2$ was made to follow the SAT minimum acceptance line for ν values less than $\sim 100\ GeV$ (see Chapter 5). Also, for values of Q^2 less than this cut, the resolution of the Q^2 measurement approaches 50% or more. The ν cut is defined also by the measured resolution - at 40 GeV, $\Delta\nu/\nu < 0.50$. The x_{Bj} cut was chosen to minimize the leakage into the event sample of muon - electron elastic scattering events which are centered around x_{Bj} of 0.0005. By fitting the μ - e peak in both the xenon and deuterium data samples, it was determined that the leakage into the final event sample at $x_{Bj} \geq 0.001$ was less than 5% in both samples. The change in the ratio of xenon/deuterium cross sections was less than 1% due to this background and affected only the lowest x_{Bj} bin. The y cut was made to limit the total correction factor for the xenon cross section due to radiative events to be $\leq 40\%$. Figure 4.10 shows resolution profiles for the kinematic variables in the ranges included in this analysis.

In summary, the event selection process consisted of two stages; 1) the Event Filter stage which used a simplified version of the reconstruction program to eliminate "bad" triggers and non-interacting beams, and 2) the full event reconstruction program with kinematic and target position cuts to define the final event sample. Table VIII shows the results of the event selection from raw events to final sample for the xenon and deuterium targets. The numbers indicated

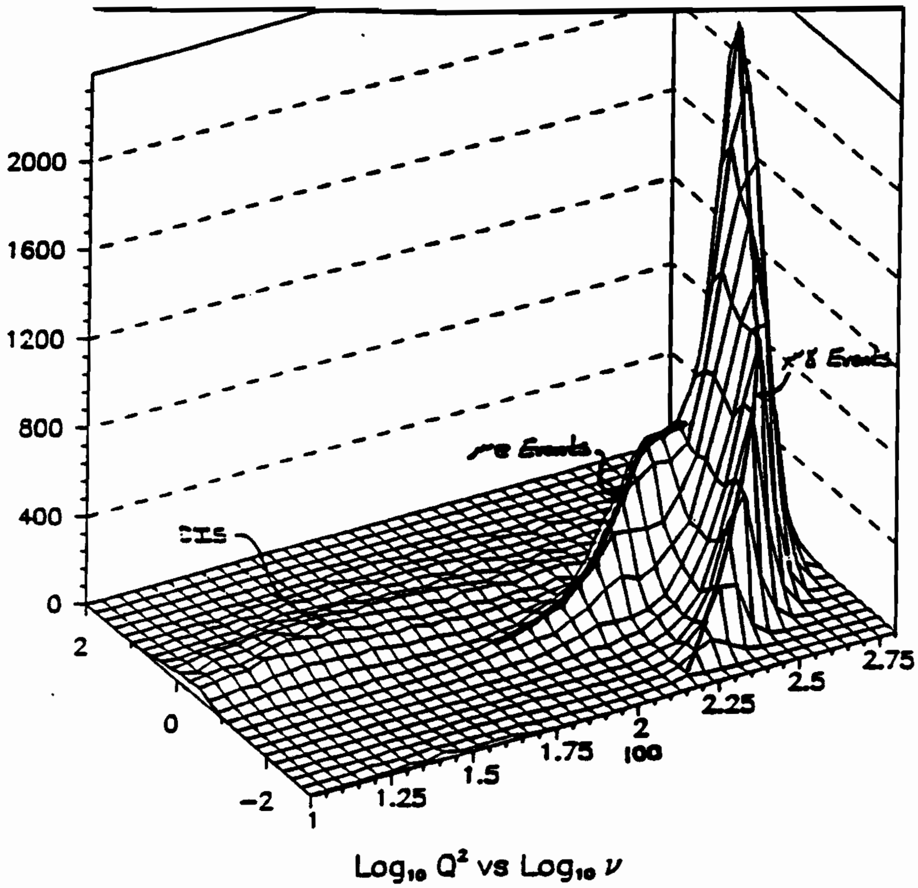

Figure 4.9: SAT Event distribution on the Q^2 - ν plane from xenon showing the dominant processes in various regions.

represent the full sample of events at each stage for each target used in this analysis. Fractions of output/input at each stage are recorded in parentheses.

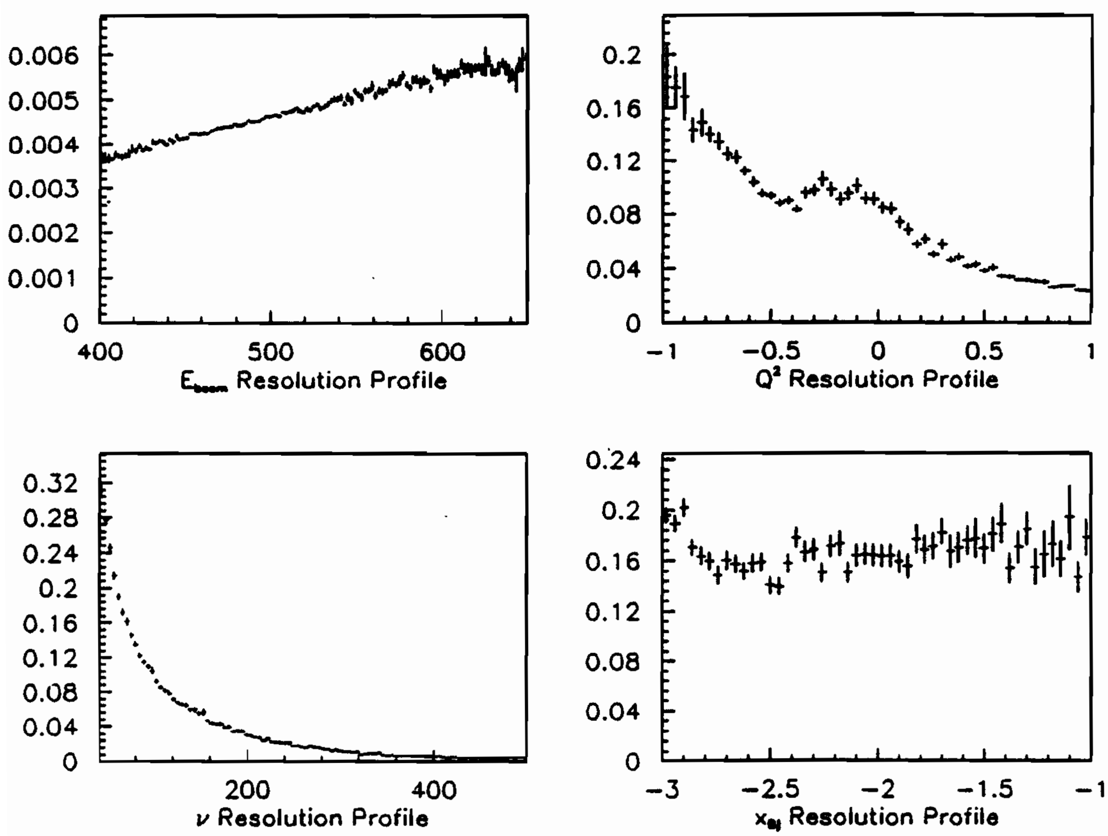

Figure 4.10: SAT kinematic variable resolution profile plots.

TABLE VIII: SAT EVENT SELECTION RESULTS

Event Selection Stage	Xenon	Deuterium
Raw Events	2076574 (1.00)	957915 (1.00)
Event Filter Cuts	789098 (0.38)	316112 (0.33)
Event Reconstruction	789098 (1.00)	316112 (1.00)
Pre-Analysis Selection		
Data Reduction	216860 (0.27)	72652 (0.24)
Run Block Filter	165309 (0.76)	51977 (0.72)
Kinematic Cuts		
Target Position	125246 (0.76)	42333 (0.81)
Q^2, ν, x_{Bj}, y **Cuts**	10276 (0.08)	9652 (0.23)
Calorimeter Cut	8511 (0.83)	8903 (0.92)
Fraction of Raw	0.004	0.009

5. CORRECTIONS TO EVENT YIELDS

In this chapter, the formulation of cross sections from the observed event yields will be described. It will include measured properties such as beam counting and target density as well as corrections to the observed number of events such as those due to reconstruction efficiencies, trigger acceptance, etc. Equation (5.1) relates the calculated cross section ratio to the measured quantities and (5.2) shows how the corrections were applied to the data.

$$\frac{(d\sigma/dx)_{Xe}}{(d\sigma/dx)_{D2}} = \frac{(dN/dx)_{Xe}}{(dN/dx)_{D2}} \times \frac{(\rho l N_A)_{D2}}{(\rho l N_A)_{Xe}} \times \frac{(N_{beams})_{D2}}{(N_{beams})_{Xe}} \tag{5.1}$$

where

$$\frac{(dN/dx)_{Xe}}{(dN/dx)_{D2}} = \frac{(dN/dx_{Full} - dN/dx_{Empty})_{Xe}}{(dN/dx_{Full} - dN/dx_{Empty})_{D2}} \times \frac{(\text{Event Yield Corrections})_{Xe}}{(\text{Event Yield Corrections})_{D2}} \tag{5.2}$$

and N represents the number of events, ρ the target density, l the target length, N_A Avagadro's number, and N_{beams} the number of beam muons counted. Event yield corrections applied to the data include :

- muon reconstruction efficiency,
- SAT trigger acceptance,
- radiative corrections or calorimeter cuts,
- non-isoscalar target correction.

These corrections will be described, with an estimate of the systematic error associated with them. When applicable, a description of the method used to determine the systematic error will be included.

5.1 Small Angle Trigger Beam Normalization

One of the more important measurements to be made in order to determine a cross section is the incident flux (N_{beams} in (5.1)). Since the SAT trigger used well-defined incident beam trajectories, only those muons which satisfied the SAT definition of "beam" should be counted for the normalization. Two independent methods were used to record the number of SAT beam muons :

1. The total number of SAT beams was recorded in a scaler module; and
2. SAT beam events were written to tape after being pre-scaled by a pre-determined constant factor.

These two methods were compared and their ratio was monitored throughout the data collection run.

5.1.1 Small Angle Trigger Beam Scalers

The number of incident muons satisfying the SAT beam definition was recorded with each event and at the end-of-spill by scaler modules. The beam counting information was stored in a variety of ways, for example, as the number of beam counts for a particular type of beam since the last event of a specific trigger type. In this way, each type of triggered event could be normalized by its corresponding beam type.

5.1.2 RSAT Beam Triggers

A prescaled number of SAT beam events was written to tape for analysis. These events were then subjected to the beam tests in the Event Filter program (see Section 4.3). Since the RSAT triggers were related to the scaled beams by the pre-scale factor, the corresponding number of scaled beams could then be subtracted from the scaler count, leaving the correct number of scaled beams for the SAT interactions.

5.1.3 Beam Scaler - RSAT Beam Trigger Correlation

During data collection, two problems were present in the RSAT trigger which caused the corresponding number of beams indicated by this method to be too high. The first problem, which was present throughout the entire run, was an increase in the number of RSAT triggers recorded caused by the inclusion of out-of-time events in the sample. The out-of-time events were caused by an intermittent increase in the width of the beam signal from a NIM logic module. This increase (~ 5 *nsec*) was large enough to allow signals from the wrong RF time bucket to trigger the experiment. The additional out-of-time beams made up $\sim 30\%$ of the total RSAT triggers. The beam scalers were not affected by this problem, and so the number of RSAT triggers had to be modified to keep only those which were in the correct RF bucket. Several methods of determining the timing status of events were tried and compared. The consistency of these methods verified the correctness of the in-time evaluation. Upon correcting the RSAT triggers by eliminating out-of-time beams, agreement was achieved between the beam scalers and the RSAT triggers.

The second problem arose during the run; it complicated the determination of the number of in-time RSAT triggers. A reflection developed in the input to the trigger-forming logic module on the cable from the RF timing module. The time of this reflection was 3 RF buckets + 3 ns ($\sim 60ns$) later than the original signal. Figure 5.1 shows the effect of this reflection on the trigger timing as recorded by a TDC on one of the beam trigger hodoscopes.

As can be seen, this reflection affected both the in-time and out-of-time triggers, but to a varying degree. The reason for the difference in the relative heights of the signals can be seen in Figure 5.2.

Note that the original RF signal and its reflection are both within the normal width beam signal, and therefore, the relative heights of these two are the same. The important conclusion from this is that for the in-time beam trigger signal, the reflection in the RF signal caused exactly double the number of triggers to be recorded. Effectively, the pre-scale factor in the RF signal was halved, allowing twice as many RF buckets to present themselves as trigger candidates. However, it can be seen in Figure 5.2 that when the width of the signal was increased due to the first problem mentioned, the original RF signal was in coincidence with

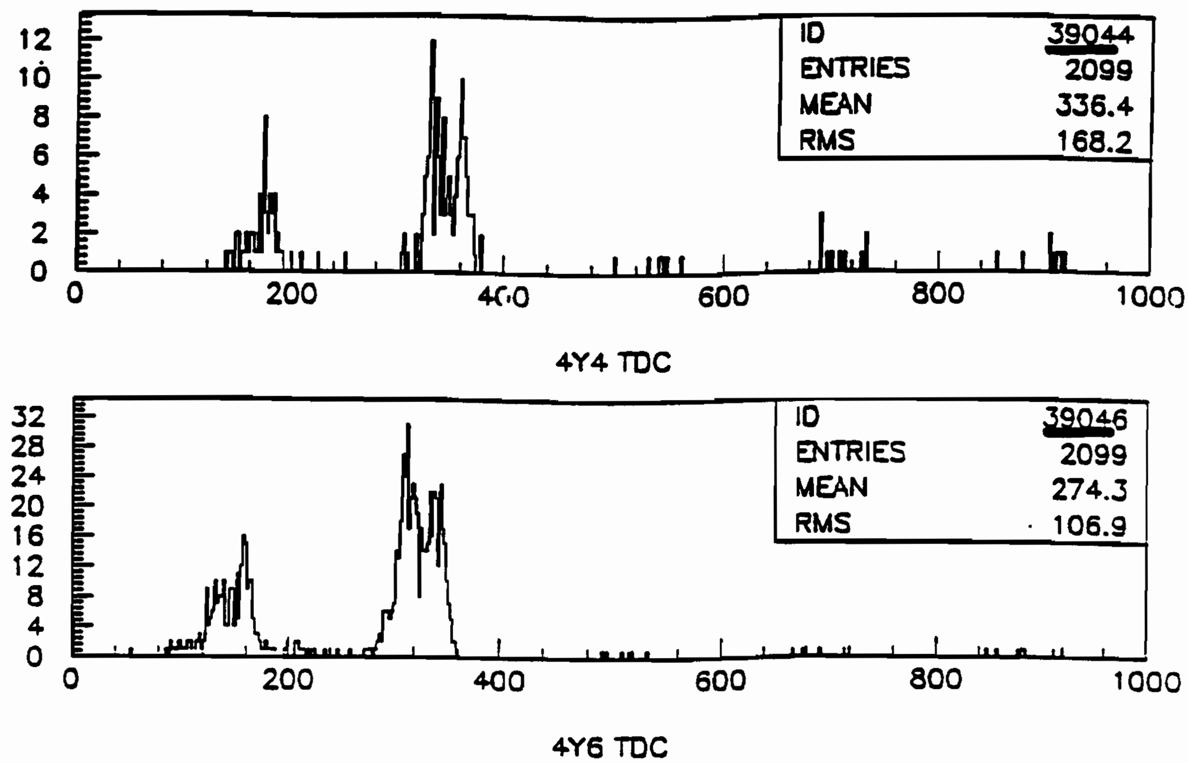

Figure 5.1: TDC spectrum from two hodoscope elements in beam hodoscope plane SBT4Y. The in-time events are those in the right-most distribution, and the out-of-time events are those in the left-most distribution.

the beam signal, but the reflected RF was just on the edge of the beam. Fortunately, the wider beam signals are from out-of-time beams as mentioned above, so the undetermined number of triggers caused by the reflected RF signal was not important. Since the reflection was not present on the signal to the scaler latches, the beam scalers were not susceptible to this problem, and therefore counted only those beams from the original RF signal.

In summary, the beam scalers counted the correct number of beams seen by the apparatus. Neither out-of-time triggers nor reflected signals were seen by the beam scaler latches. However, both of these problems affected the RSAT beam triggers written to tape. To correct the trigger problems, an alternative method selected from several successful candidates was used to determine the timing properties of all RSAT beam triggers. The in-time RSAT beam triggers as determined externally were matched by the beam scaler counts with no further corrections

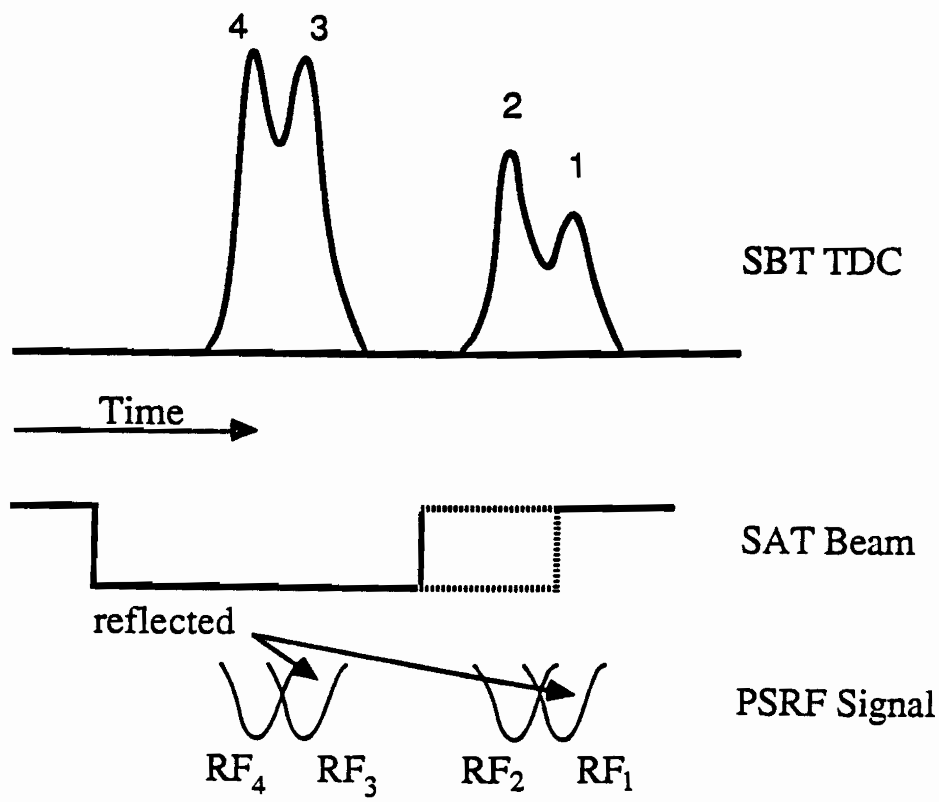

Figure 5.2: Coincidence of beam and RF signals.

until the reflected RF signal appeared. After correcting for out-of-time triggers, the pre-scale factor for the RF was adjusted by exactly a factor of $\frac{1}{2}$ in order to compensate for the doubled number of in-time RSAT beam triggers caused by the RF reflection. In this way, the number of RSAT triggers and beam scaler counts agreed to 0.5%.

5.1.4 Beam Normalization Parameters

For each SAT event, the number of beams since the last event was written to tape with all of the event information. Therefore, the incident flux needed to produce a deep inelastic scatter was obtained by accumulating the beams stored with each event in the sample. The actual accumulated flux was reduced by modifications to the beam sample accepted for analysis. Events were subjected to 3 cuts which reduced the total number of beams incident on the targets. The fraction of RSAT triggers remaining after these cuts was determined for each data taking sub-period of typically 4 hours (denoted as a Run Block). This fraction was then used to modify the total number of beams counted by the event scalers to form the beam normalization parameter. The following cuts were applied to the beams in both the RSAT and SAT triggered events :

Event Filter Cuts

The SAT Event Filter, which included some tests on the beam, was run on RSAT triggered events as well as SAT events (see Section 4.4).

Beam χ^2 Probability Cut

After beam pattern recognition and track fitting, the quality of the fit was checked to ensure that the track was acceptable based on its χ^2 probability. The cut value was set at 0.001, which eliminated approximately 3% of the reconstructed beams (see Figure 5.3).

Beam Momentum Cut

A minimum beam momentum requirement designed to help eliminate bad RSAT beams was also imposed. In the raw sample of SAT and RSAT triggered events, a hole in the beam hodoscope aperture caused by inactive hodoscope elements allowed low momentum beams to pass the trigger requirements whenever a random signal from a hodoscope element in the trigger acceptance was seen. Normally, this did not affect the trigger since the random singles rate from most of the hodoscope elements was negligible. In this case, however, one of the hodoscope elements included in the SAT beam combinations (from SBT4Y) had a singles rate which was $\sim 10\%$ of the trigger rate. This resulted in a low momentum tail ($< 400\ GeV/c$) on the beam momentum distribution for raw SAT events of about 20%. Most of these events were cut by the SAT Event Filter, but in order to gaurantee that none entered the final sample, a minimum momentum cut of 400 GeV/c was applied.

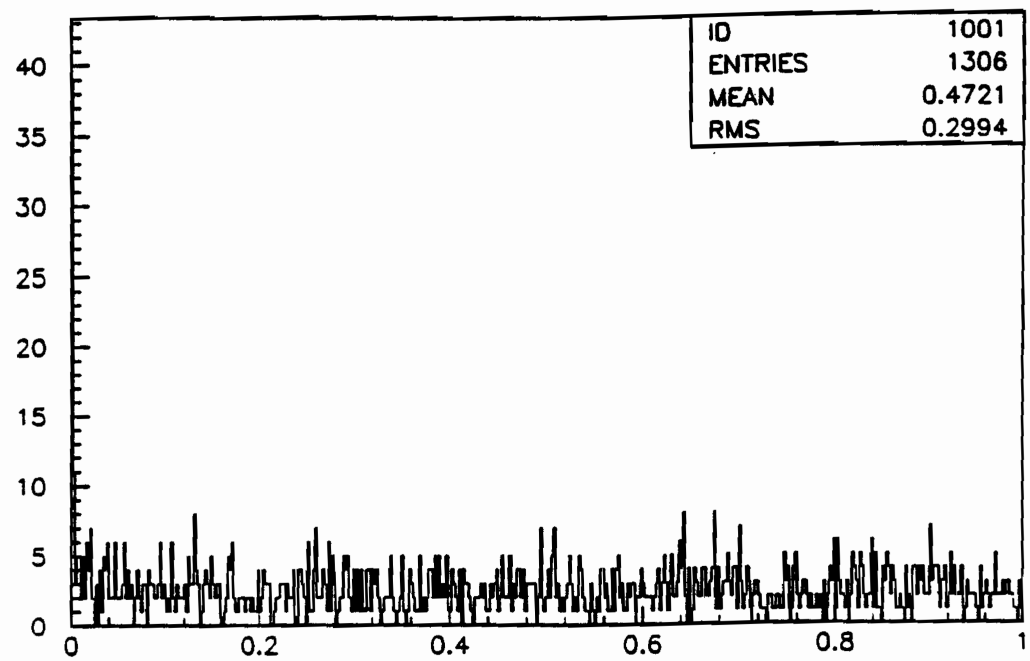

Figure 5.3: χ^2 probability of reconstructed beam tracks.

Systematic Error on Normalization

The level of agreement between the two methods used to determine the beam flux provided an indication of the systematic error associated with the beam normalization factor. For both the deuterium and xenon target runs, the estimate of systematic error on the beam normalization was 0.5%.

5.2 Target Density

In addition to the beam count, the target thickness is needed to determine the luminosity of the experiment. The densities of the xenon and deuterium targets were monitored by continuous temperature and pressure measurements which were recorded on strip charts.

5.2.1 High Pressure Gaseous Xenon Target

The gaseous xenon target consisted of a target vessel filled to a pressure of $\sim 210PSI$ and kept at a temperature of $\sim 20°$ C. The pressure was monitored continuously and measured to within 0.25 PSI. The temperature monitor measured the temperature to $\pm 0.1°$ C. The resultant density calculation was done using a ideal gas equation of state modified by compressibility corrections. The density was calculated for 5 different time periods for the full xenon target data. One such time period included data taken when the target had developed a leak; this data was not used in this analysis. Figure 5.4 shows the calculated density as a function of time with the 4 constant periods and leaking target indicated.

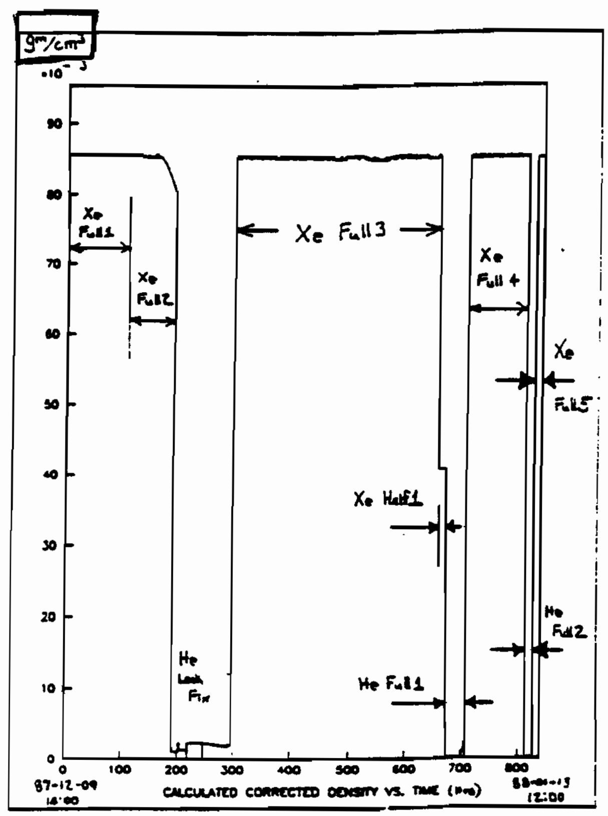

Figure 5.4: Xenon target density versus time. Indicated on the plot are the periods designated as full target.

The average density of the high pressure xenon for the 4 running periods labelled as "full" was calculated to be 0.08535 g/cm^3.

5.2.2 Liquid Deuterium Target

The stability of the liquid deuterium target was also monitored by constant measurements of the temperature and pressure. The resultant target density was determined to be 0.16264 g/cm^3.

5.2.3 Systematic Error on Target Density

The following table shows the measurement of the target density for the gaseous xenon and liquid deuterium targets along with estimates of their associated statistical and systematic measurement errors.

TABLE IX: TARGET DENSITIES

Target	Density (g/cm^3)	$\sigma_{Stat.}$	$\sigma_{Syst.}$
Xenon	0.08535	0.00016	0.00015
Deuterium	0.16264	0.00001	0.00050

5.3 Small Angle Trigger Geometrical Acceptance

Since the xenon and deuterium targets had different sized vessels, in principle, the geometrical trigger acceptance must be known for each target. In addition, changes in the beam phase space could alter the acceptance as a function of time if different combinations of beam and veto regions were dominant for the two targets.

The geometrical acceptance was calculated for each target vessel by generating Monte Carlo events and applying the SAT requirements to the resultant scattered muon. Also, a test run of the Monte Carlo was made for each target in the region where they overlapped to verify that the acceptance was the same in that region. The position of the targets along the beam direction was measured by two independent methods which agreed to within 1 cm.

5.3.1 Xenon Target

The xenon target vessel was designed to contain xenon gas at high pressure (210 PSI). The target walls were relatively thick 10μm mylar with 1 mm thick end caps. The target vessel was

113 *cm* long and had a diameter of 14 *cm*. This information was included in the Monte Carlo program along with the relative alignment information. The Monte Carlo generated 140000 events in various regions to cover the kinematic range used in this analysis and the results are shown in Figure 5.5 as a function of Q^2 and x_{Bj}.

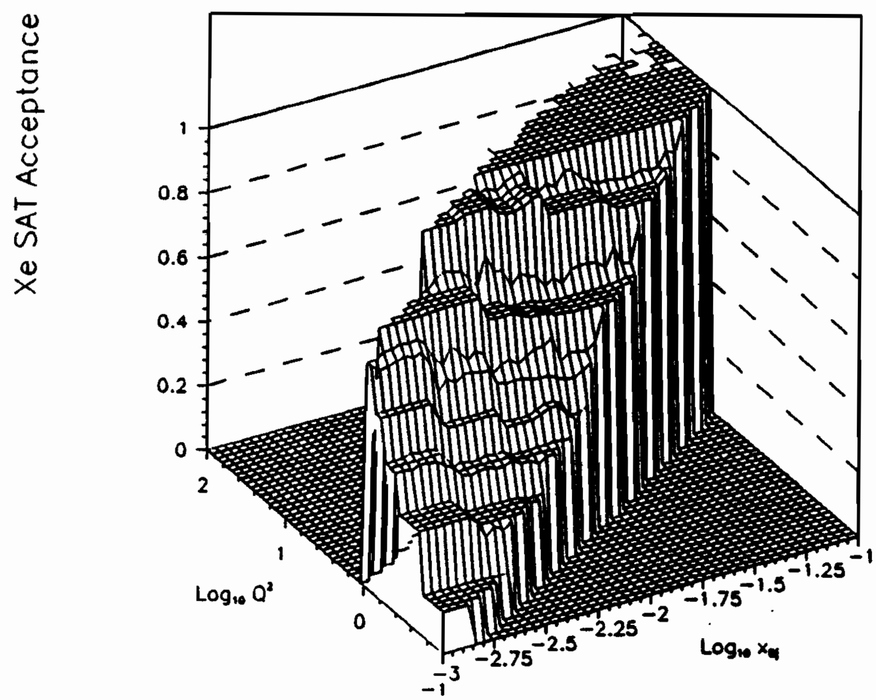

Figure 5.5: SAT geometrical acceptance for the xenon target vessel.

5.3.2 Deuterium Target

The deuterium target vessel was made to acocmodate liquid deuterium and hydrogen. The walls of the target vessel were made of 10 μm mylar uniform throughout the entire vessel. The target was 115 cm long and 16 cm in diameter. The target vessel was surrounded by a Rohacell jacket to provide insulation. For this target, again, 140000 Monte Carlo events were generated to check the SAT acceptance. Figure 5.6 shows the acceptance for the deuterium target as a function of Q^2 and x_{Bj}.

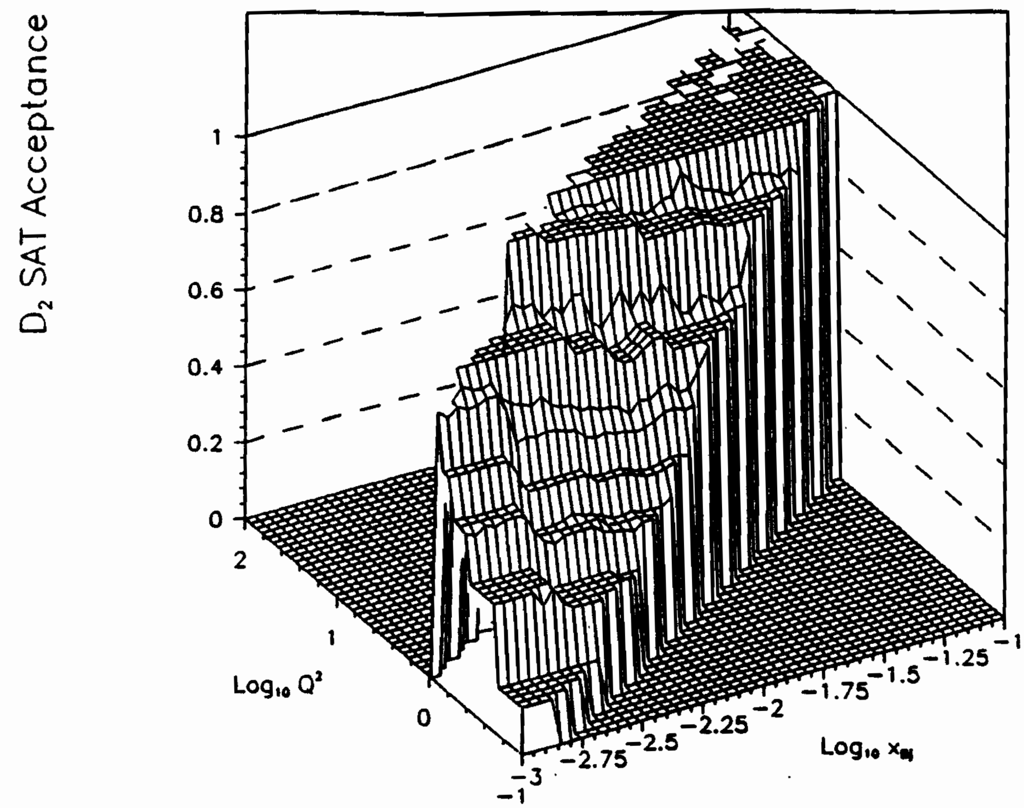

Figure 5.6: SAT geometrical acceptance for the deuterium target vessel.

5.3.3 Systematic Error on Trigger Acceptance

The measurement of the SAT trigger acceptance was, like the trigger itself, dependent on the relative alignment of the SBT and SMS hodoscopes. Therefore, the largest source of systematic error for this correction was determined by the degree to which the alignment was known. During the run, the SMS hodoscopes were monitored continuously in order to determine whether their alignment changed. Also, since many intermediate elements of the SAT trigger were scaled, close watch on the veto counts would indicate movement of the veto region and, therefore, the SMS hodoscopes. The maximum change in the SMS hodoscopes seen during the entire 1987-88 running period was 2 mm in only one plane (incidentally, this plane was not used in any SAT veto definition). The average shift in SMS position observed by the dedicated alignment runs was 0.7 mm. This shift was used to determine the estimate of systematic error in the SAT geometrical acceptance. Previous to the Monte Carlo run, alignment constants were once again checked for the SMS hodoscopes. The final result for each target vessel was 0.75% which added in quadrature yields a systematic error on the ratio of xenon to deuterium cross sections of 1.05%.

5.4 Scattered Muon Reconstruction Efficiency

Since the data from the two targets was taken at different times, it was important to know the time dependence of the muon reconstruction efficiency. It was found that the performance of the muon reconstruction did change over time and that the change was due to changing chamber efficiencies in the region of the scattered muon.

5.4.1 Time-Dependence in Muon Reconstruction

The scattered muon reconstruction efficiency was determined separately from RSAT beam triggers and SAT triggered events. The RSAT events were particularly useful in determining the reconstruction efficiency in the SAT beam region. This was because of the beam selection and veto projection using specific SBT-SMS hodoscope element combinations stored in the SAT Trigger Matrix modules. For each RSAT event, the position of the scattered muon in the SMS counters was known from the beam-veto projection. Therefore, using RSAT events with SMS projections at the positions defined by the veto trigger matrices, the muon reconstruction efficiency in the beam region of the Forward Spectrometer was measured. Figure 5.7 shows the time dependence of the reconstruction efficiency for RSAT events from the deuterium running period. The solid points represent the efficiency of forming a muon projection in the SMS detector. The dotted points represent the efficiency for reconstruction of a muon track in the Forward Spectrometer and the dashed line is the average measured chamber efficiency for the PC chambers.

As can be seen in Figure 5.7, the muon reconstruction efficiency in the beam region changes in the deuterium data by $\sim 5\%$. The reconstruction efficiency of $\sim 95\%$ shown at the beginning of the deuterium running period (left-hand side of Figure 5.7) has been reproduced by the Monte Carlo for beam events using chamber efficiencies determined for this time period.

The estimate of reconstruction efficiency for SAT events was not as straight-forward since

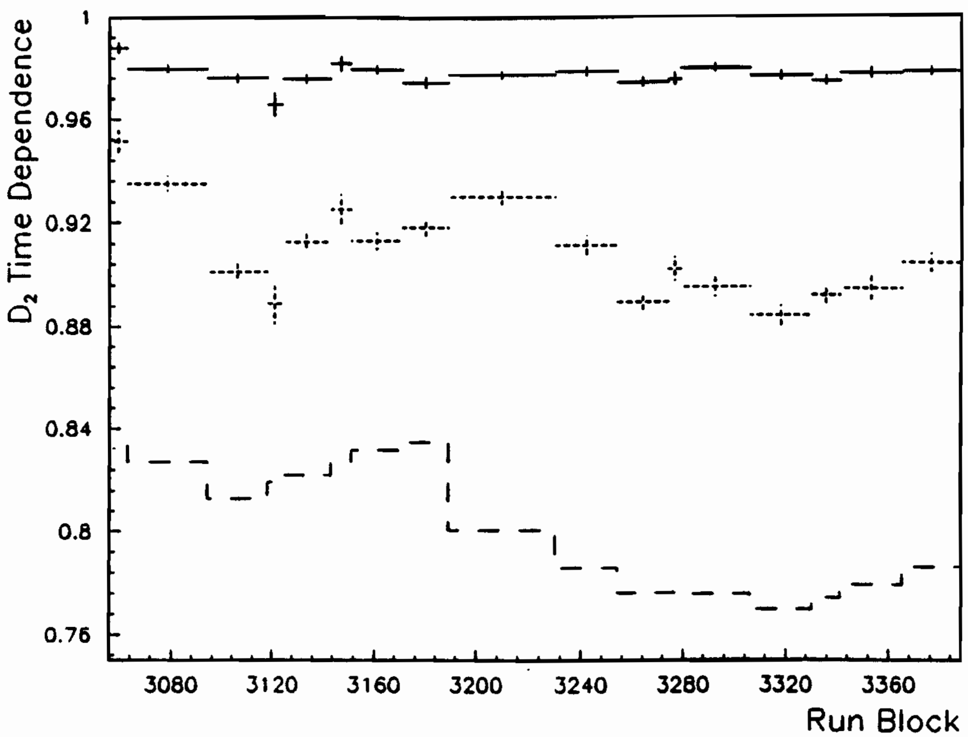

Figure 5.7: Time dependence of muon reconstruction efficiency - RSAT beam events taken during the deuterium runing period.

the position of the scattered muon in the SMS and PTM detectors was not known from the beam-veto projections. However, the measured efficiencies for the PTM and SMS detectors were near 100% and showed no time dependence. The reconstruction efficiency for muon projections with these detector efficiencies was also $\sim$ 100%, and the efficiency for matching muon projections with a muon candidate in the Forward Spectrometer was > 99%. These reconstruction efficiencies were verified by Monte Carlo using the SMS and PTM measured efficiencies. An estimate of the reconstruction efficiency for scattered muons in the Forward Spectrometer was obtained by requiring one and only one LPRO projection in each view (Y and Z), and then counting the number of events in which an LMUN muon match was formed. Figure 5.8 shows the time dependence of the scattered muon reconstruction efficiency in SAT and RSAT events for the deuterium and xenon data taking periods.

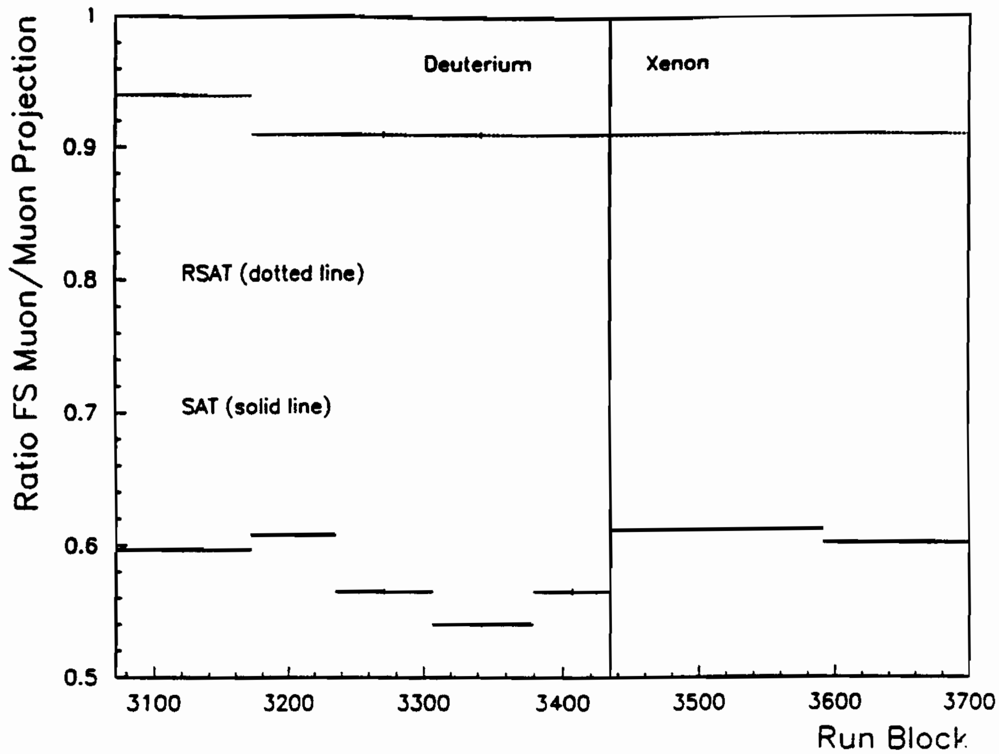

Figure 5.8: Time dependence of muon reconstruction efficiency - SAT and RSAT events in xenon and deuterium.

Note that the same time dependence seen in the RSAT data is also seen in the SAT events, but that the change during the deuterium running period is more pronounced ($\sim$ 8%). It is important to note that the scattered muons in SAT events do not necessarily travel through the same detector regions as the beam muons do in RSAT events. Therefore, the correction for time dependence of the scattered muon reconstruction requires a full position and time dependent measurement of the chamber efficiencies in the Forward Spectrometer.

5.4.2 Scattered Muon Pattern Recognition Efficiencies

The search for loss in efficiency to explain the time dependence in the deuterium data started with the measurements done by the pattern recognition program on the wire chamber efficiencies. This program calculated average chamber plane efficiencies in a somewhat biased way (since tracks were required to make efficiency measurements), but the results qualitatively reflected the true chamber efficiency changes. Figure 5.7 shows that the average efficiency of the PC MWPC's changed at the same time that the drop in muon reconstruction efficiency was seen. As mentioned in Chapter 4, the PC chambers were essential for the reconstruction of all scattered muon trajectories. A check of the reconstructed muon trajectory coordinates in the PC chambers revealed a time feature of the chambers that was known but for which there was no previous indication of modified chamber performance. It was seen that in the coordinate regions defined by two rings centered in the PC chambers, the muon reconstruction efficiency was significantly reduced in the second half of the deuterium data-taking period as compared to that in the first half. The central region showed a much less pronounced change; this is the region where unscattered muon beams were found. This explained the reduced inefficiency seen in the RSAT data. Figure 5.9 shows the scattered muon reconstruction efficiency ratio for the two deuterium data collection periods as a function of radius in the PC chambers.

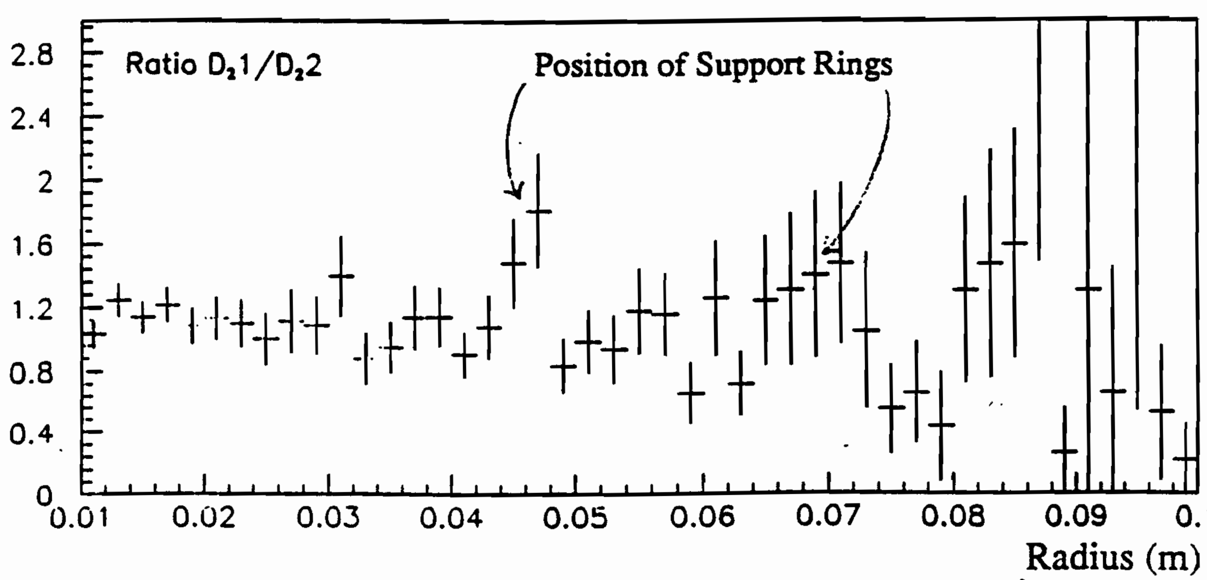

Figure 5.9: Ratio of muon reconstruction efficiency for the two deuterium data periods versus radius.

The kinematic distributions also reflected the change in efficiency. Figure 5.10 shows the ratio of x_{Bj} and Q^2 distributions for the second half of the deuterium run (D22) compared to the first half (D21) before and after the radial efficiency correction.

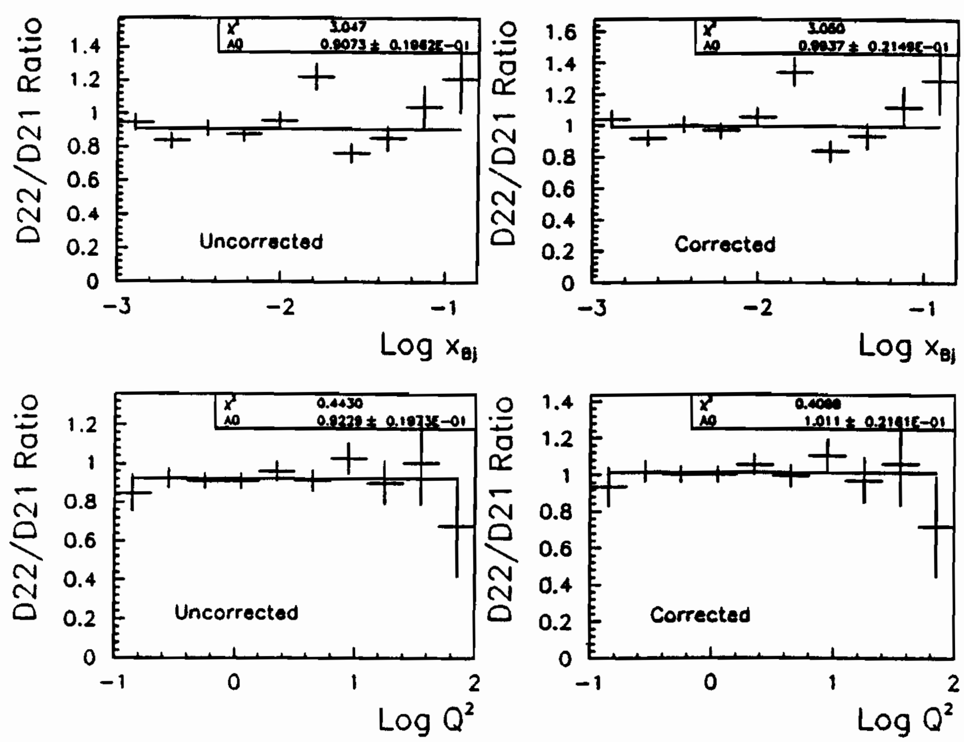

Figure 5.10: Ratio of kinematic variable distributions for the deuterium data set before and after the radial correction.

The source of the time dependent PC plane efficiency was traced to a change in the gas mix which occured when the alcohol bubbler ran out of alcohol and was not refilled for several days. The absence of alcohol, commonly used as a quencher (not by thirsty Physicists, but to slow down ionization in the gas) in MWPC's, allowed spacecharge to build up around the rings defining the separated cathode plane regions (a design feature to allow deadening of specific regions of the chamber), reducing the electric field seen by the ions in the gas in this region and thus lowering the chamber efficiency. Figure 5.11 shows a radial map of the chamber efficiency of PC plane PC2Y for the second half of the deuterium data collection, clearly indicating the

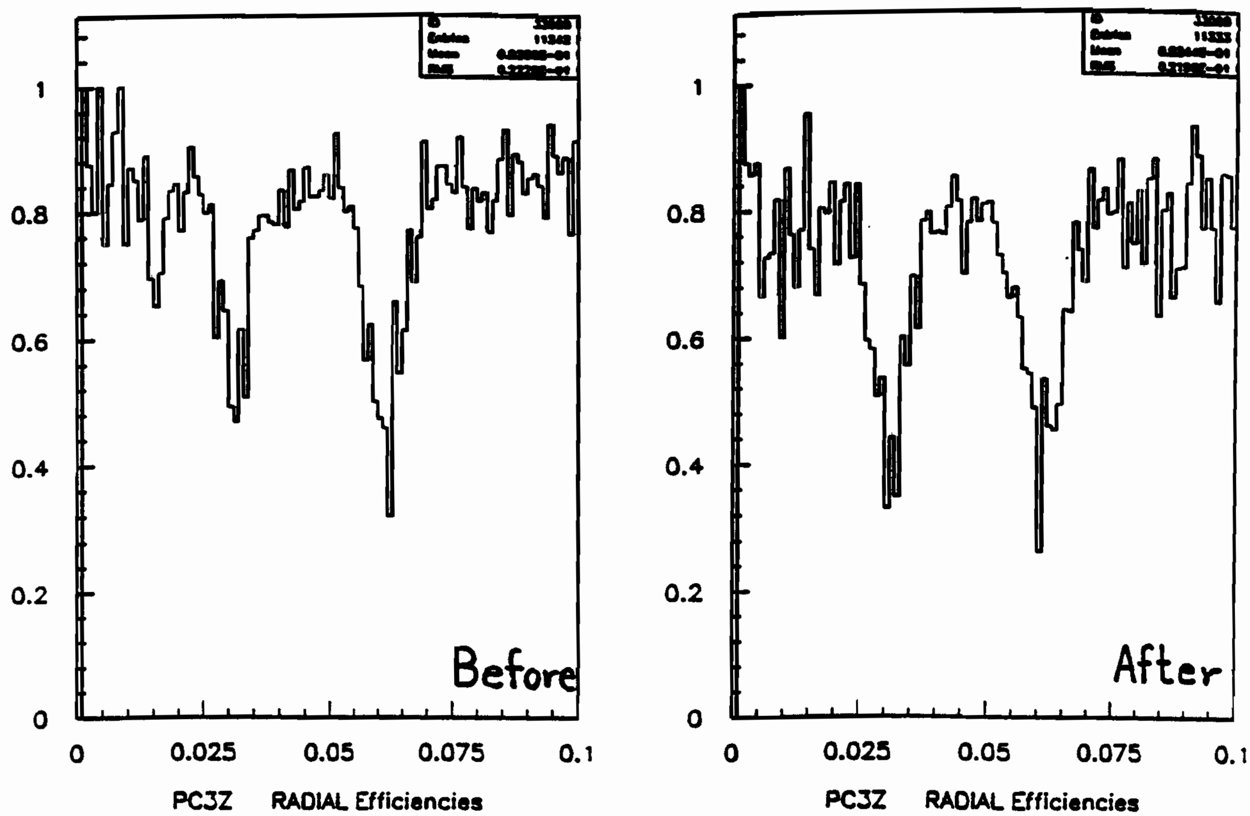

Figure 5.11: PC2Y radial efficiency measurements before and after the change in the chamber gas mixture.

rings of reduced efficiency.

5.4.3 Xenon/Deuterium Relative Reconstruction Efficiency

Prior to the start of the xenon data-taking period, the alcohol bubbler was refilled in the PC gas system. From Figure 5.8, it can be seen that the RSAT muon reconstruction efficiency appears to have returned to its previous value.

5.4.4 Systematic Error on Muon Reconstruction Efficiency

Since this analysis compares the ratio of the two targets, the correction factors have been normalized to the first half of the deuterium data taking period. The muon reconstruction efficiency for this period has been estimated by the Monte Carlo to be $\sim 90\%$ for SAT scattered muons. The systematic error on the muon reconstruction efficiency contains contribution from two parts :

1. The correction applied to fix the deuterium time-dependence; and

2. The correction on the relative reconstruction efficiency of xenon to deuterium data.

The first estimate was made by comparing the kinematic distributions obtained in the two parts of the deuterium data-taking period (see Figure 5.10). The systematic error on the reconstruction efficiency correction for the deuterium data was $< 1\%$ based on these results.

The second estimate was made using only information from the RSAT efficiency measurements. Based on these measurements, no correction was applied to the xenon data since the RSAT muon reconstruction during the xenon running period closely matched the deuterium before the change. As noted previously, however, this measurement is not in the region of the scattered muon. The measurement only shows the degree to which the PC chambers returned to their previous operating conditions after the alcohol bubbler was refilled. Using the ratio of reconstruction efficiency in the scattered muon region of the PC's compared to the beam region, the difference in the reconstruction efficiency could be as high as 7%. Therefore, the systematic error on the relative reconstruction efficiency of the xenon to deuterium data taking periods was estimated to be $+7\%$ and probably no less than -1% since the reconstruction efficiency does not indicate a marked improvement.

Adding the time dependent and relative errors in quadrature, the overall systematic error on the muon reconstruction efficiency correction to the xenon/deuterium cross section ratios was estimated to be $+7\%$ and $\sim -1\%$.

5.5 Empty Target Subtraction

Data were taken with the target vessels emptied and subsequently subtracted from the full target data. This was necessary for the measurement of the inclusive cross sections since the position resolution of the primary vertex along the X coordinate was typically ± 20 cm. Figure 5.12 shows a superposition of full and empty target distributions as a function of the X coordinate of the vertex for the xenon target vessel (the corresponding distributions for deuterium are similar).

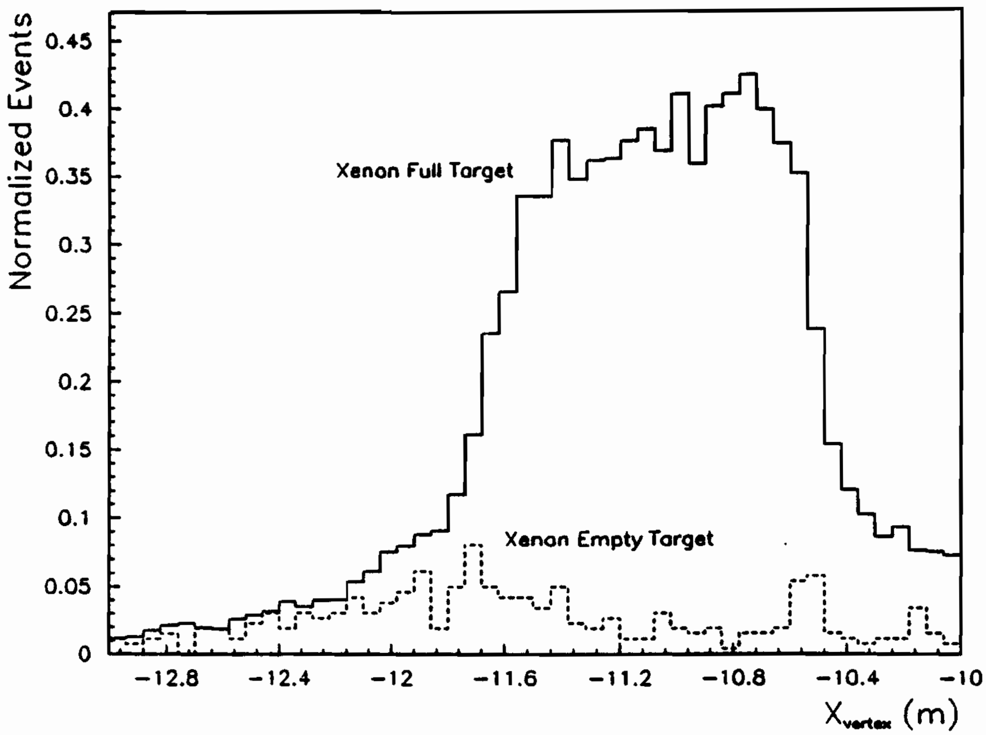

Figure 5.12: Xenon full and empty target distributions shown as a function of the position along the beam.

Figure 5.13 shows the correlation of target position with x_{Bj} for the empty target data for the deuterium target vessel.

Notice the large number of entries at $x_{Bj} \sim 0.001$ which occur at a target position of ~ -12 m. These events also showed activity in the electromagnetic calorimeter indicative of single photons interpreted as being due to bremsstrahlung. The source of these events was an aluminized mylar window located at -12 m. The resultant enhancement of events at low x_{Bj} occured in both the deuterium and xenon empty target data.

5.5.1 Xenon Results

Figure 5.14 shows the fraction of events in the xenon full target distribution originating from interactions other than those from the xenon target gas as a function of x_{Bj}.

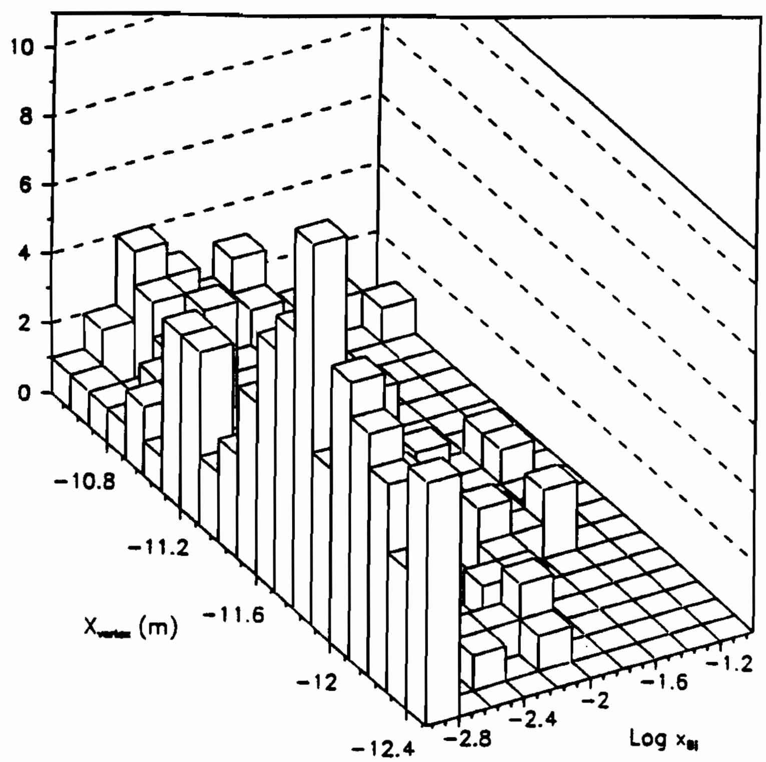

Figure 5.13: X_{vertex} versus x_{Bj} for empty target data from the deuterium target vessel.

The appropriate number of events for each x_{Bj} bin was subtracted from the full target distribution to form the final sample of events from the xenon in the target vessel. The uncertainty on this subtraction method was constrained by the limited statistics from the empty target running period and was $\sim 1\%$.

5.5.2 Deuterium Results

Figure 5.15 shows the fraction of events in the deuterium full target distribution originating from interactions other than those from the deuterium target liquid as a function of x_{Bj}.

The appropriate number of events for each x_{Bj} bin was subtracted from the full target distribution to form the final sample of events from the deuterium in the target vessel. The uncertainty on this subtraction method was again constrained by the limited statistics from the empty target running period and was also $\sim 1\%$.

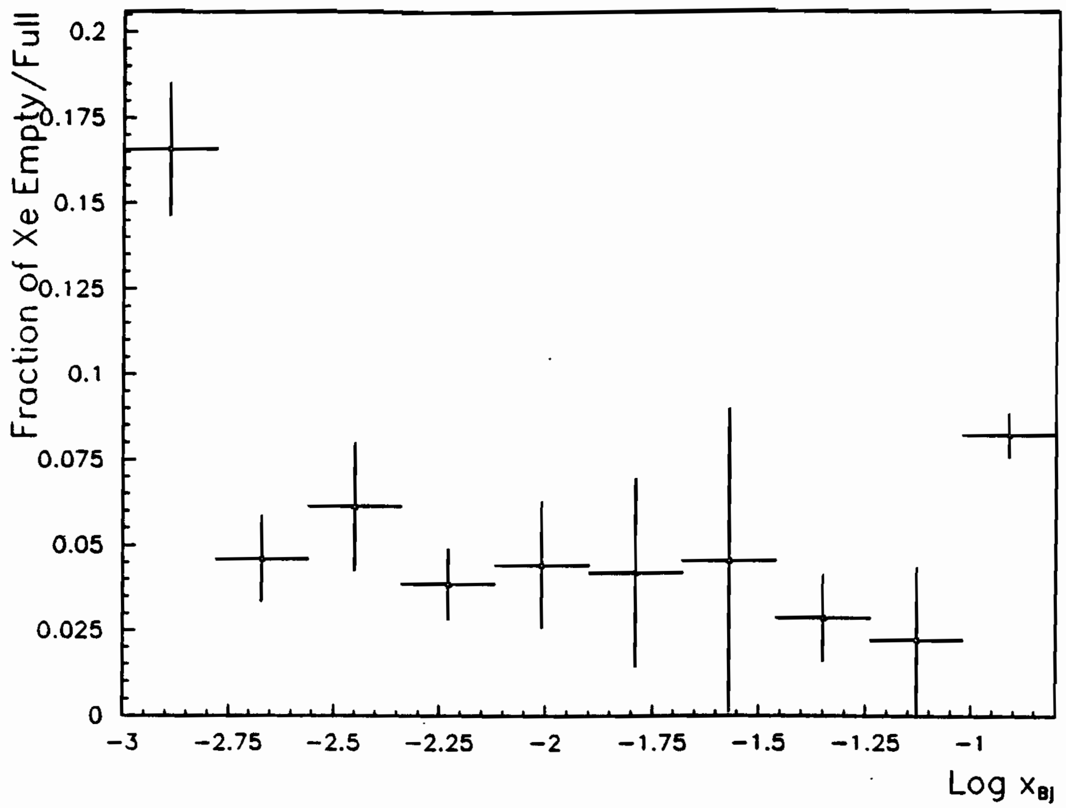

Figure 5.14: Fraction of events originating in the xenon target vessel.

5.5.3 Systematic Error on Empty Target Subtraction

The above estimates of the uncertainty in subtracting events from the target vessels and other material were added in quadrature for each target vessel to determine the systematic uncertainty for this correction on the Xe/D_2 cross section ratio. The result was a contribution of 1.4% to the total systematic error.

5.6 Corrections for Radiative Processes

The single largest source of corrections to the raw event yields at $x_{Bj} < 0.1$ was due to processes in which the beam and/or the scattered muon radiated a bremsstrahlung photon while passing the target nucleus. The probability of photon emission depends on the number of electrons in the target atom ($\propto Z^2/A$), and therefore, the correction is relatively large for heavy nuclear targets. In this analysis, two independent methods were employed to identify and correct for

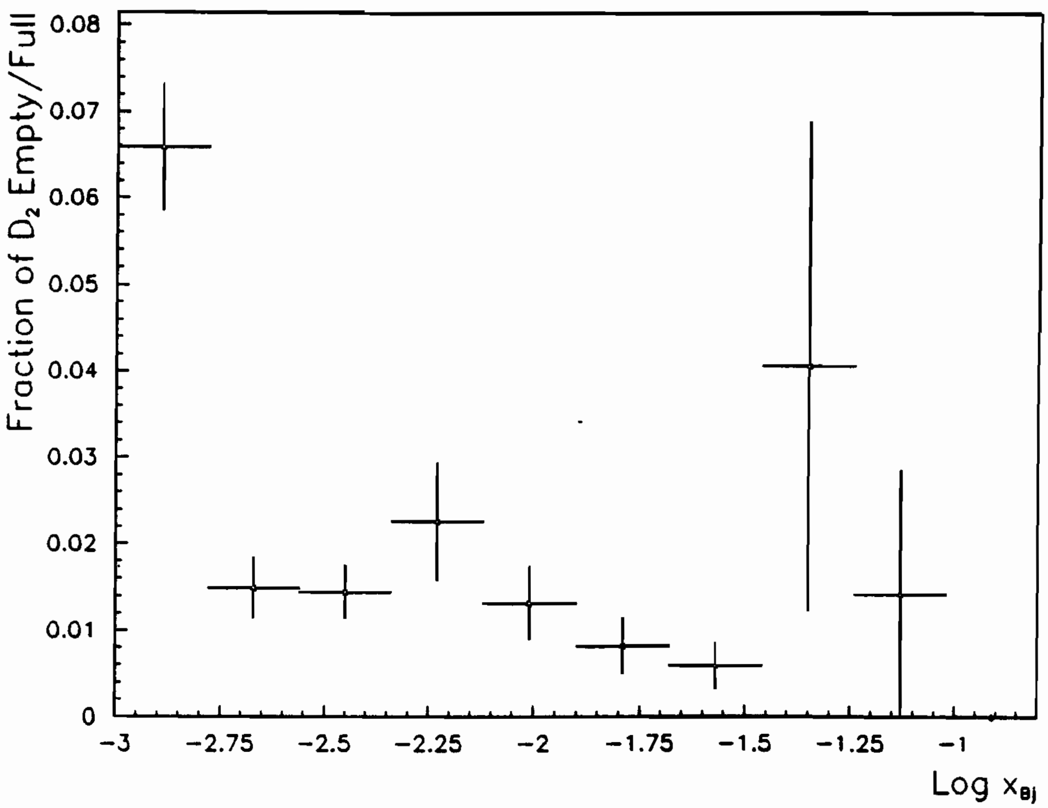

Figure 5.15: Fraction of events originating in the deuterium target vessel.

the radiative events present in the DIS sample.

Figure 5.16 shows diagrams of typical radiative processes (up to order α_{em}^2) which contribute to the measured cross section.

The first two processes, 5.16a and 5.16b, are known as the vertex correction and vacuum polarization, respectively. While they are important for absolute cross section measurement and F_2 extraction, they are independent of the number of nucleons (A), and therefore, are not important in the calculation of cross section ratios.

Processes 5.16c and 5.16d, which represent bremsstrahlung from the beam and scattered muon, respectively, are target dependent and are the largest source of radiative background in a heavy nuclear target. In addition, these two processes come in 3 types :

1. Coherent - where the nucleus does not break up;

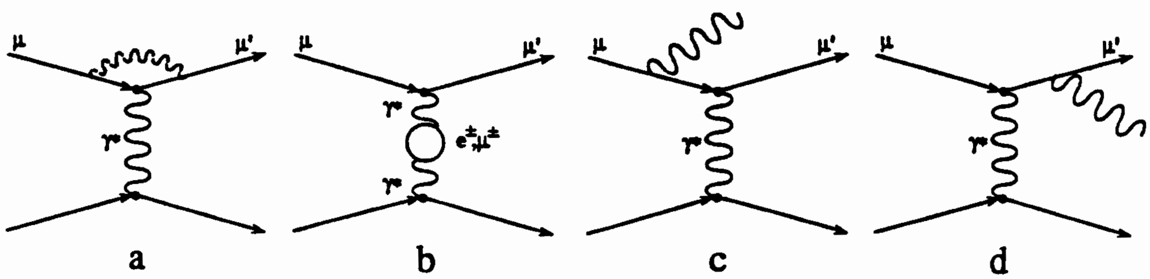

Figure 5.16: Radiative processes of up to order α_{em}^2 which contribute to the measured cross section for muon inelastic scattering.

2. Quasi-elastic - where the nucleus breaks up but the constituent nucleons do not break up; and

3. Inelastic - where the nucleons break up and produce hadrons.

The coherent and quasi-elastic processes dominate the measured cross section at high ν and low Q^2 (or small angles since Q^2 and ν are related to θ by equation (3.1)) for heavy nuclear targets. In this experiment, $\sim 60\%$ of the SAT events from the xenon target for $\nu > 400\ GeV$ contained bremsstrahlung photons resulting from these two types of interaction. Since no hadrons are produced in these interactions, very little of the energy transfer is taken up by the target (only to excite nuclei in quasi-elastic scattering). Therefore, all of the available energy goes into the bremsstrahlung photon.

The selection of these events by the SAT was enhanced by the large loss of energy (ν) at low Q^2 by the muon in the target. Since interactions in the target occured inside a magnetic field, the focussing condition was destroyed (the energy independence of the focussing condition is only maintained if the particle has constant energy throughout the field region). Therefore, the SAT trigger was dominated at high ν by muon - nucleus bremsstrahlung in the xenon target. Another source of low Q^2, large energy loss events was muon - electron elastic scatters, which also were prevalent in the SAT data, although not in the kinematic region of this analysis (see Section 4.4).

The inelastic process also generates photons which change the measured kinematics of the scattered muon. Of course, this process depends on the structure function of the nucleons in the two targets, and is, therefore a weak function of A. The bremsstrahlung photon in these events shares the available energy, ν, with the hadrons produced in the break-up of the target nucleon. Since these events are generated according to the DIS cross section, they display a $1/\nu$ dependence, and represent an approximately constant fraction of the events (compared to DIS) at all ν.

Figure 5.17 shows the relative contribution to the measured cross section in xenon as a function of $y = \nu/E$ at $x_{Bj} = 0.005$ for the 3 types of radiative events described above. The coherent and quasi-elastic processes are included together since they are very similar in appearance in the experimental apparatus.

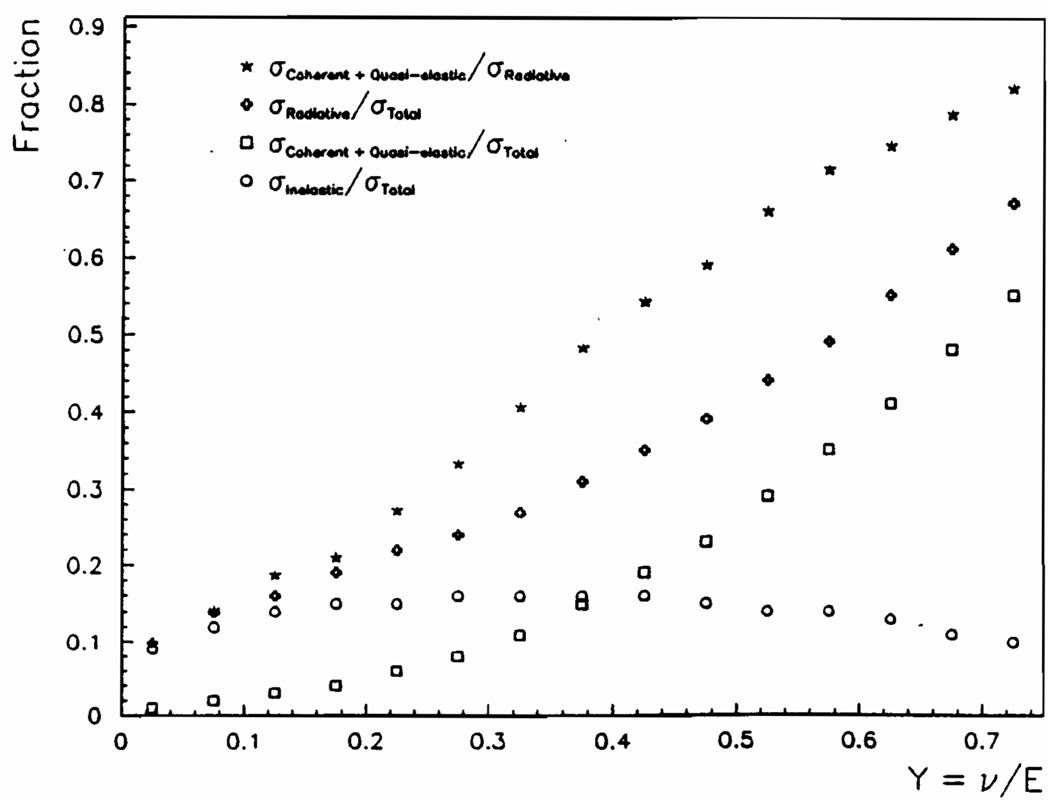

Figure 5.17: Relative contribution of the dominant radiative processes as a function of y for fixed $x_{Bj} = 0.005$.

5.6.1 Radiative Correction Calculations

The calculation of the above radiative processes has been described by several authors [49, 58] and [4], and their results have been applied to muon scattering experiments. These two methods are very similar in their treatment of the coherent, quasi-elastic and inelastic contributions described above, differing mainly in higher order (in α_{em}) calculations and the inclusion of electro-weak interference. In this analysis, a calculation of the radiative processes in xenon and deuterium has been done using a modified program from the EMC group, which employs the method of Mo and Tsai [49, 58]. This method has been compared to the method of Akhundov et al. [4] by Lietzke and Wimpenny [43] with the conclusion that the two methods were nearly the same (to within 1%) for $x_{Bj} < 0.3$, increasing to $\sim$ 4% in the region above $x_{Bj} = 0.8$ and $Q^2 = 200(GeV/c)^2$. The following section describes the input to the radiative correction program and the results of using it to calculate the contribution to the measured cross section on both xenon and deuterium.

Xenon

The largest correction to the data used in this analysis was that due to coherent bremsstrahlung generation in the xenon target. Therefore, the largest source of systematic error in the total correction is due to the lack of knowledge of the xenon elastic form factor.

Form Factor for Elastic Scattering One of the simplest models used to parametrize the charge density of a nucleus is the Two-Parameter Fermi distribution :

$$\rho(r) = \sum_{i=1}^{n} \frac{\rho_0}{(1 + e^{(r-R_i)/\gamma_i})} \qquad (5.3)$$

where the sum is performed over all the nuclear isotopes, R_i is the charge radius, and γ_i is the "skin thickness" of the charge distribution (a measure of the steepness of the slope of the charge distribution at its edge). The elastic form factor is then determined by Fourier transform of this charge distribution. The two parameters, R_i and γ_i have been measured for many elements, however, they have not been measured for xenon. For input to the radiative correction program, these two parameters were obtained by interpolating results from nuclei with atomic numbers close to that of xenon. Specifically, the paramaters have been measured for many isotopes of tin (including Sn_{128} which also occurs in xenon) and Lanthanum (average $A = 138$). The interpolation of the parameters for these two nuclei yields a charge radius value of 5.7 *fermi* and a skin thickness of 0.55 *fermi* for Xe_{131}. These values were used to generate the elastic form factor for xenon and the resulting radiative correction factors compared with the same results obtained with different parameters. For example, a change in the charge radius of 10% resulted in a change in the radiative corrections due to coherent scattering of less than 1%. The variation of the γ had no effect on the results. The total radiative correction results on xenon have been compared to other heavy nuclei, such as lead and copper, showing that the xenon results are consistent with those from other nuclei. This comparison is shown in Figure 5.18.

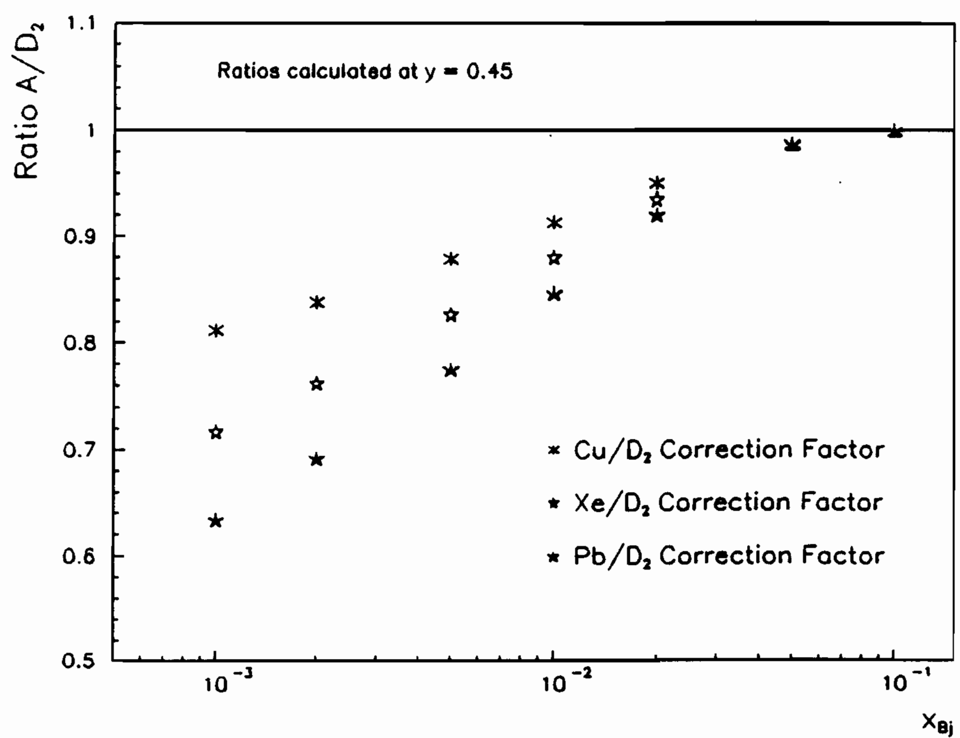

Figure 5.18: Radiative correction factors for Pb, Cu, and Xe presented as ratios of the corrections for the heavy nuclei compared to deuterium.

F_2 Parameterization for Inelastic Scattering The structure function F_2 has not been measured for xenon, and therefore, no specific parametrization exists for input to the radiative correction calculation. However, since the dominant corrections in xenon are due to coherent bremsstrahlung production, the lack of knowledge of F_2 provides a small contribution to the total systematic error. The parametrization used was that of the EMC group [8], who found that by varying F_2 of calcium by a large amount (enough to cancel the EMC Effect at high x_{Bj}) contributed $< .2\%$ to the systematic error on the radiative corrections. Since no previous measurement of F_2 for xenon has been measured, the parametrization of this structure function was taken to be the same as that used by EMC for other heavy nuclei, e.g. Cu, Sn, and Fe.

Corrections to Measured Cross Sections Figure 5.19 shows constant radiative contribution contours for xenon as calculated by the radiative correction program in the Q^2 and x_{Bj} plane defined by the kinematic cuts used in this analysis.

Deuterium

The input parameters to the radiative correction program for deuterium nuclei have been used in previous results and have been undertood regarding any systematic effects related to the measured and calculated parameters. The following sections describe the determination of the systematic error in the deuterium radiative correction calculations.

Form Factor for Elastic Scattering For deuterium, the contribution of elastic scatters accounts for a very small fraction of the total measured cross section. The total radiative correction for deuterium was calculated by Arvidson, et al. [8] using two very different form factors as input. The difference in the total radiative corrections amounted to $< 0.1\%$ for these two methods.

F_2 Parameterization for Inelastic Scattering The parametrization of F_2 for deuterium was found by Arvidson, et al. to contribute a negligible amount to the systematic error on the radiative corrections.

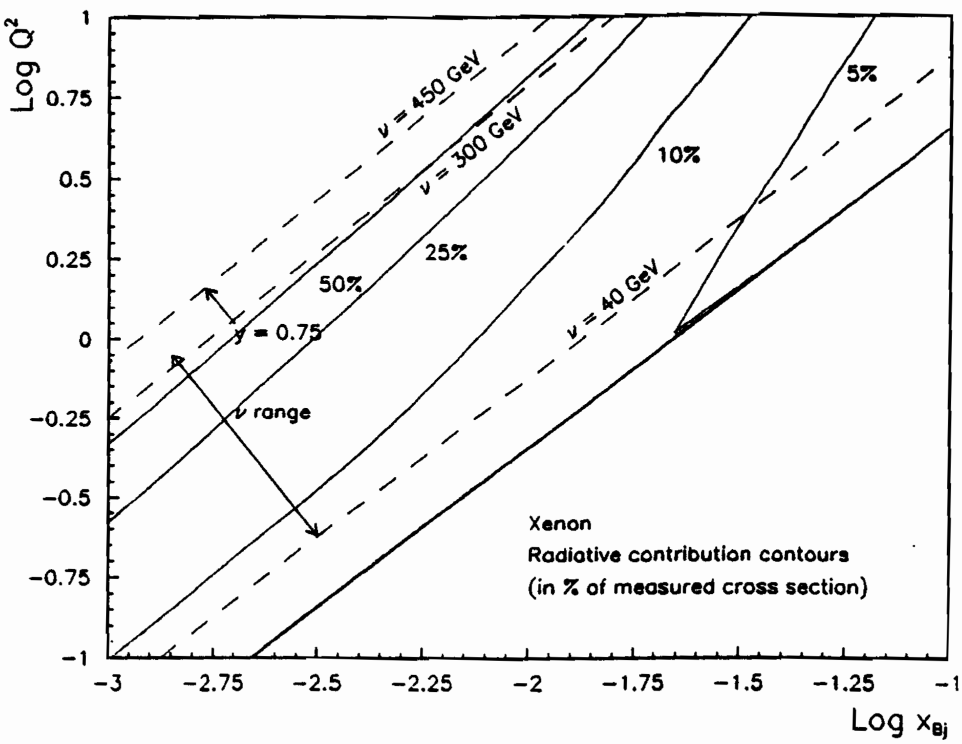

Figure 5.19: Radiative correction factor contours for xenon.

Corrections to Measured Cross Sections Figure 5.20 shows constant radiative contribution contours for deuterium as calculated by the radiative correction program in the Q^2 and x_{Bj} plane defined by the kinematic cuts used in this analysis.

Systematic Error on Radiative Correction Calculations

To correct the cross sections measured in this analysis, the radiative correction program was run to calculate the correction factors on a fine-grained Q^2 and x_{Bj} grid, using the onput as described above. An interpolation routine was used to smooth the correction between grid points, resulting in an almost continuous calculation of the fraction of events at a particular Q^2 and x_{Bj} point that were of radiative origin. Each event was therefore weighted by the fraction of events at a particular Q^2 and x_{Bj} point which were DIS events according to the radiative calculation.

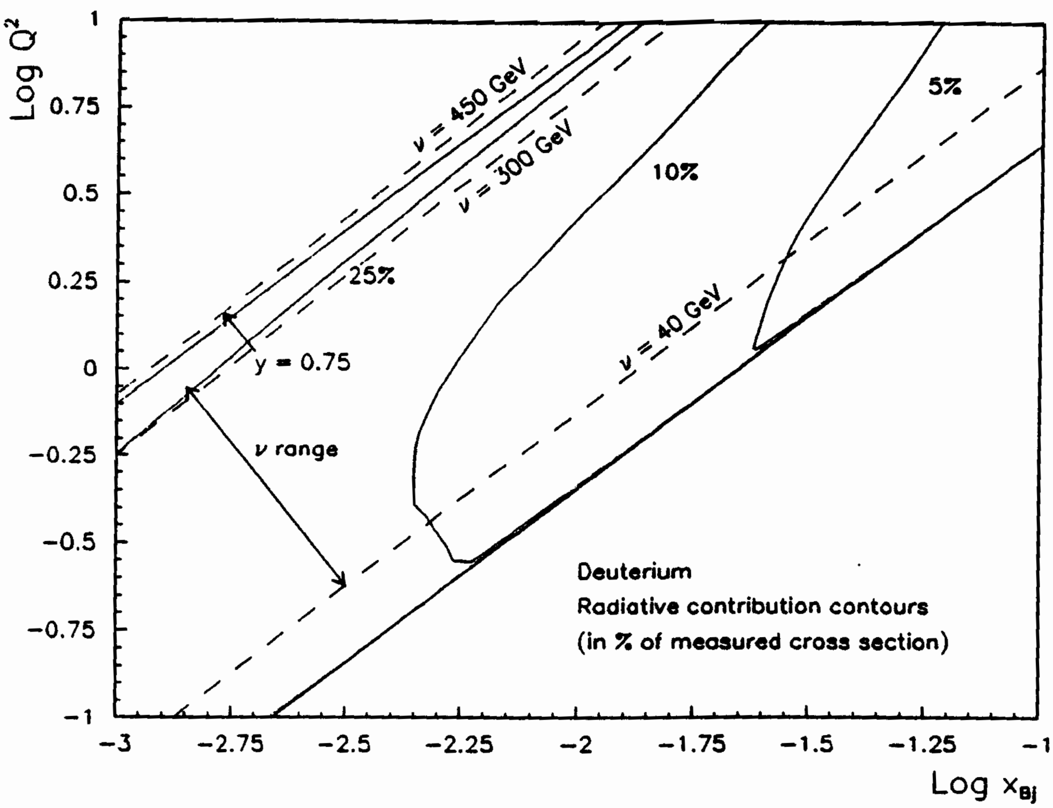

Figure 5.20: Radiative correction factor contours for deuterium.

The source of systematic errors was thus due to the error on the calculation by the correction program due to the uncertainties of the inputs, and to the ratio of radiative to total cross section used to weight the events. For deuterium, both systematic errors were small ($< 1\%$ for the total contribution), but for xenon, since neither F_2 or the charge distribution parameters have been measured, the systematic error could be large. For xenon, the uncertainty in the calculation due to the input parameters appears to be small, even though the charge density parameters have not been measured. Allowing the parameters to vary from the next lowest measured isotope (Sn_{126}) to the next highest measured isotope (La_{138}) yielded a worst case difference in the calculated correction factor of $\sim 1\%$.

5.6.2 Electromagnetic Calorimeter

An alternative way to identify the contribution to the measured cross section from radiative events is to actually detect the events in the data sample. For this analysis, the electromagnetic calorimeter detected and identified photons formed in radiative events; theses events were then discarded from the total sample. In principle, this method identifies photons formed by coherent and quasi-elastic radiative processes. However, even though photons formed in inelastic events can be detected in the calorimeter, these events are hard to eliminate since there are many methods by which energy can be deposited in the calorimeter from the products of inelastic events. If the source of the photon could be identified, i.e. that it came from the beam or scattered muon, then these events could also be corrected in the data sample. For this analysis, however, the intent of the calorimeter analysis was to identify coherent and quasi-elastic radiative events and to cut these from the data sample [54, 55]. Figure 5.21 shows the comparison of radiative correction calculations for the coherent and quasi-elastic contributions to the cross section compared to the Electromagnetic Calorimeter cut for these events.

Note that since the dominant processes for $y > 0.5$ are the coherent and quasi-elastice processes and, therefore, in the high y region, the two methods should yield similar results. The error bars represent statistical errors on the cut ratio to the initial sample.

Calorimeter Cuts for Xenon and Deuterium Data

The calorimeter response was used to discard events based on a fit of energy deposited in the calorimeter divided by ν (the energy available in the event) for muon - nucleus bremsstrahlung candidate events selected from the data. The calorimeter response for the selected events from both the xenon and deuterium data sets were fitted separately in order to check that the response was consistent between the two targets. The result was that both fits agreed to within 4% as shown in Figure 5.22.

The following fitted parametrization was used for both data sets :

$$E_{Cal}/\nu = 0.60 - 0.356 \times 10^{-3}\nu - 0.706 \times 10^{-6}\nu^2 + 0.160 \times 10^{-8}\nu^3 \qquad (5.4)$$

Any event with E_{Cal}/ν greater than this result and in which the calorimeter showed two or less

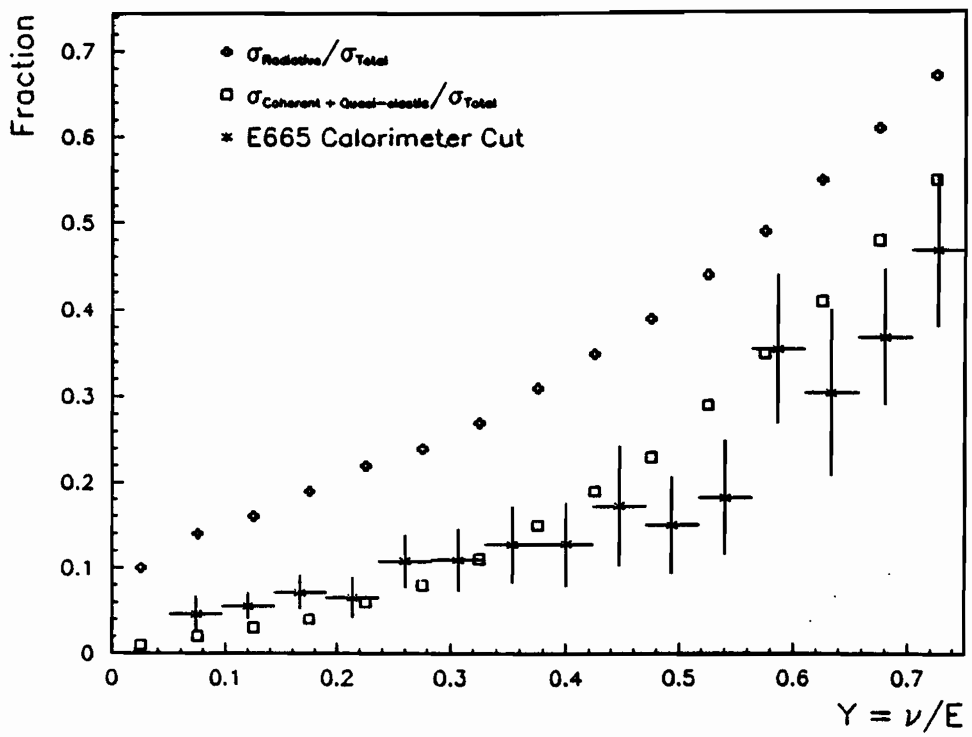

Figure 5.21: Comparison of calculated radiative corrections to the ratio of cut events by the Electromagnetic Calorimeter on the total sample.

clusters of energy, was considered a muon - nucleus bremsstrahlung event and was subsequently cut from the final data sample (the maximum cluster requirement was imposed to reduce the number of DIS events lost due to the low calorimeter energy to ν ratio). The fraction of DIS events lost due to the calorimeter cut can be monitored by counting the number of particle tracks associated with the primary vertex in events that are discarded. Aside from the incident and scattered muon tracks, no other tracks should be associated with the vertex in coherent or quasi-elastic muon - nucleus bremsstrahlung events. Figure 5.23 shows the number of associated tracks at the vertex for events which were cut using the calorimeter.

The DIS loss rate, as determined by this method, was estimated to be $< 2\%$ for both data sets, which may be an overestimate of the loss rate since many of the single fitted track events may be due to electrons from μ - e elastic scattering in the target "leaking" into the x_{Bj} range

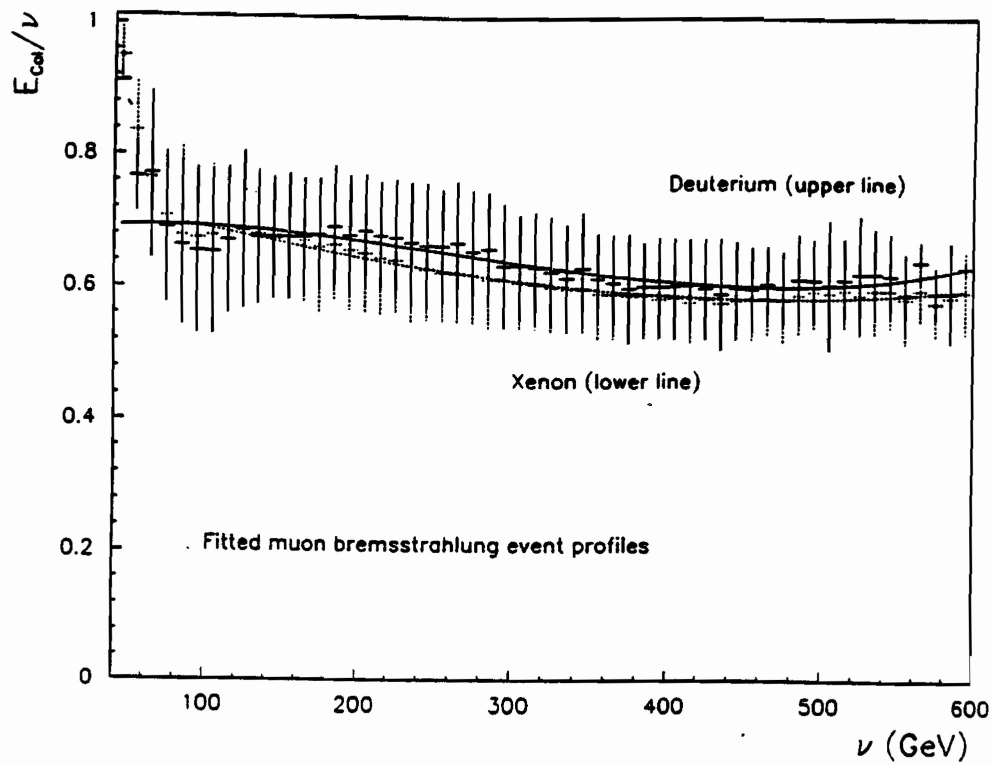

Figure 5.22: Calorimeter response to muon bremsstrahlung events, comparing the fitted results for xenon to deuterium.

defined by the kinematic cuts (see Section 4.4).

Systematic Error on Calorimeter Cuts

An estimate of the systematic error associated with the use of the electromagnetic calorimeter is difficult to determine without a very detailed Monte Carlo calculation including a full simulation of the calorimeter response. The method used in this analysis, that of fitting muon - nucleus bremsstrahlung events in order to measure the response of the calorimeter, was done to determine if the response was altered as a function of time. If the response had been significantly different for the two running periods, a cross calibration would have had to be done relating the two response functions. As it was, the calorimeter response was the same to within 5% using the results of the fit.

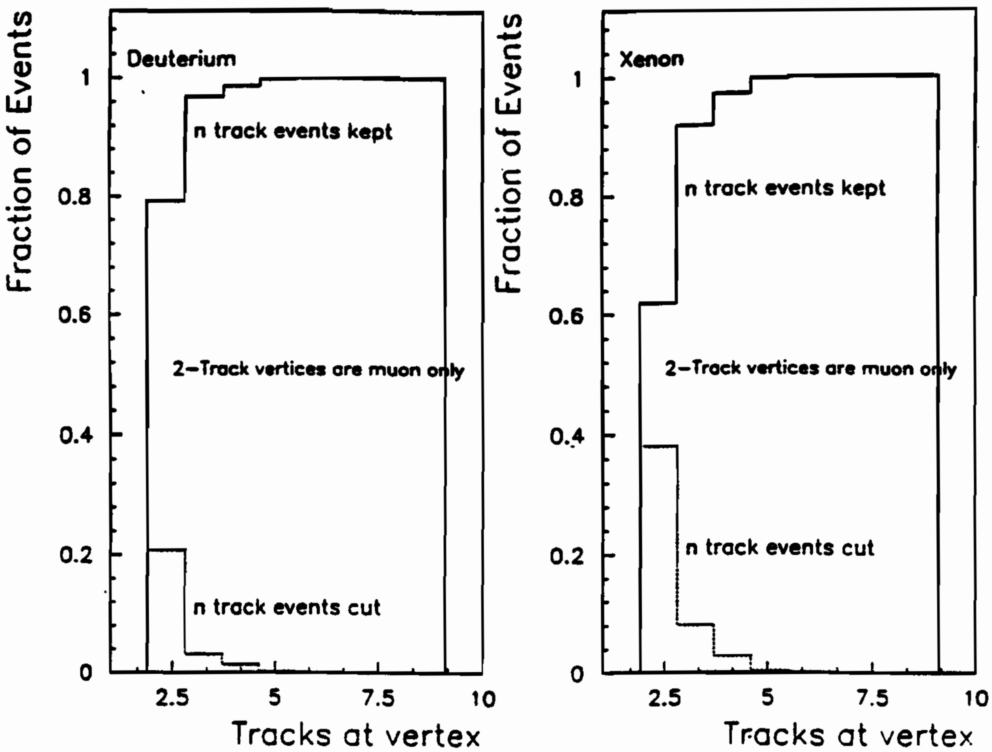

Figure 5.23: Estimate of DIS losses due to the calorimeter cut.

5.7 Non-Isoscalar Target Correction for Xenon

In principle, when measuring the cross section per nucleon, the difference in the scattering cross section from neutrons and protons will affect the results. It is, therefore, advantageous when comparing several nuclei to use only nuclei which are isoscalar. In this analysis, a comparison is made between a non-isoscalar nucleus, xenon, and an isoscalar nucleus, deuterium. Therefore, the cross section per nucleon for xenon should be corrected for this difference, if there is any. Figure 5.24 shows the ratio of neutron/proton structure functions as a function of x_{Bj} [12].

Note that at low x_{Bj}, the ratio of σ_n/σ_p is consistent with 1.0, indicating that the neutron and proton appear as similar objects (this is expected since at low x_{Bj}, the virtual photons are absorbed by sea quarks). A parameterization of these results yields :

$$F_2{}^n(x)/F_2{}^p(x) = 1 - 1.85x + 2.45x^2 - 2.35x^3 + x^4 \ (\pm .015) \tag{5.5}$$

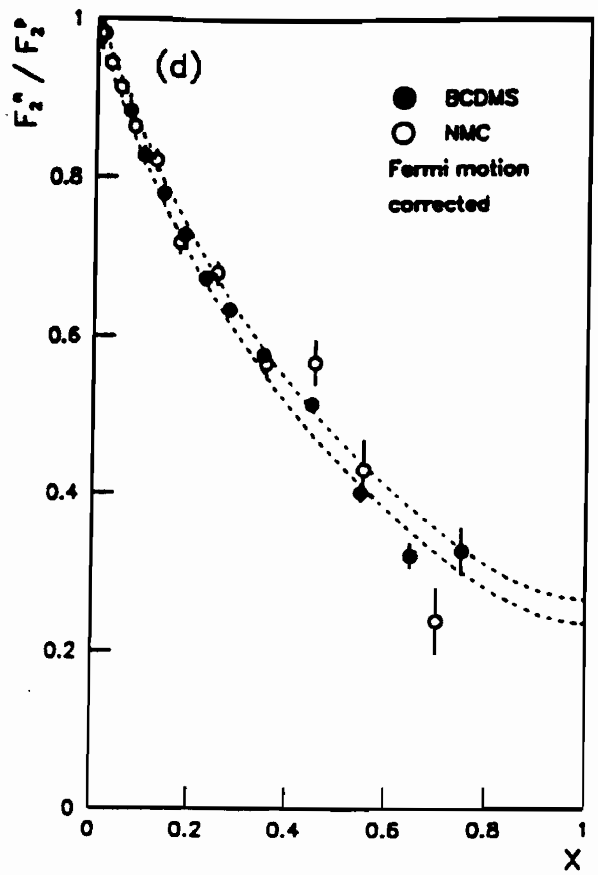

Figure 5.24: $F_2{}^n/F_2{}^p$ versus x_{Bj}.

The correction factor for the xenon data in each x_{Bj} bin is calculated according to :

$$C(x) = \frac{A_{Xe}[1 + F_2{}^n(x)/F_2{}^p(x)]}{2[Z_{Xe} + N_{Xe}F_2{}^n(x)/F_2{}^p(x)]} \tag{5.6}$$

and is shown in Table 5.2.

5.7.1 Systematic Error on Non-Isoscalar Correction

From Table 5.2, the systematic error introduced by the correction applied to the xenon cross section was 0.3%.

5.8 Summary of Systematic Errors

The systematic error estimates obtained after making the corrections described in this section are summarized in Table 5.3. The total contribution is given for both radiative correction results and for calorimeter cut results (in parentheses).

TABLE X: NON-ISOSCALAR CORRECTION FOR XENON

x_{Bj}	$C(x)$	$\sigma_{C(x)}$
.0013	1.0002	.0030
.0021	1.0003	.0030
.0035	1.0006	.0030
.0060	1.0010	.0030
.0098	1.0016	.0030
.016	1.0026	.0030
.027	1.0044	.0030
.045	1.0073	.0030
.074	1.0119	.0030
.126	1.0200	.0031

TABLE XI: SUMMARY OF SYSTEMATIC ERRORS

Source	Estimate on Ratio
Beam Normalization	0.7%
Non-Isoscalar Target	0.3%
Target Density	0.4%
Trigger Acceptance	1.05%
Empty Target Subtraction	1.4%
Muon Reconstruction Efficiency	7.0%
Radiative Processes	
Radiative Corrections	1.4%
Calorimeter Cut	5.0%
Total	7.4% (8.8% with Calorimeter Cut)

6. XENON/DEUTERIUM CROSS SECTION RATIOS

In this section, the results of the ratios of cross sections will be shown starting from uncorrected, normalized event yield ratios and ending with the final, fully corrected ratios determined by 3 independent methods. The x_{Bj}, Q^2, and ν dependence of the uncorrected ratios show the same trends as in the corrected ratios. A comparison of the 3 different methods used to eliminate background due to radiative processes is made as follows :

1. More restrictive kinematic cuts were applied to reduce the fraction of radiative events in the sample.
2. Radiative corrections were calculated according to the method of Mo and Tsai (see Section 5.6).
3. Events were cut using the total amount of energy detected in the electromagnetic calorimeter.

The agreement between the 3 methods indicates the amount of systematic error introduced by the radiative correction procedures.

6.1 Raw Event Yields

The uncorrected event yields from the xenon and deuterium targets are presented in Figure 6.1 as a function of x_{Bj}; only the "standard" kinematic cuts (as defined in Section 4.4) are applied. There are $\sim$ 10000 events passing these kinematic cuts from each target.

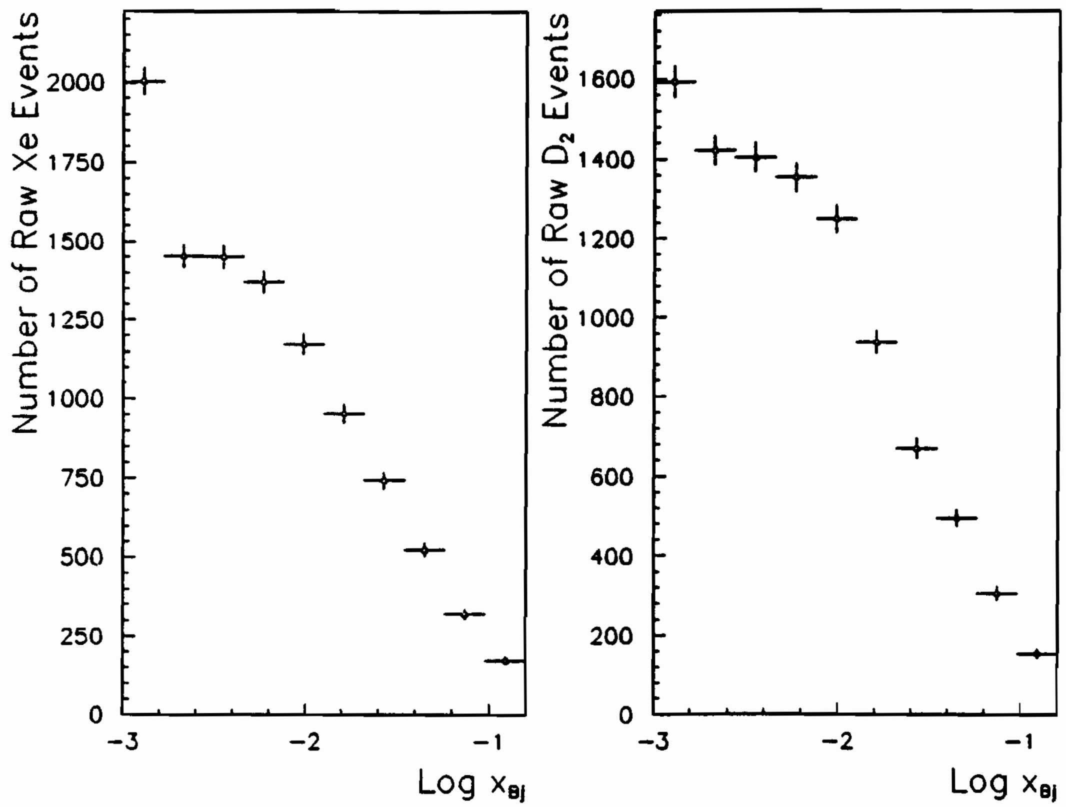

Figure 6.1: Raw event yields from xenon and deuterium shown as a function of log x_{Bj}.

Figure 6.2 shows the raw distributions as a function of Q^2, splitting the data into two x_{Bj} regions; the choice of the two x_{Bj} regions was made to divide the data into shadowed and un-shadowed regions (which will become apparent in Section 6.3).

Figure 6.3 shows the raw distributions as a function of ν in the range $40\ GeV < \nu < 300\ GeV$; the upper limit was determined by restricting the total radiative correction to be $\leq 50\%$ in any ν bin for xenon.

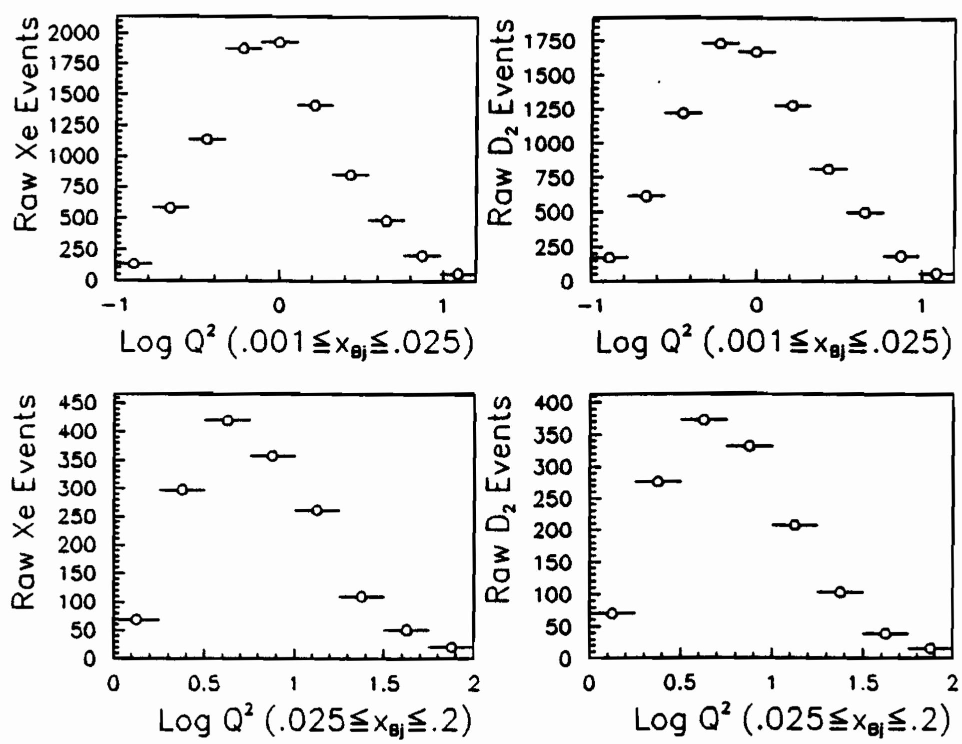

Figure 6.2: Raw event yields from xenon and deuterium shown as a function of log Q^2. The x_{Bj} range has been divided into two regions for this plot.

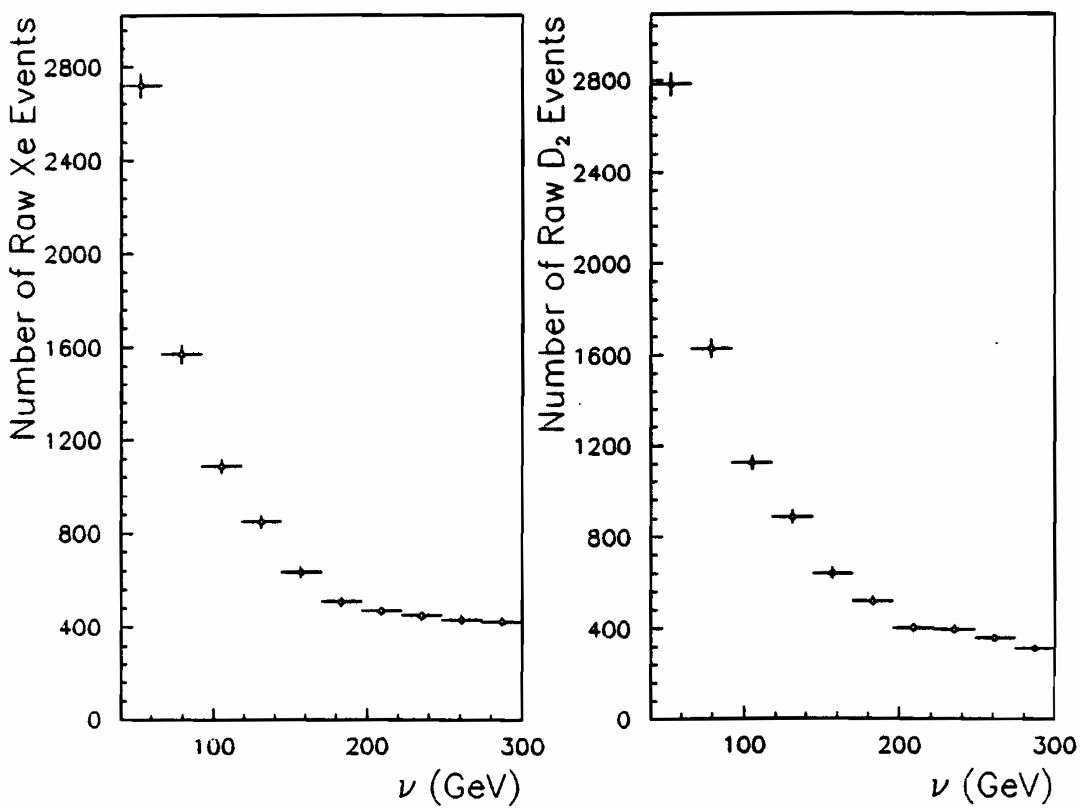

Figure 6.3: Raw event yields from xenon and deuterium as a function of ν.

6.2 Uncorrected Cross Section Ratios

In this section, the uncorrected event yields will be normalized by the luminosity observed in each target to obtain uncorrected cross section ratios. The following table shows the parameters used and the measured luminosity for the xenon and deuterium targets.

TABLE XII: TARGET LUMINOSITY

Target	N_{beams} ($\times 10^{10}$)	ρ_{target} (g/cm^3)	l_{target} (cm)	Luminosity $\rho l N_A N_{beams}$ ($\times 10^{34}$ cm^{-2})
Xenon	0.9348	0.0851	113	5.4134
Deuterium	0.4355	0.1630	115	4.9160

Figure 6.4 shows the uncorrected Xe/D_2 cross section ratio as a function of x_{Bj} for all ν and Q^2.

Figure 6.5 shows the uncorrected Xe/D_2 cross section ratio as a function of Q^2 for the two x_{Bj} regions.

Figure 6.6 shows the uncorrected Xe/D_2 cross section ratio as a function of ν for all x_{Bj} and Q^2.

The uncorrected ratio as a function of x_{Bj} and ν shows a tendency towards increased depletion at low x_{Bj} and high ν and the amount of depletion showing a slight Q^2 dependence.

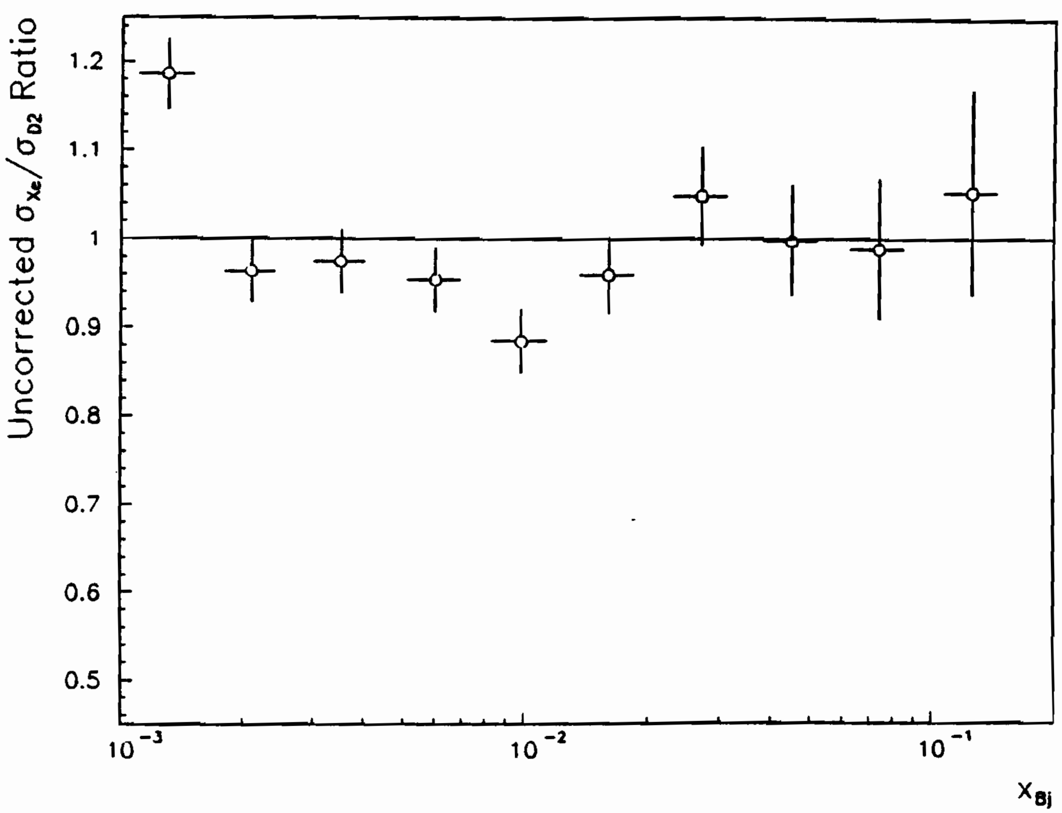

Figure 6.4: Uncorrected Xe/D_2 cross section ratio as a function of x_{Bj}.

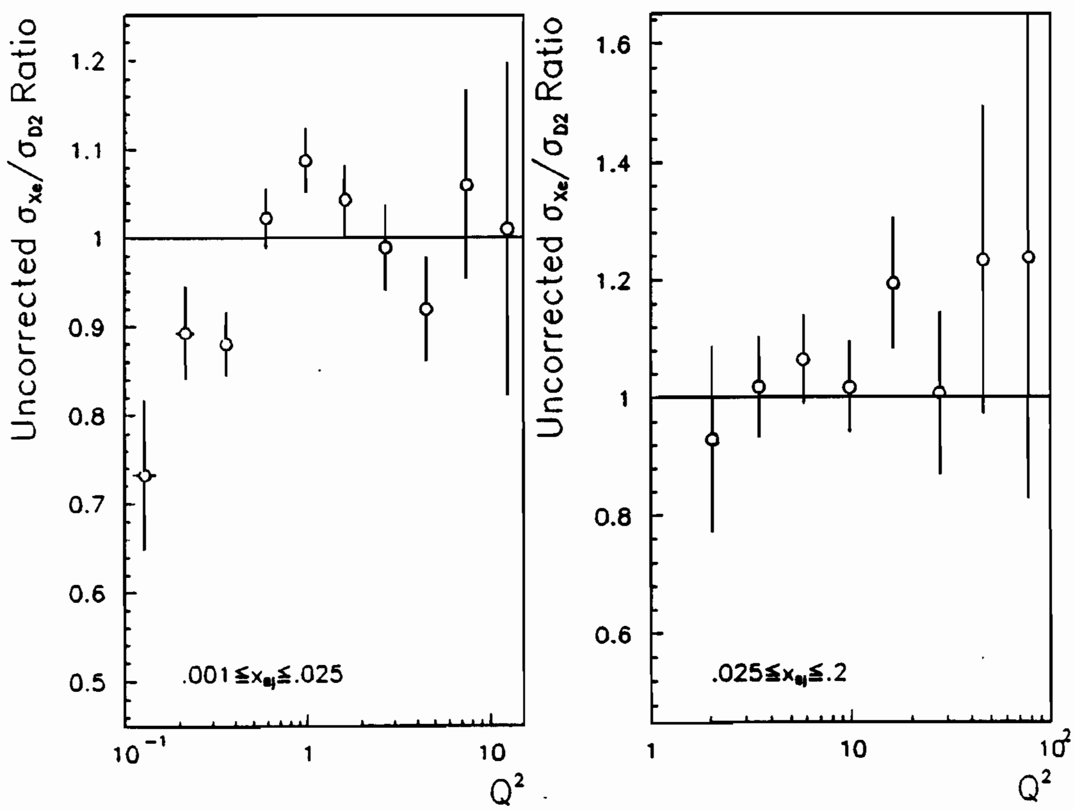

Figure 6.5: Uncorrected Xe/D_2 cross section ratio as a function of Q^2 for the two indicated x_{Bj} regions.

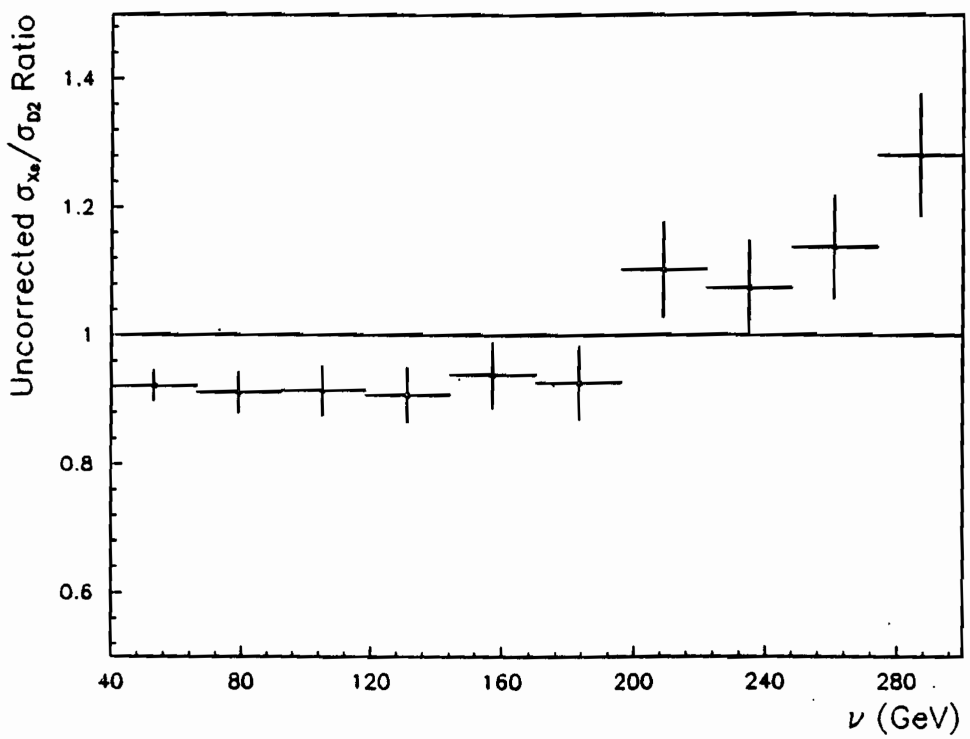

Figure 6.6: Uncorrected Xe/D_2 cross section ratio as a function of ν.

6.3 Corrected Cross Section Ratios

In this section, cross section ratios will be shown which include the full complement of correction factors applied to the data as discussed in Chapter 5. All of the ratios are corrected for empty target events, reconstruction efficiency (in the deuterium data), and trigger acceptance. In addition, each of the 3 methods described in Section 6.1 will contain the correction or cut used to eliminate the contribution from radiative processes. Figure 6.7 shows the corrections for muon reconstruction efficiency and trigger acceptance applied to deuterium (solid line) and xenon (dotted line) as a function of x_{Bj}.

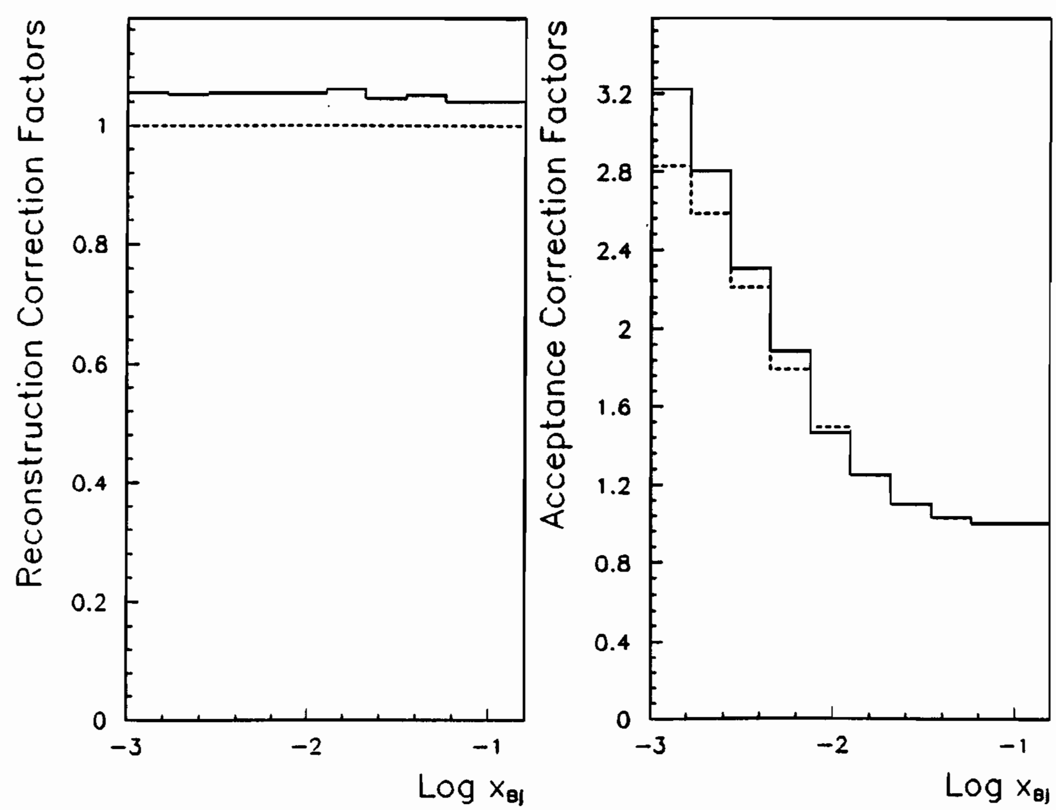

Figure 6.7: Reconstruction efficiency and acceptance correction factors for deuterium (solid line) and xenon (dotted line) as a function of x_{Bj}.

Note that there is no muon reconstruction efficiency correction factor (= 1.0) for xenon (see Section 5.4). Figure 6.8 shows the xenon/deuterium ratio of these correction factors as a function of x_{Bj}.

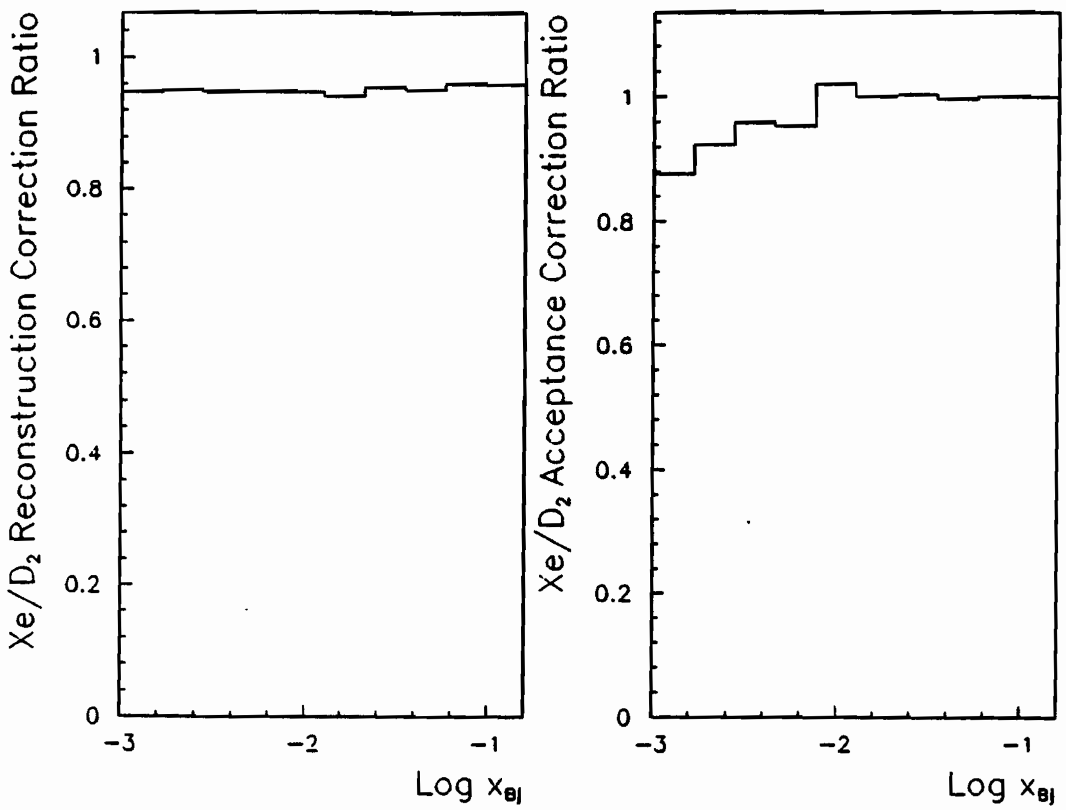

Figure 6.8: Xe/D_2 ratio of muon reconstruction efficiency and trigger acceptance corrections as a function of x_{Bj}.

6.3.1 Kinematic Cut Results

The first method used to reduce the amount of radiative events present in the final sample is to redefine the kinematic region used to select DIS events. In a plot of Q^2 versus ν, the radiative contributions are present at low Q^2 and high ν (see Figure 4.9). By redefining certain kinematic cuts, it can be seen that the majority of the radiative events can be removed from the sample without sacrificing all of the data. The following kinematic cuts are used to calculate ratios :

- $Q^2 > 0.2\ (GeV/c)^2$
- $x_{Bj} > 0.002$
- $\nu > 40\ GeV$
- $y = \nu/E < 0.5$

Figure 6.9 shows the corrected cross section ratio versus x_{Bj} with these kinematic cuts and with all corrections except radiative applied.

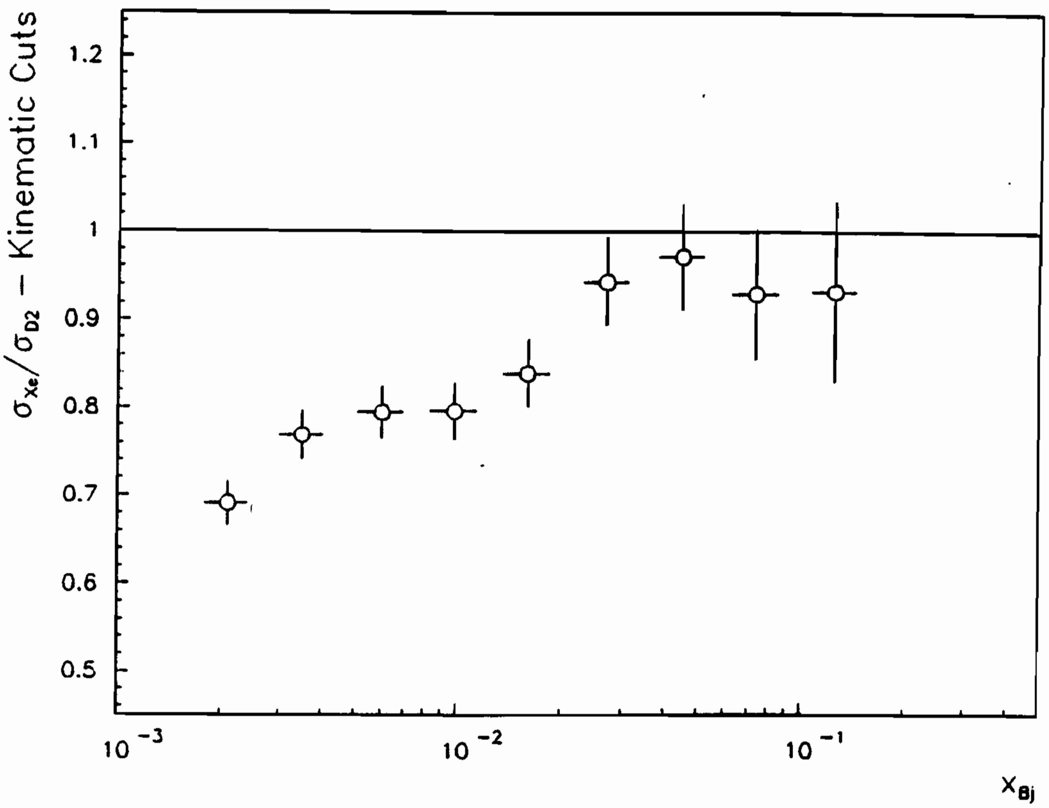

Figure 6.9: Corrected cross section ratio as a function of x_{Bj} evaluated with redefined kinematic cuts.

Figure 6.10 shows the cross section ratio versus Q^2 in two x_{Bj} regions with the same corrections and kinematic cuts applied.

Figure 6.11 shows the corrected cross section ratio versus ν with the same cuts and corrections.

The cross section ratio again shows shadowing in the low x_{Bj} and high ν regions and is consistent with little or no Q^2 dependence.

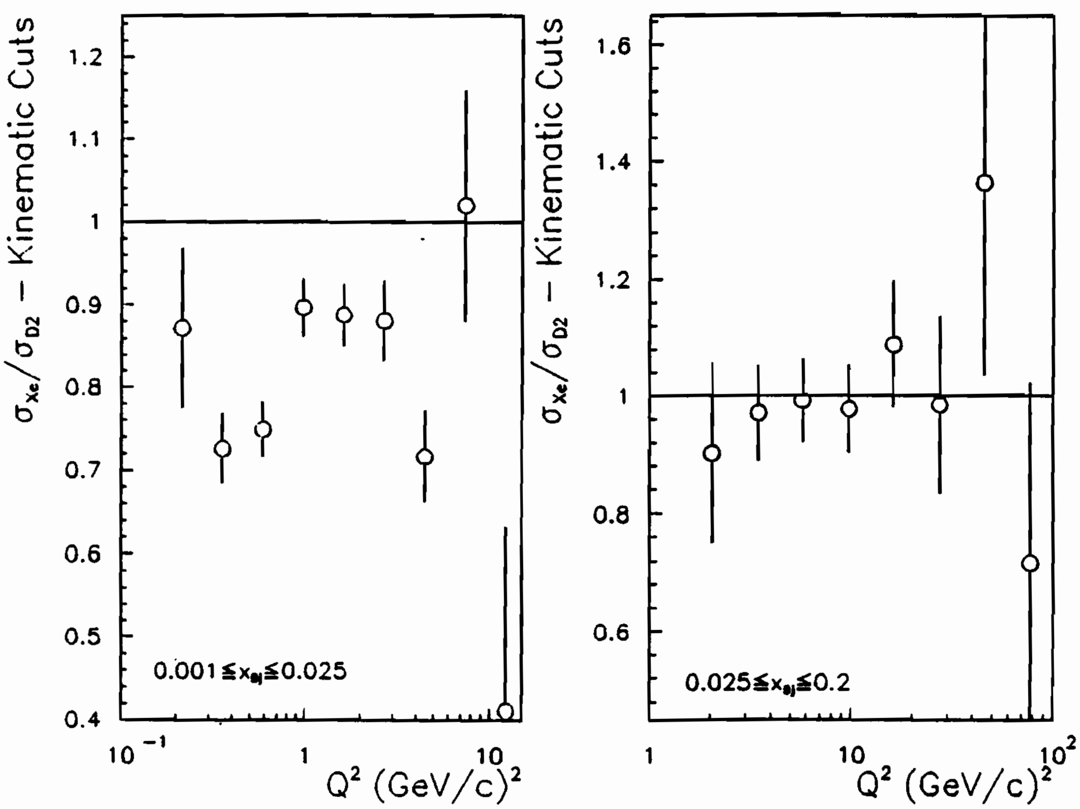

Figure 6.10: Corrected cross section ratio as a function of Q^2 evaluated with redefined kinematic cuts.

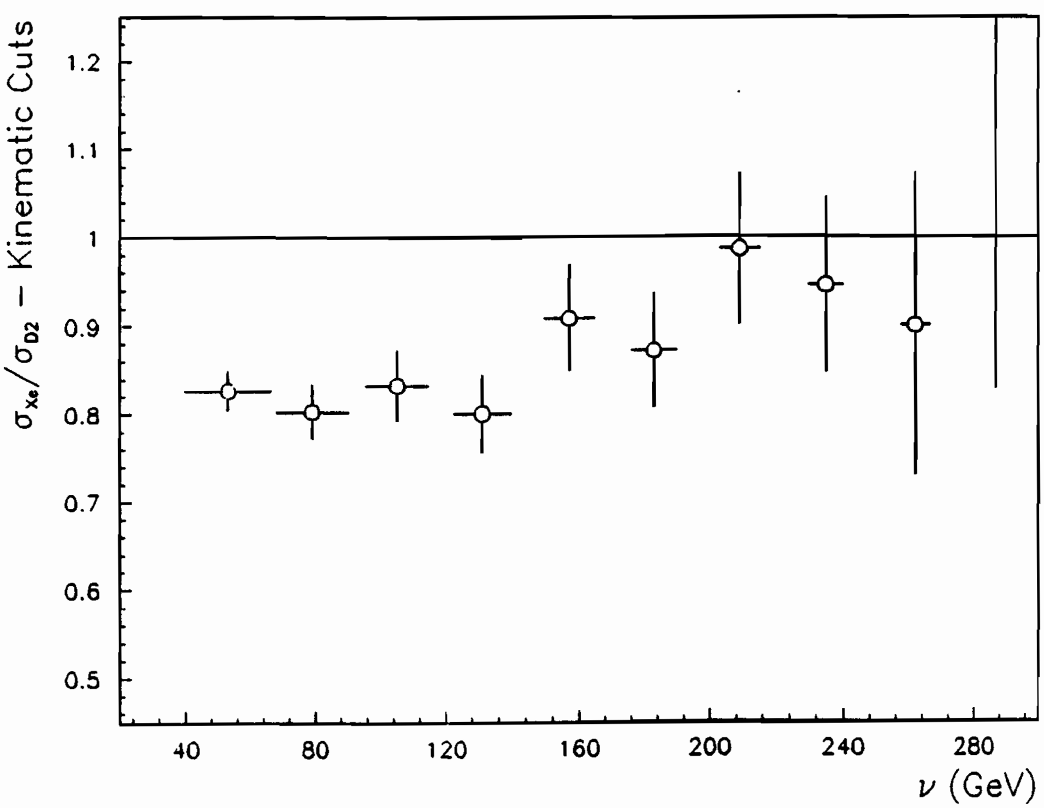

Figure 6.11: Corrected cross section ratio as a function of ν evaluated with redefined kinematic cuts.

6.3.2 Radiative Correction Results

In this section, the "standard" kinematic cuts will return and the presence of radiative background will be treated by applying the calculated radiative corrections (see Section 5.6).

Figure 6.12 shows the radiative correction factors calculated for deuterium (solid line) and xenon (dotted line) as a function of x_{Bj}.

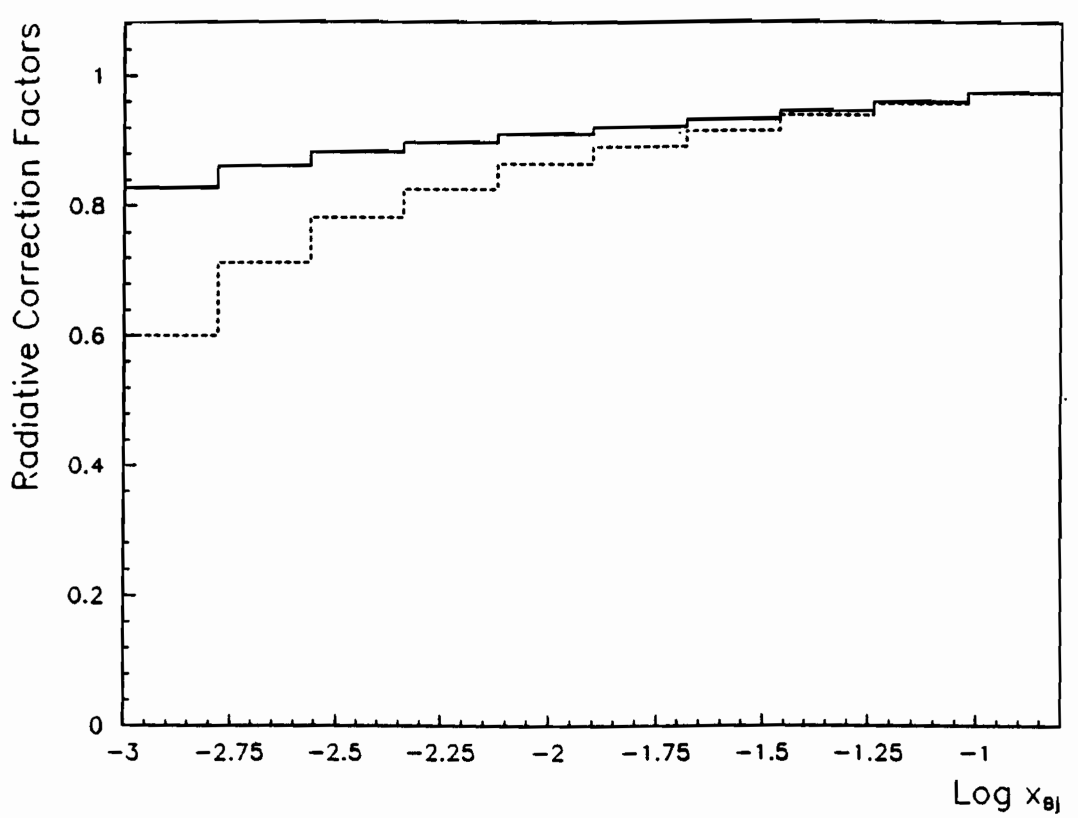

Figure 6.12: Radiative correction factors for deuterium and xenon as a function of log xBj.

The maximum radiative contribution of $\sim 40\%$ in the lowest x_{Bj} bin was determined by the choice of the maximum $y = \nu/E = 0.75$ defined in the "standard" kinematic cuts (see Section 4.4). Figure 6.13 shows the xenon/deuterium ratio of these correction factors as a function of x_{Bj}.

Figure 6.14 shows the corrected cross section ratio versus x_{Bj} with the "standard" kinematic cuts and all corrections (including radiative corrections) applied.

Figure 6.15 shows the cross section ratio versus Q^2 in two x_{Bj} regions with the same

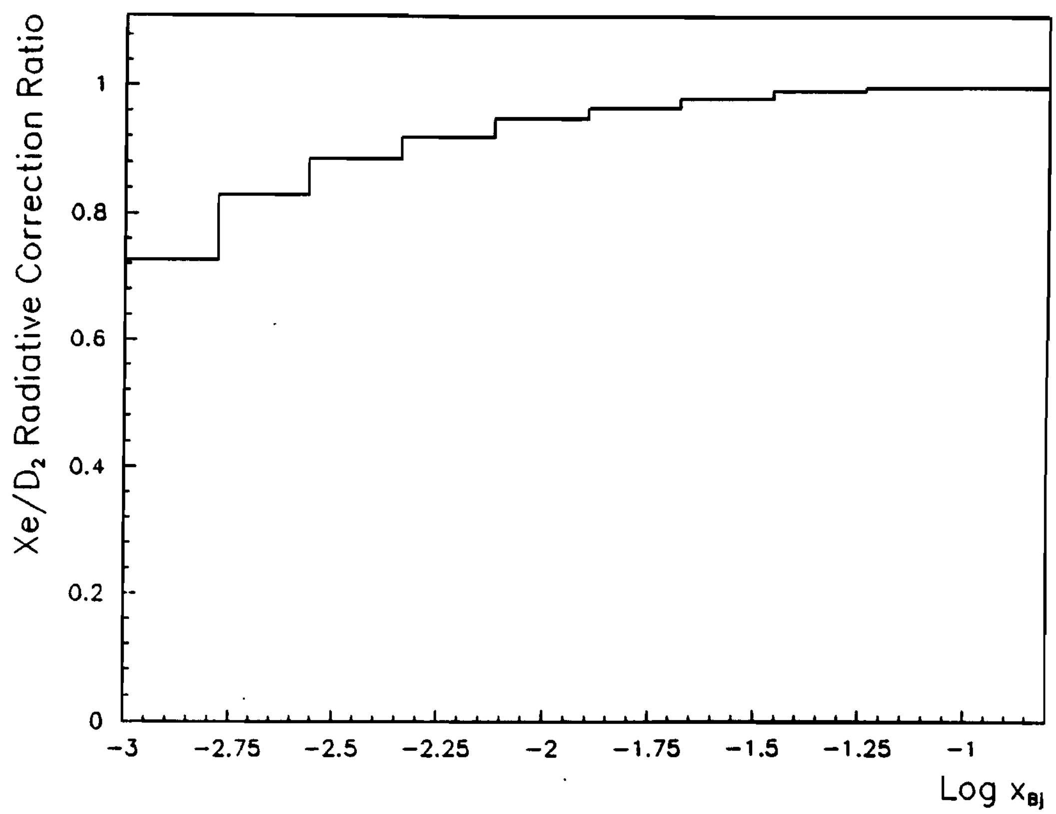

Figure 6.13: Xe/D_2 ratio of radiative correction factors as a function of x_{Bj}.

corrections and kinematic cuts applied.

Figure 6.16 shows the corrected cross section ratio versus ν with the same cuts and corrections.

The presence of shadowing is clearly indicated in the cross section ratio in the low x_{Bj} region and in the entire ν range with no increase in the lowest x_{Bj} and high ν bins, and are consistent with a flat Q^2 dependence.

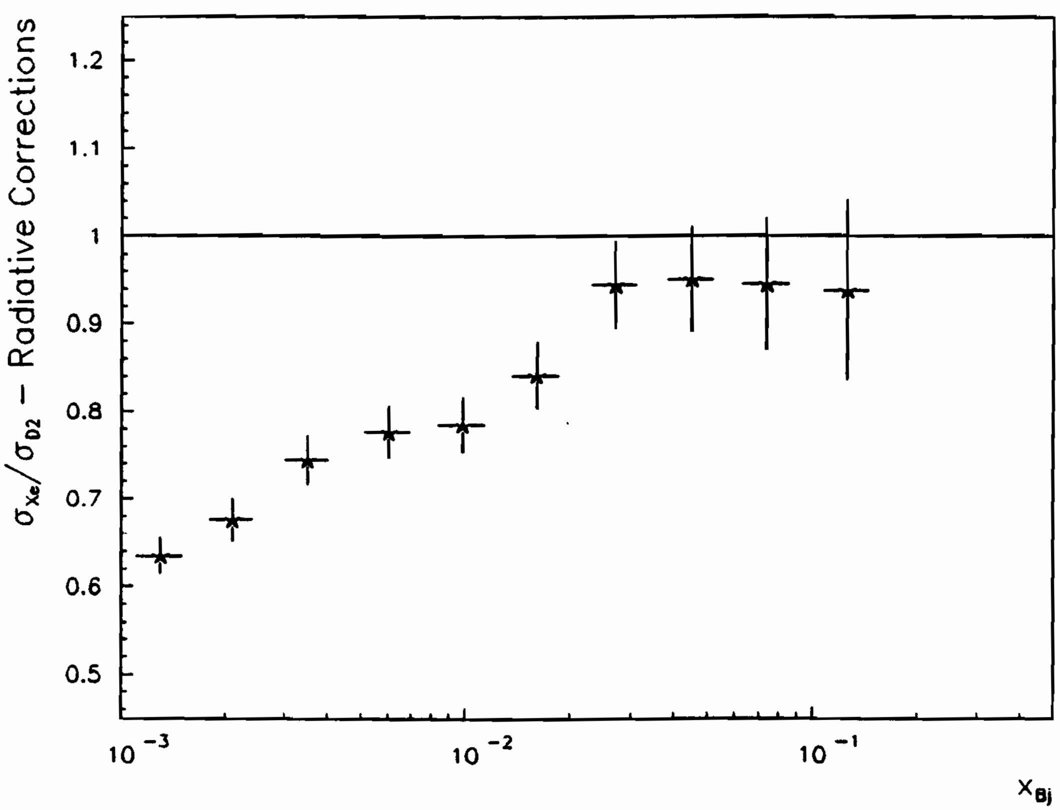

Figure 6.14: Corrected cross section ratio as a function of x_{Bj} evaluated including radiative corrections.

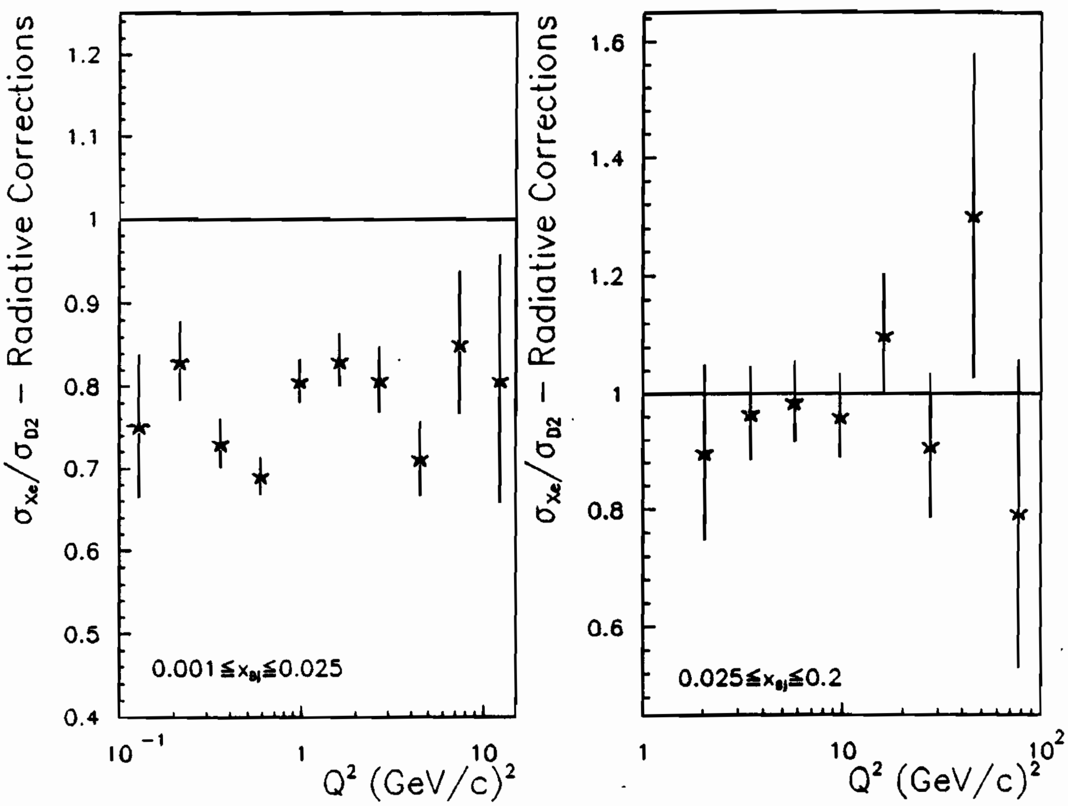

Figure 6.15: Corrected cross section ratio as a function of Q^2 evaluated including radiative corrections.

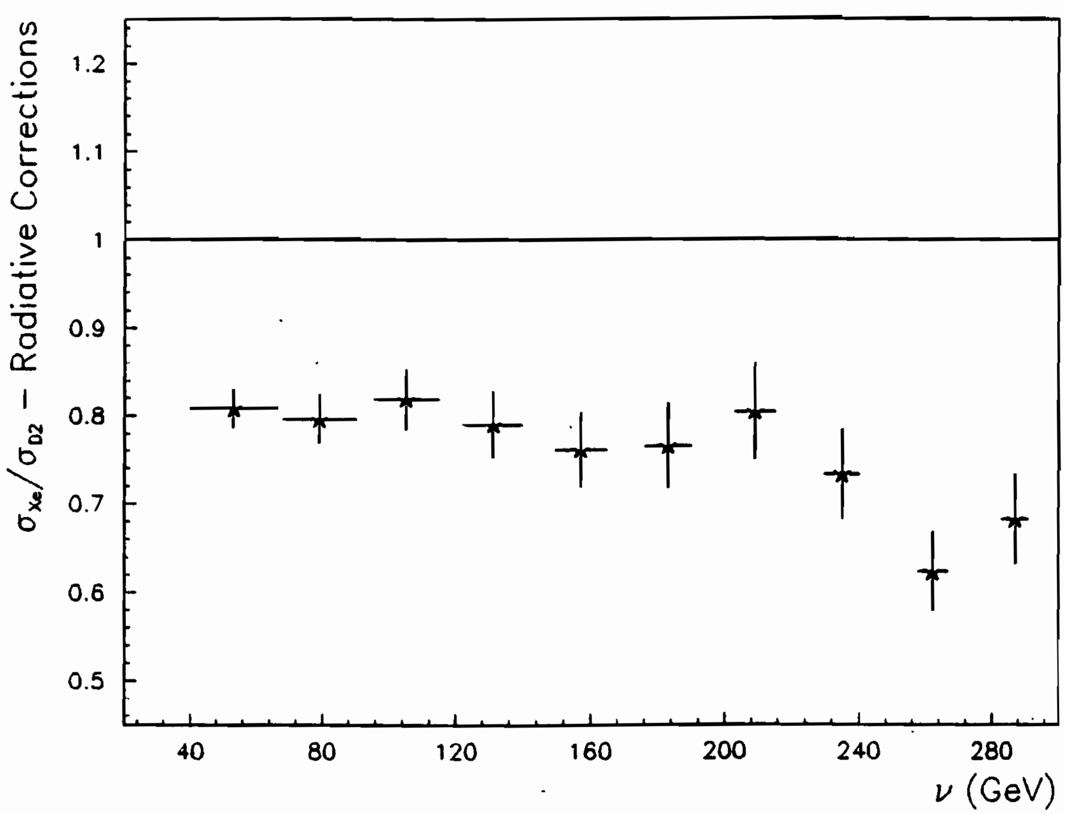

Figure 6.16: Corrected cross section ratio as a function of ν evaluated including Radiative Corrections.

6.3.3 Calorimeter Cut Results

The final section for reporting the fully corrected cross section ratios will use the electromagnetic calorimeter to cut those events which are determined to be radiative in nature. As described in Section 5.6, the calorimeter was used to selectively cut events in which a large fraction of the available energy was seen only in the calorimeter, indicating the presence of a high energy photon resulting from a coherent or quasi-elastic μ - nucleus scattering interaction.

Figure 6.17 shows the ratio of events remaining after the electromagnetic calorimeter cut to the raw sample for deuterium (solid line) and xenon (dotted line) as a function of x_{Bj}.

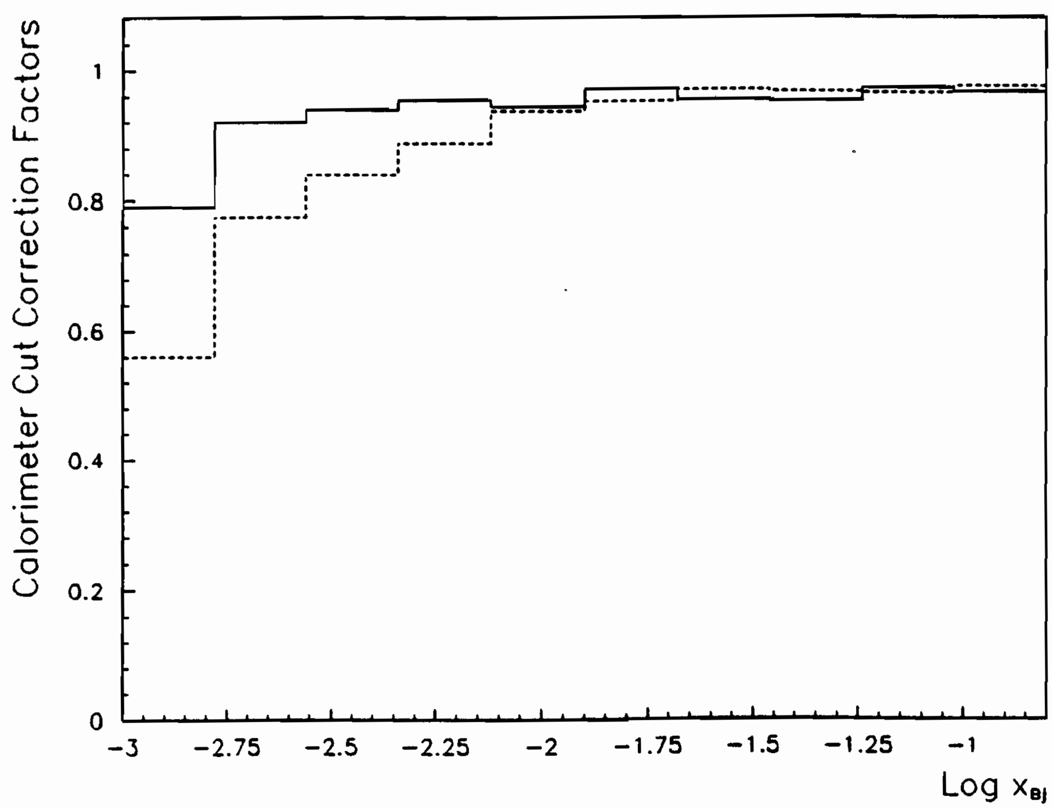

Figure 6.17: Effect of the Electromagnetic Calorimeter cut for xenon and deuterium as a function of log xBj.

Figure 6.18 shows the xenon/deuterium ratio of these cuts as a function of x_{Bj}. The error bars represent the statistical error on the ratio of cut events to raw events.

Overlayed on this plot is the ratio of radiative corrections (dotted line) from Figure 6.13.

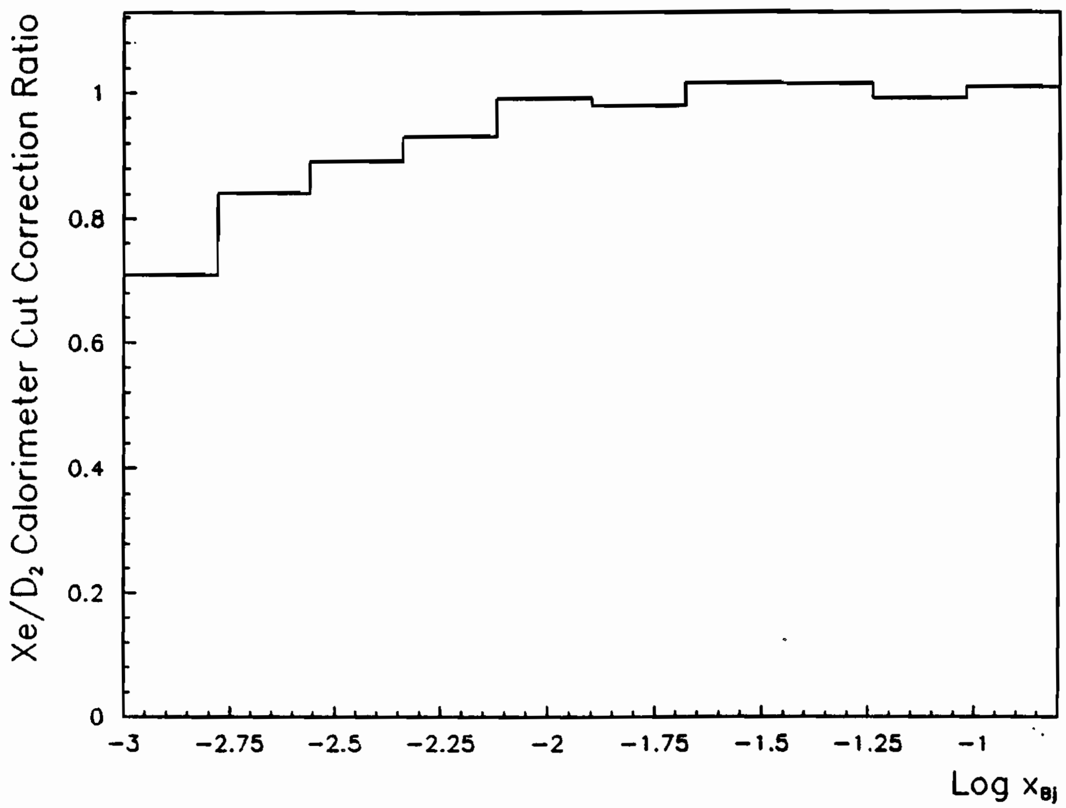

Figure 6.18: Xe/D_2 ratio of the Electromagnetic Calorimeter cut as a function of log x_{Bj}.

The two curves show no difference within the statistical precision of the calorimeter correction result.

Figure 6.19 shows the corrected cross section ratio versus x_{Bj} with the "standard" kinematic cuts and all corrections (after the electromagnetic calorimeter cut) applied.

Figure 6.20 shows the cross section ratio versus Q^2 in two x_{Bj} regions with the same calorimeter cut and kinematic cuts applied.

Figure 6.21 shows the corrected cross section ratio versus ν with the same kinematic and calorimeter cuts applied.

The cross section ratio again shows shadowing in the low x_{Bj} region and in the entire ν range and shows the same Q^2 dependence seen in the ratios with radiative corrections applied.

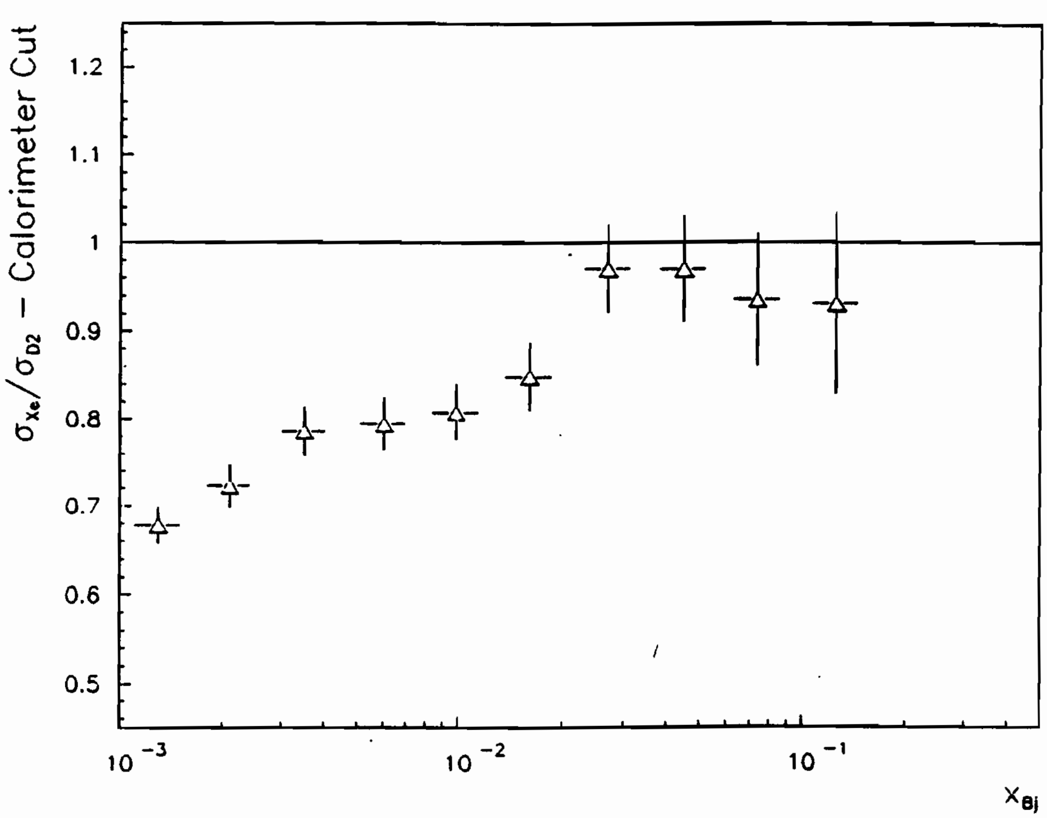

Figure 6.19: Corrected cross section ratio as a function of x_{Bj} evaluated including the Electromagnetic Calorimeter cut.

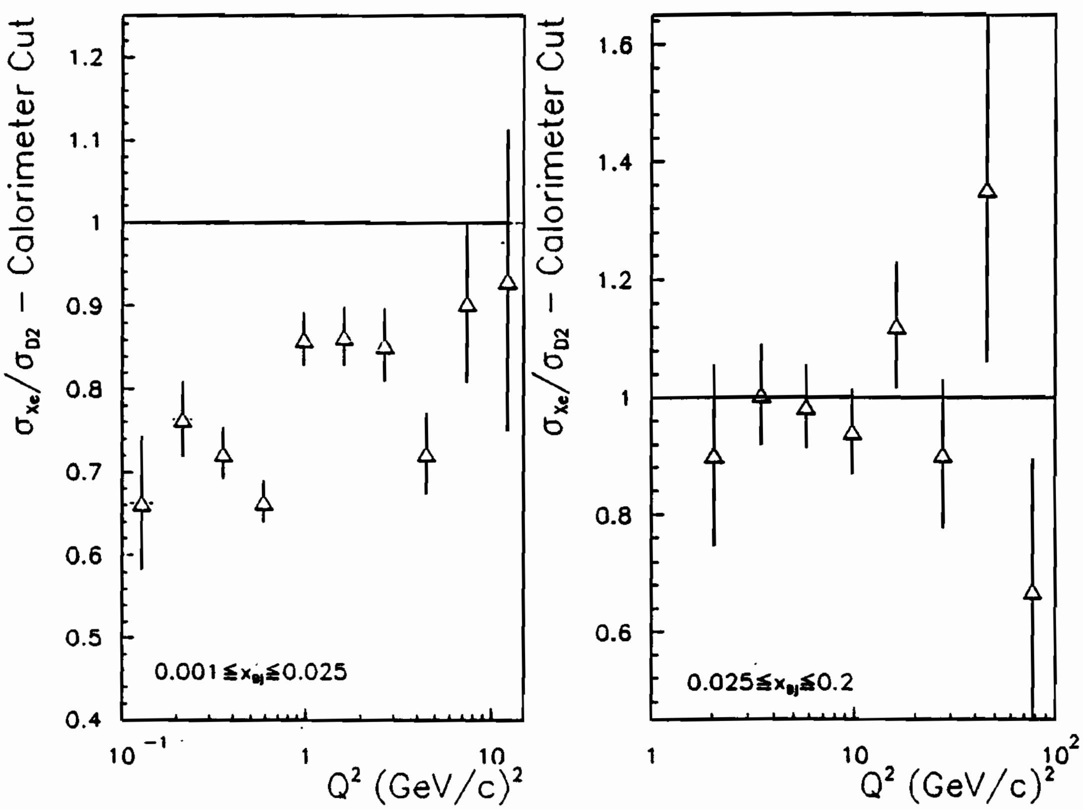

Figure 6.20: Corrected cross section ratio as a function of Q^2 evaluated including the Electromagnetic Calorimeter cut.

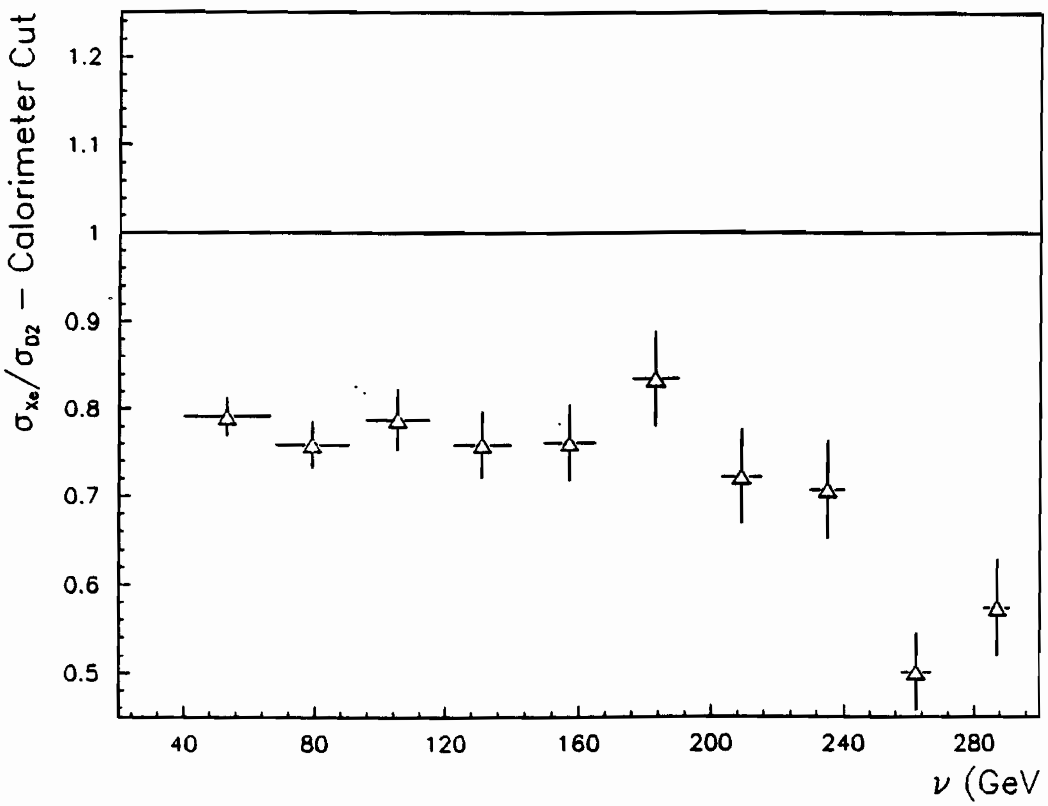

Figure 6.21: Corrected cross section ratio as a function of ν evaluated including the Electromagnetic Calorimeter cut.

6.4 Comparison of Correction Methods

The 3 different methods used to correct for the presence of the radiative background in the data sample are compared in overlapping regions of the kinematic variables. Figure 6.22 shows the results of the 3 methods plotted as a function of x_{Bj}.

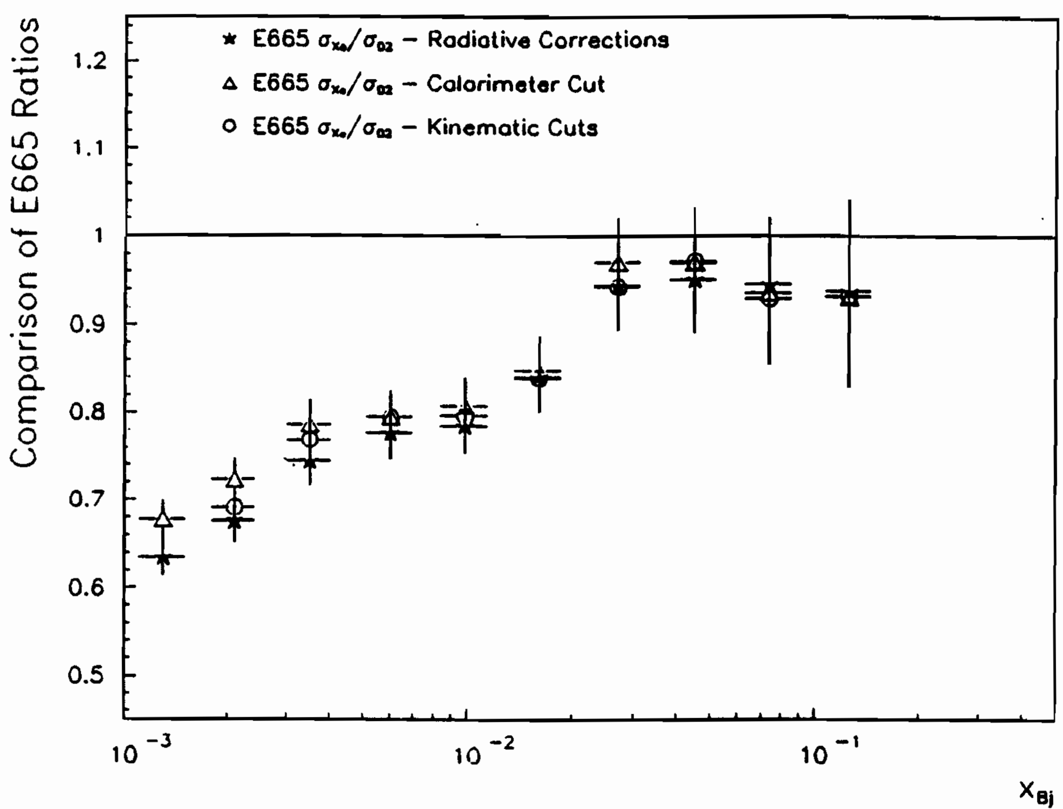

Figure 6.22: Comparison of cross section ratios for the 3 methods indicated as a function ofx_{Bj}.

Figure 6.23 shows the comparison of the cross section ratios for the 3 methods as a function of Q^2 in the two x_{Bj} regions.

Figure 6.24 shows the results of the 3 methods plotted as a function of ν.

Within the measured statistical errors, all 3 methods agree in the overlap region with the redefined kinematic cut results. The results using calculated radiative corrections and the calorimeter cut agree over the total range within statistical errors. It can be seen, however, that there is a systematic increase of the ratio for the calorimeter cut ratio over the radiative

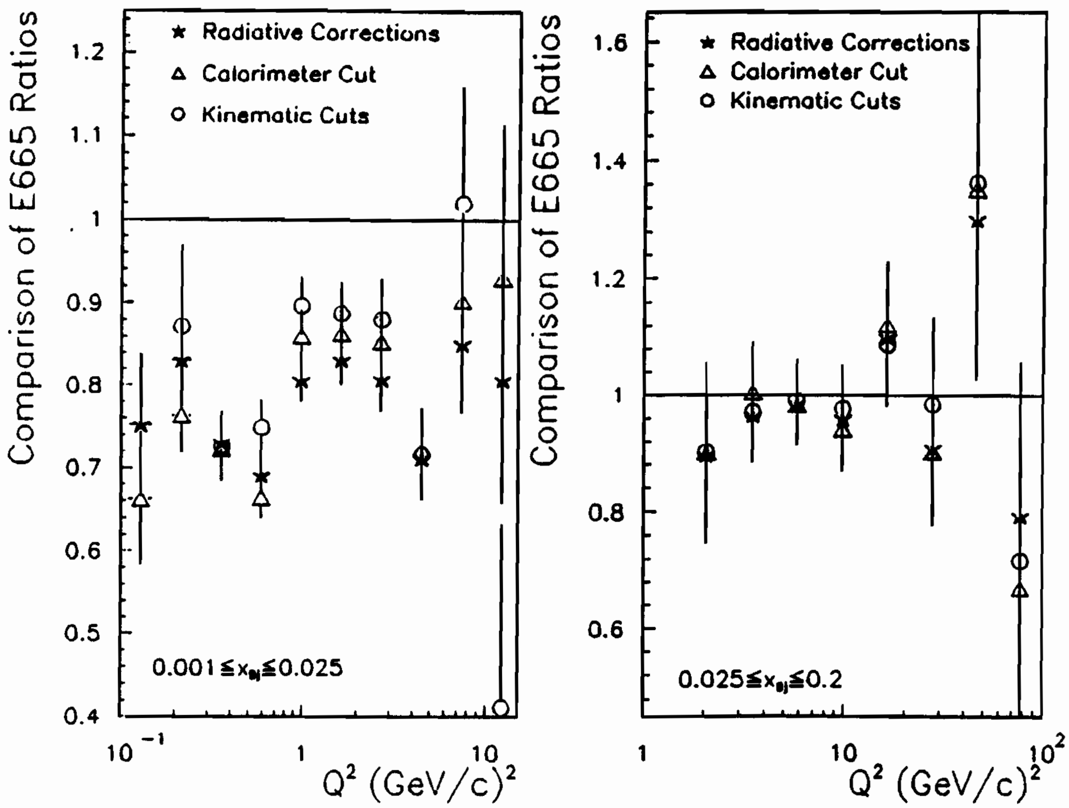

Figure 6.23: Comparison of cross section ratios for the 3 methods indicated as a function of Q^2.

correction ratio of a few percent. The reasons for this are not known, but some suggested explanations are :

1. Electromagnetic Calorimeter inefficiency. It is possible that there is a time dependence in the calorimeter efficiency. In this analysis, only the cathode pad readout is used, and this has been estimated to be > 99% efficient for recording the presence of photons. The response of the cathode pads was also monitored closely during the run and corrected for time variations. Also a possibility was that the calorimeter readout dropped out of the data acquisition. This was possible for events with a large number of words in the readout chain. This was also checked and found to be time independent to within 1%.

2. Bremsstrahlung photons from inelastic scatters. The calculated radiative corrections include contributions from inelastic events in which the beam or scattered muon radiate a

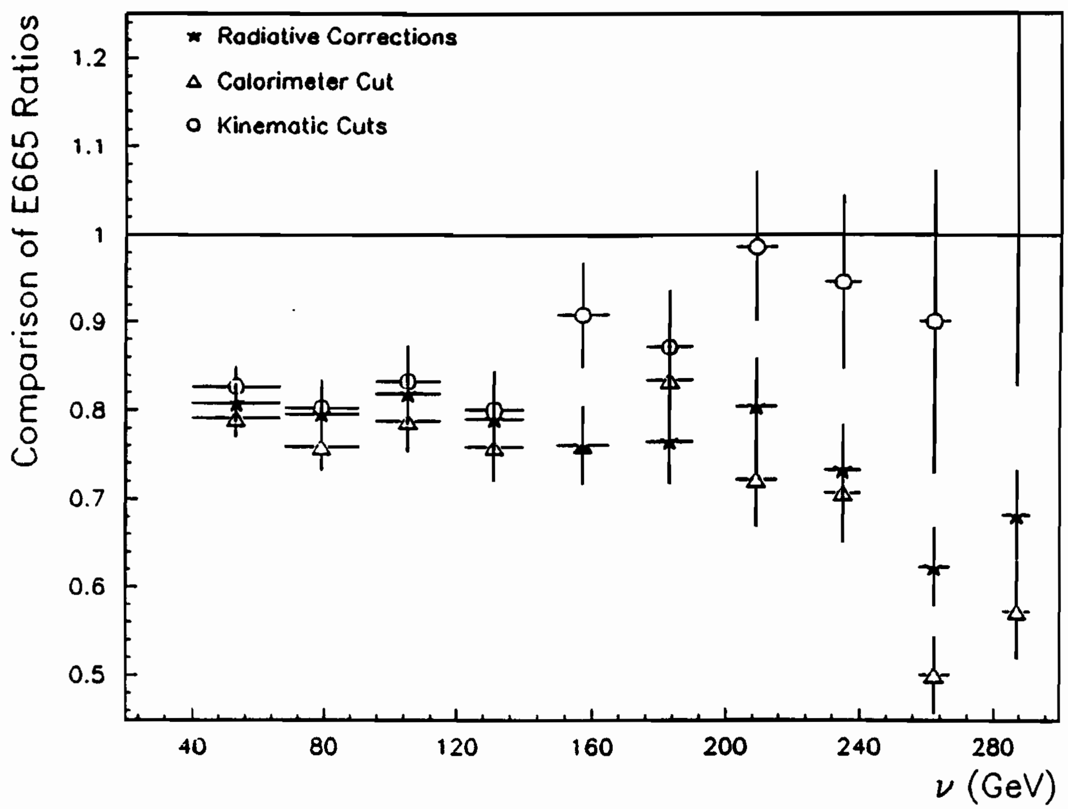

Figure 6.24: Comparison of cross section ratios for the 3 methods indicated as a function of ν.

photon. This type of event was not cut with the calorimeter so as to keep the DIS loss rate small (see Section 5.6). In principle, the contribution from these events should be approximately A independent since they only depend on the structure function F_2. Figure 5.17 shows the relative contribution of these events from the radiative correction calculation program. The measurement of F_2 for the xenon target is necessary to determine the relative correction due to these processes compared to deuterium.

3. Electromagnetic Calorimeter cut too conservative. Since the cross section ratio for the calorimeter cut is systematically higher than that from the radiative correction calculation, it may be that the E_{Cal}/ν ratio used to determine if events are to be cut is too high, or that the cluster requirement is too restrictive. As shown in Section 5.6, the value used was based on a fit of events selected for their high probability of being due to muon - nucleus bremsstrahlung and the cluster requirement was confirmed by checking

the number of tracks associated with the primary vertex. However, the coherent scattering bremsstrahlung events were most likely to result in a lower E_{Cal}/ν ratio since the high energy photon generated in such events saturated the charge collecting ability of the calorimeter, resulting in an underestimate of the energy contained in the detected photon. This problem can only be corrected by greater segmentation in the region in which these photons are seen.

The most likely explanation for the systematic difference is probably item 3, but to correct for this by lowering the E_{Cal}/ν ratio for the cut would introduce a greater DIS loss rate considered unacceptable for this analysis.

6.5 Tabulated Results

Tables XIII - XV contain the tabulated results of the fully corrected (including radiative corrections) cross section ratio as a function of each of the 3 kinematic variables x_{Bj}, Q^2, and ν. Also shown are the statistical and systematic errors for each point. For the x_{Bj} and ν results, average Q^2 values are reported, and for the Q^2 results, average x_{Bj} values are included.

TABLE XIII: σ_{Xe}/σ_{D_2} VERSUS x_{Bj}

x_{Bj} Dependence				
σ_{Xe}/σ_{D_2}	x_{Bj}	$< Q^2 >$	σ_{stat}	σ_{syst}
.639	.0013	.406	.021	.047
.680	.0021	.597	.025	.050
.748	.0035	.861	.028	.055
.780	.0060	1.310	.030	.058
.788	.0098	2.073	.032	.058
.844	.016	3.301	.039	.062
.946	.027	5.231	.050	.070
.950	.045	8.022	.060	.070
.940	.074	12.377	.075	.070
.926	.126	26.195	.103	.069

TABLE XIV: σ_{Xe}/σ_{D_2} VERSUS Q^2

Q^2 Dependence (.001 < x_{Bj} < .025)					**Q^2 Dependence (.025 < x_{Bj} < .2)**				
σ_{Xe}/σ_{D_2}	Q^2	$< x_{Bj} >$	σ_{stat}	σ_{syst}	σ_{Xe}/σ_{D_2}	Q^2	$< x_{Bj} >$	σ_{stat}	σ_{syst}
.752	.129	.0013	.087	.056	.898	2.04	.028	.152	.066
.831	.214	.0018	.048	.061	.965	3.47	.035	.081	.071
.731	.355	.0024	.030	.054	.985	5.75	.047	.070	.073
.691	.589	.0037	.023	.051	.961	9.77	.066	.073	.071
.807	.977	.0059	.027	.060	1.101	16.22	.088	.102	.081
.832	1.62	.0096	.032	.062	.909	27.54	.127	.125	.067
.808	2.69	.0120	.040	.060	1.303	45.71	.200	.277	.096
.712	4.47	.0139	.045	.053	.794	77.62	.237	.264	.059
.852	7.41	.0168	.086	.063	-	-	-	-	-
.808	12.30	.0203	.150	.060	-	-	-	-	-

TABLE XV: σ_{Xe}/σ_{D_2} VERSUS ν

ν Dependence				
σ_{Xe}/σ_{D_2}	ν	$< Q^2 >$	σ_{stat}	σ_{syst}
.808	53	.406	.022	.060
.796	79	.597	.028	.059
.819	105	.861	.035	.061
.790	131	1.310	.038	.058
.761	157	2.073	.043	.056
.765	183	3.301	.048	.057
.804	209	5.231	.055	.059
.733	235	8.022	.051	.054
.623	261	12.377	.045	.046
.682	287	26.195	.051	.050

7. COMPARISON OF RESULTS

The xenon/deuterium cross section ratios obtained in this analysis will be compared to other experimental results and to theoretical results where quantitative predictions have been made. Some experimental and theoretical results are expressed as ${F_2}^A/{F_2}^D$ (ratio of structure function per nucleon in a nuclear target compared to that in deuterium) instead of ratio of cross sections. By examining Equation 1.27 in Section 1.1, it follows that if $R = \sigma_L/\sigma_T$ is independent of A (as the best available evidence indicates [30]), then $\sigma_A/\sigma_D \equiv {F_2}^A/{F_2}^D$ and direct comparisons are possible. Also, the ratio A^{eff}/A is an equivalent way of expressing the ratio of cross sections per nucleon, and will therefore be compared directly.

7.1 Comparison with Other Experiments

For direct comparison, the NA28 (EMC Collaboration) experiment is the closest in apparatus design and experimental technique to E665. The method of triggering [7] was very much like the SAT described in Chapter 3. The kinematic ranges in x_{Bj} and Q^2 were very similar in both experiments, with the NA28 region being a subset of the E665 range.

The EMC Collaboration also examined the ratio of structure functions in tin ($A = 118$) compared to deuterium for an x_{Bj} range which substantially overlaps with NA28 and E665, but at Q^2 values higher than those obtained in NA28. Figure 7.1 shows these results compared to the E665 xenon/deuterium ratio as a function of x_{Bj}.

The progression of the EMC results shows stronger shadowing as a function of A. From these

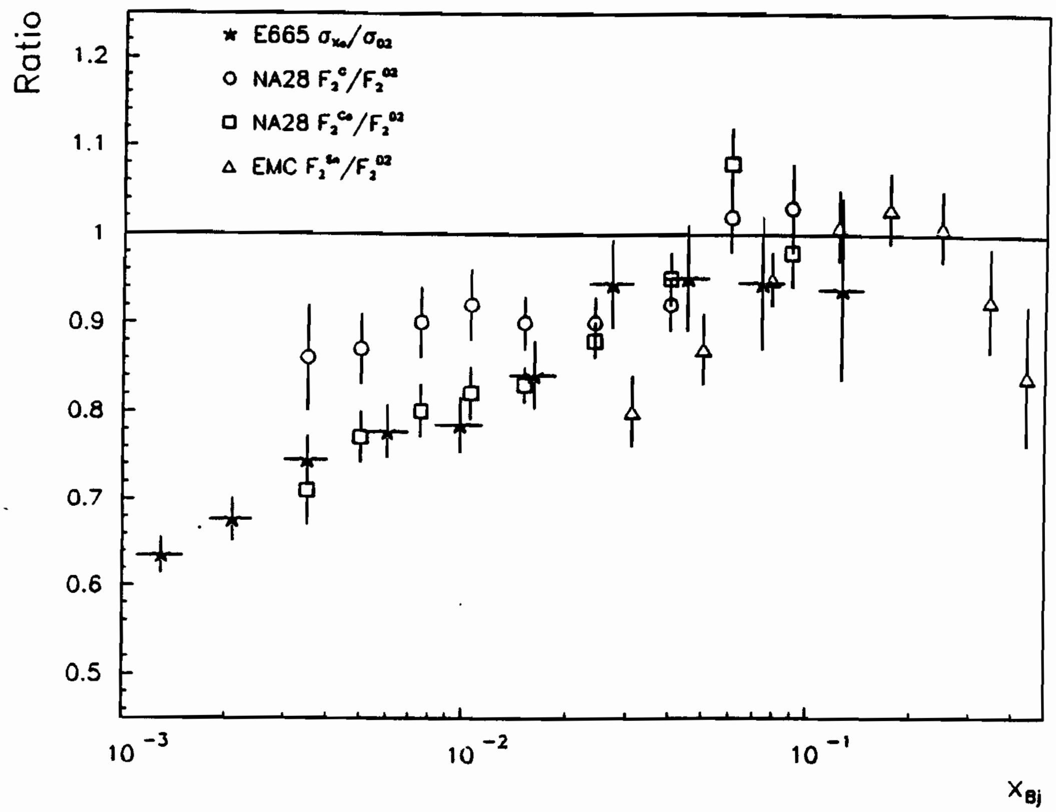

Figure 7.1: Comparison of E665 σ_{Xe}/σ_{D2} results to NA28 ${F_2}^A/{F_2}^D$ results for carbon and calcium and EMC results for ${F_2}^{Sn}/{F_2}^D$.

results, it is expected that the E665 xenon results should closely match those of EMC tin. However, Figure 7.1 shows that the E665 results more closely match the NA28 calcium/deuterium ratio. A possible source of this discrepancy could be the systematic errors quoted for each of the results; NA28 quotes a 7% systematic error on the normalization, and EMC reports a 5% total systematic error. Taking the systematic error for this analysis of $\sim$ 7%, the ratios can be rearranged to show a consistent A dependence. It must also be noted, however, that the tin/deuterium ratio does not agree with the A dependence shown by the carbon and calcium ratios when included in the same theoretical model.

Figure 7.2 shows the cross section ratio as a function of Q^2 in the two x_{Bj} regions for this analysis compared to the Q^2 dependence of the NA28 calcium/deuterium results.

A flat dependence on Q^2 is indicated for both results with the E665 ratio extending the

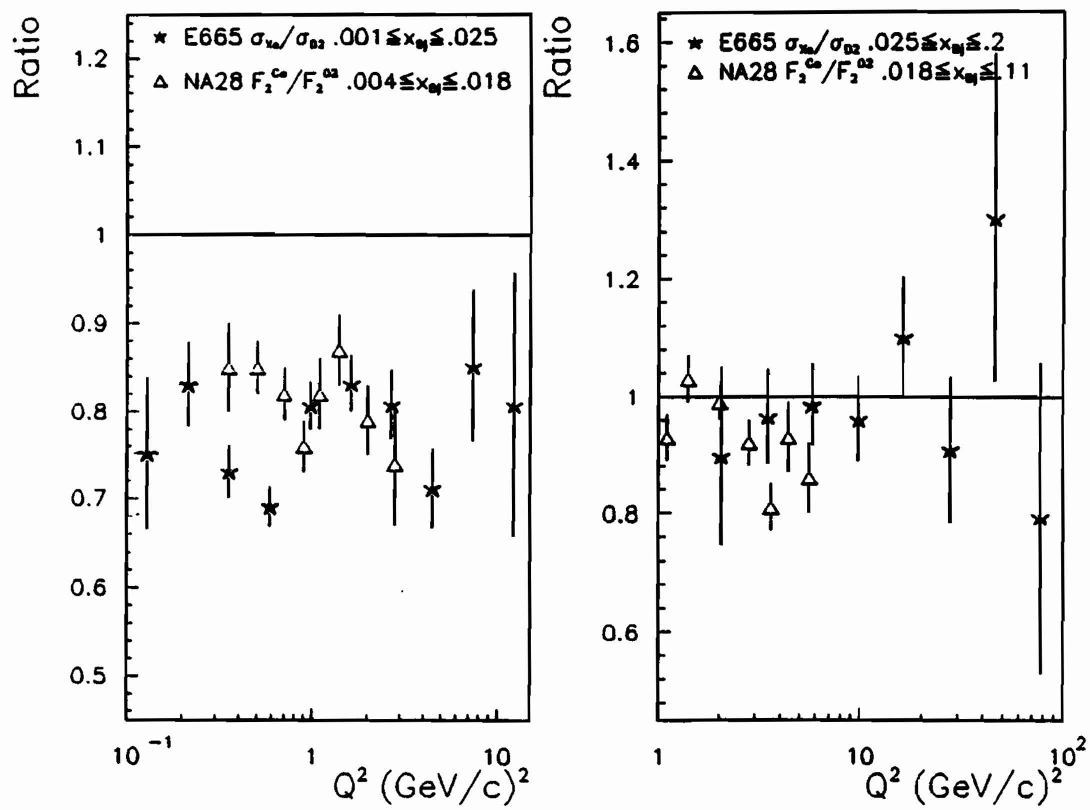

Figure 7.2: Comparison of E665 σ_{Xe}/σ_{D2} results to the NA28 ${F_2}^{Ca}/{F_2}^{D}$ results as a function of Q^2.

range in Q^2 over which this dependence is seen. From the low x_{Bj} range plot, it can be seen that shadowing persists for Q^2 values of up to 10 $(GeV/c)^2$.

The recent results from the Drell-Yan experiment E772 at FNAL also show shadowing as a function of x_t - the fraction of the target nucleon's momentum carried by the struck quark. The Drell-Yan process in the continuum region between the J/ψ and the Υ represents masses (analagous to Q in deep inelastic scattering) between 4 GeV and 8 GeV, or Q^2 values from $16 \rightarrow 64$ $(GeV/c)^2$. The lower limit on x_t is ~ 0.04 determined by the trigger acceptance. Figure 7.3 shows the results from E772 for ratios of calcium/deuterium, iron/deuterium ($A_{Fe} = 56$), and tungsten/deuterium ($A_W = 184$) event yields per nucleon as a function of x_t compared with the results from this analysis. The NA28 calcium/deuterium structure function ratio is also included as a direct comparison of like targets.

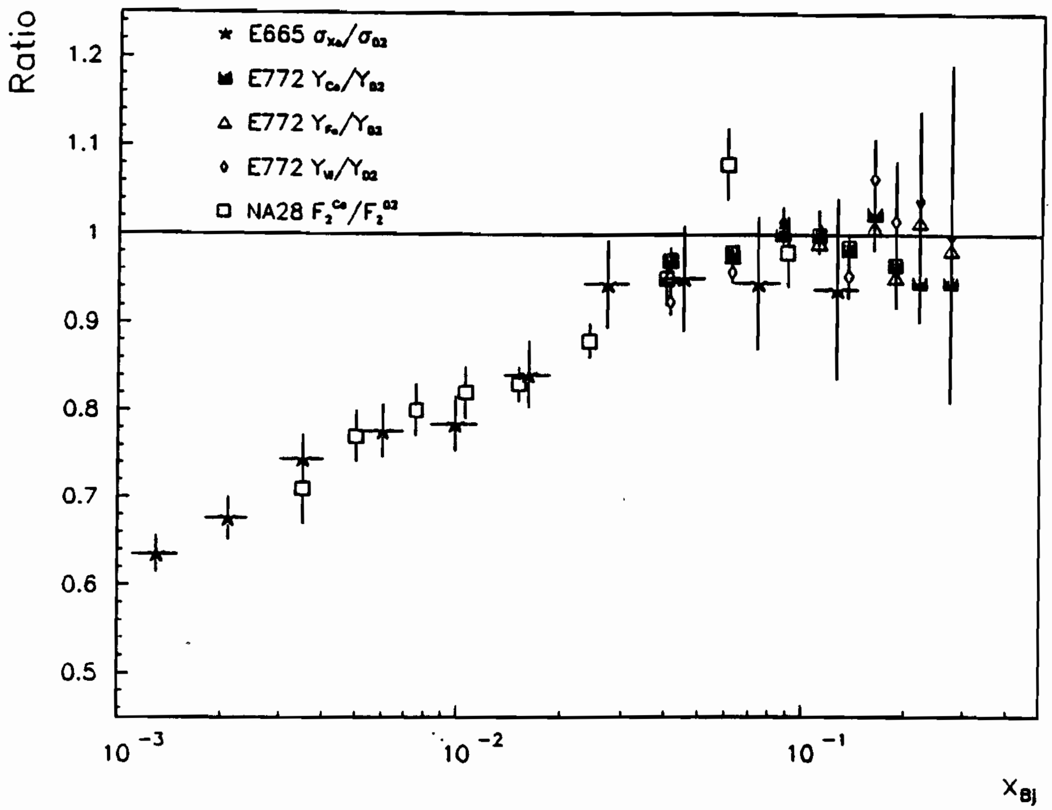

Figure 7.3: Comparison of E665 σ_{Xe}/σ_{D2} results to E772 Drell-Yan ratios of event yield per nucleon for calcium, iron, and tungsten. The NA28 ${F_2}^{Ca}/{F_2}^{D}$ result is also included.

The comparison of these results shows a consistent A dependence of shadowing among the 3 E772 targets represented, and the calcium/deuterium ratios of E772 and NA28 show fairly good agreement. The systematic error quoted on the E772 results is $< 2\%$. It must be remembered that the Q^2 values of the NA28 data $(0.3\ (GeV/c)^2 < Q^2 < 3.2\ (GeV/c)^2)$ do not overlap with the E772 $(\text{Mass})^2$ of $> 16\ GeV^2$. Therefore, the agreement of the two data sets in these two different kinematic ranges is further indication of the Q^2 independence of shadowing as seen in the NA28 and E665 data.

The final comparison with other experiments is to compare the ν dependence seen in the E665 xenon/deuterium cross section ratio with the ratio of A^{eff}/A seen in real photon scattering data. Figure 7.4 shows the ν dependence of carbon/deuterium, copper/deuterium ($A_{Cu} = 64$) and lead/deuterium ($A_{Pb} = 207$) from reference [23] along with the E665 xenon/deuterium ν

dependence.

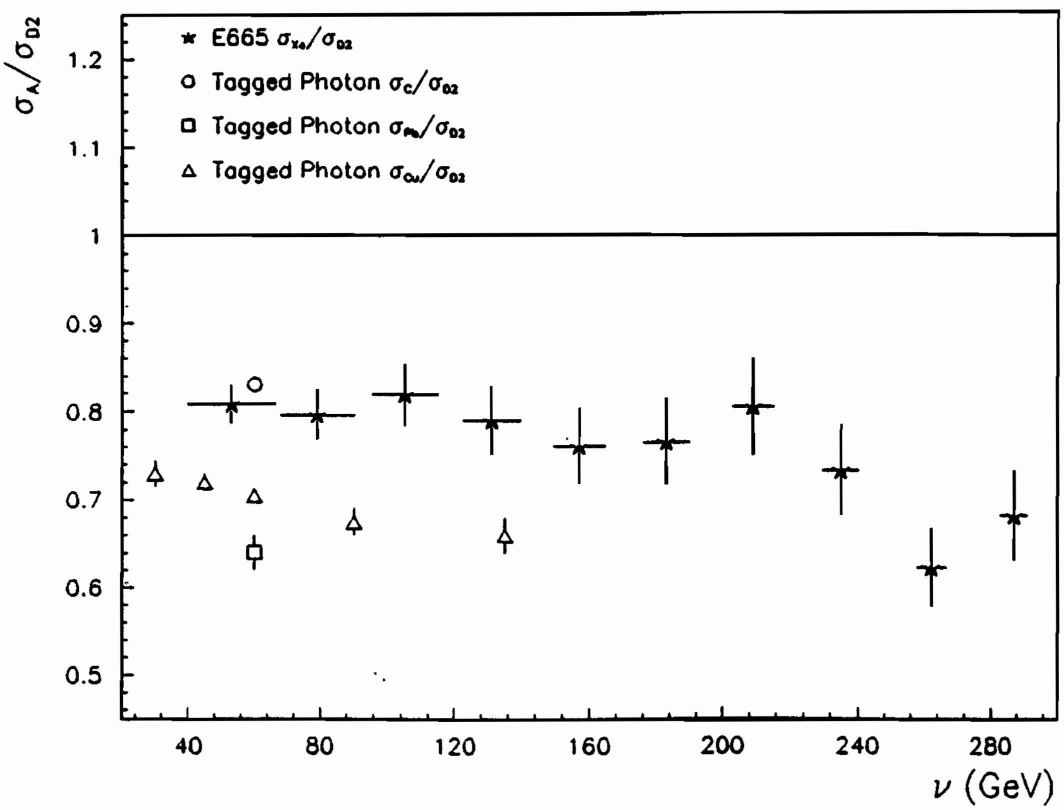

Figure 7.4: Comparison of E665 σ_{Xe}/σ_{D2} results to real photon results of A_{eff}/A for carbon, copper, and lead as a function of ν.

7.2 Comparison with Theoretical Models

The theoretical models used to explain shadowing are divided into two basic types as discussed previously; those which model the ratio of cross sections by vector dominance and its variations, and those which use some variation of parton recombination to explain the effect. While both types of models can explain the existence of shadowing at low x_{Bj} (or high ν), varying degrees of shadowing are predicted by the individual models in each category such that it is hard to distinguish between general types as opposed to individual models. However, the one item which separates the two general categories and can be used to give support to one or the other is the Q^2 dependence of the ratio. In the vector dominance models, the presence of Q^2 in the denominator of the energy difference between the photon and hadronic states eventually dominates the ratio, forcing shadowing to go away at high Q^2. The slope of the dependence can be modified by including increasingly heavy vector mesons, but the quantitative predictions of the resulting dependence on Q^2 show large variations in the shadowing signal as Q^2 changes. On the other hand, the parton recombination models can exist with a very slight or even non-existent Q^2 dependence which the recent data of NA28 [6], E772 [5], and now E665 show. It is seen in this study as well as in the individual experiments NA28 and E772 that the Q^2 dependence appears to be flat over the range $0.1(GeV/c)^2 < Q^2 < 30(GeV/c)^2$, agreeing with Qiu [53], who indicates a slight Q^2 dependence in this range. Figure 7.5 shows a comparison of this data with the results of Qiu's predictions.

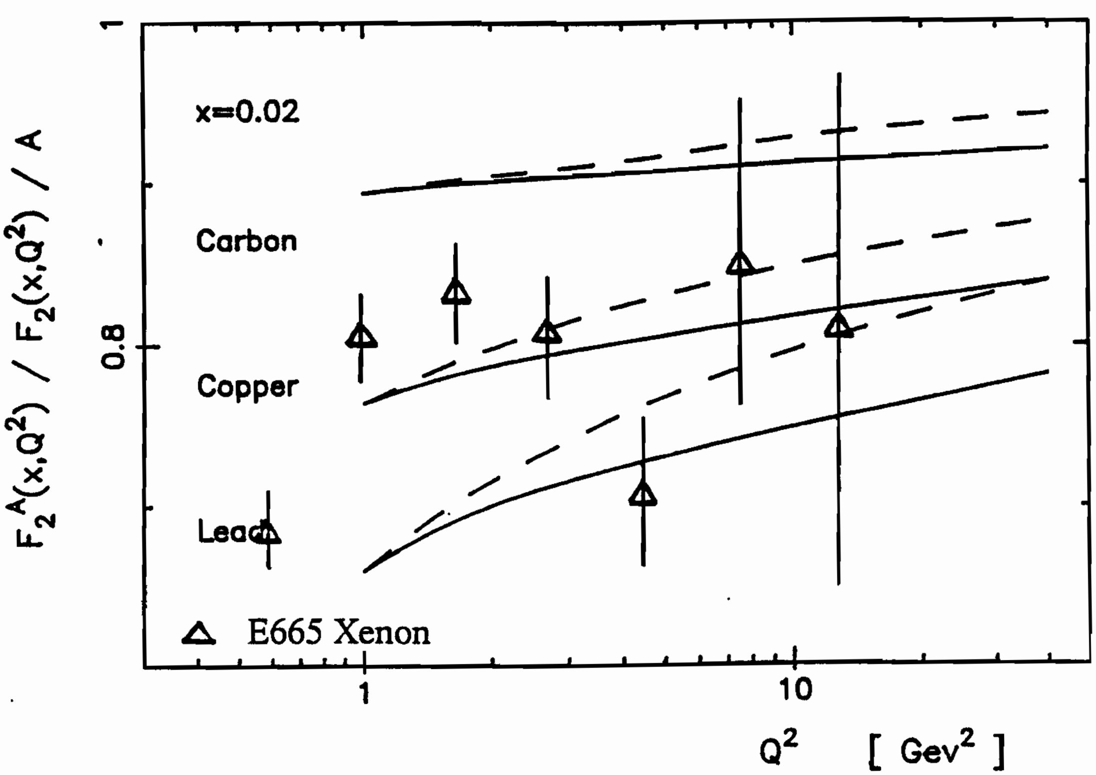

Figure 7.5: Comparison of the Q^2 dependence from a QCD shadowing model to the observed dependence of $\sigma_{Xe}/\sigma D2$.

8. CONCLUSIONS

This analysis featured the following items which were unique in this study of the low x_{Bj} structure of free nucleons compared to nucleons in nuclei :

- The highest muon beam momentum (490 GeV/c average) and virtual photon energy ($\nu = 350\ GeV$) in a DIS experiment.
- The lowest x_{Bj} (0.001) reached in a DIS experiment.
- The largest Q^2 range ($0.1 \rightarrow 50\ (GeV/c)^2$) in a DIS low x_{Bj} experiment.
- The use of xenon ($A_{Xe} = 131$) to provide bound nucleons.
- The use of both radiative correction calculations and electromagnetic calorimetry to correct for the presence of radiative background for the first time in a low x_{Bj} cross section ratio measurement.

The results of this analysis qualitatively confirm previous results from various nuclear targets and probes. The presence of shadowing at low x_{Bj} is seen. No evidence for saturation of the shadowing effect down to $x_{Bj} = 0.001$ is seen in this analysis of σ_{Xe}/σ_{D_2}. In addition, by studying the ratio dependence on different kinematic variables, it has been determined that the dependence of the ratio of cross sections on the scaling variable x_{Bj} is the natural way to model shadowing. The Q^2 dependence at fixed x_{Bj} shows that shadowing does not disappear as Q^2 increases which is contrary to vector dominance models. In fact, this analysis shows that the lack of Q^2 dependence is consistent with Qiu's model [53] which predicts a flat Q^2 dependence at fixed x_{Bj}. Also, the recent Drell-Yan shadowing results support the lack of Q^2 dependence when the calcium results at high Q^2 are compared to the NA28 results at $Q^2 \sim 1(GeV/c)^2$. The ν dependence of the ratio (at all Q^2 since no Q^2 dependence is seen) also indicates that the naive vector dominance model (or ρ dominance) is also not consistent with the data. It is possible that more recent generalized vector dominance models are consistent with the observed ν dependence, but as shown in Section 7.2, these models are not consistent with the data as a function of Q^2.

All of the above observations point to a parton model approach to explain shadowing in nuclear targets. The x_{Bj} dependence of the ratio as seen in this analysis can be explained by the sea quark and gluon recombination models as suggested by Mueller and Qui [51]. While some of the features of the ratio dependence can not be determined from this analysis, such as the onset of shadowing or the presence of anti-shadowing, the x_{Bj} dependence and Q^2 dependence at fixed x_{Bj} strongly suggest that the recombination model and resultant modified Altarelli-Parisi evolution equations can explain the observed features of shadowing. Several variations of this model, i.e. those of Brodsky and Lu [22], Frankfurt and Strikman [36], and Zhu and Shen [59], also can explain some features of this data, and can not be ruled out as competing explanations.

The common feature which is the basis for all of the theoretical models describing shadowing in nuclei is the size of the probe and/or the scattering region. The transverse size ($\propto Q$) is a property of the virtual photon probe and as such is associated with vector dominance models which treat the photon as an object with structure. The longitudinal size ($\propto x_{Bj}$) is a property of the nucleon in its free and bound states, the effects of this size becoming evident when nucleons are packed in a nucleus. Therefore, x_{Bj} dependent shadowing indicates that low x_{Bj} partons extend well beyond the size of a nucleon, belonging, instead to the nucleus. This, in itself, does not explain the effect of reduced parton distributions per nucleon, but it does provide a means to allow a mechanism such as parton recombination to occur.

In summary, the results of this analysis support the description of the phenomenon of shadowing as a partonic effect. The parton distributions (for gluons and sea quarks) at low

x_{BJ} appear to be modified when the nucleons containing these partons are bound in a nucleus. The net effect of parton recombination would effectively reduce the total number of partons in nuclei per nucleon at low x_{Bj}, and the modified Altarelli-Parisi evolution equations, which include recombination effects, predict the very weak Q^2 dependence. If vector dominance plays a role in the shadowing phenomenon observed in this Q^2 and x_{Bj} region, it appears to be dominated itself by the reduced parton distributions per nucleon in nuclei.

CITED LITERATURE

[1] Adams, M.R., Aid, S., Anthony, P.L., Baker, M.D., Bartlett, J.F., Bhatti, A.A., Braun, H.M., Burnett, T., Busza, W., Conrad, J.M., Coutrakon, G.B., Davisson, R., Dhawan, S.K., Dougherty, W., Dreyer, T., Ecker, U. Eckardt, V., Erdmann, M., Eskreys, A., Eskreys, K., Gebauer, H.J., Geesaman, D.F., Gilman, R., Green, M.C., Haas, J., Halliwell, C., Hanlon, J., Hughes, V.W., Jackson, H.E., Jansen, D.M., Jansco, G., Kaufman, S., Kennedy, R.D., Kirk, T., Kobrak, H., Krzywdzinski, S., Kunori, S., Lord, J., Lubatti, H.J., Lyons, T., Magill, S., Malecki, P., Manz, A., McLeod, D., Melanson, H., Michael, D.G., Mohr, W., Montgomery, H.E., Morfin, J.G., Nickerson, R.B., O'Day, S., Osborne, A.M., Osborne, L., Pawlik, B., Pipkin, F. M., Ramberg, E.J., Roser, A., Ryan, J., Salvarani, A., Schmitt, M., Schuler, K.P., Sexton, E., Seyerlein, H.J., Skuja, A., Soldner-Rembold, S., Steinberg, P.H., Stier, H.E., Stopa, P., Strube, P., Swanson, Robert A., Talaga, R.L., Tentindo-Repond, S., Trost, H.-J., Venkataramania, H., Vidal, M., Wilhelm, M., Wilkes, J., Wilson, Richard, Wolbers, S., and Zhao, T., Nucl. Instrum. Methods A291:533, 1990.

[2] Adams, M., *SAT MWPC's*, E665 Internal Report BT020, July 1986.

[3] Aid, S., Cole, J., Kunori, S., O'Day, S., Ramberg, E., Rapp, P., Skuja, A., Snow, G., Steinberg, P., Talaga, R., Conrad, J., Michael, D., Nickerson, R. Pipkin, F., Schmitt, M., Williams, H., and Wilson, R., *An Electromagnetic Calorimeter for E665*, In Proceedings of the Gas Sampling Calorimetry Workshop II, Fermilab, 1985.

[4] Akhundov, A.A., Bardin, D.Yu., and Shumeiko, N.M., JINR E2:10147, 1976.

[5] Alde, D.M., Baer, H.W., Carey, T.A., Garvey, G.T., Klein, A., Lee, C., Leitch, J., Lillberg, J.W., McGaughey, P.L., Mishra, C.S., Moss, J.M., Peng, J.C., Brown, C.N., Cooper, W.E., Hsiung, Y.B., Adams, M.R., Guo, R., Kaplan, D.M., McCarthy, R.L., Danner, G., Wang, M.J., Barlett, M.L., and Hoffman, G.W., Phys. Rev. Lett. 64:2479, 1990.

[6] Arneodo, M., Arvidson, A., Aubert, J.J., Badelek, B., Beaufays, J., Bee, C.P., Benchouk, C., Berghoff, G., Bird, I., Blum, D., Bohm, E., de Bouard, X., Brasse, F.W., Braun, H., Broll, C., Brown, S., Bruck, H., Brull, A., Calen, H., Chima, J.S., Ciborowski, J., Clifft, R., Coignet, G., Combley, F., Coughlan, J., D'Agostini, G., Dahlgren, S., Dengler, F., Derado, I., Dreyer, T., Drees, J., Drobnitzki, M., Duren, M., Eckardt, V., Edwards, A., Edwards, M., Ernst, T., Eszes, G., Favier, J., Ferrero, M.I., Figiel, J., Foster, J., Ftacnik, J., Gabathuler, E., Gajewski, J., Gamet, R., Geddes, N., Grafstrom, P., Gustafsson, L., Haas, J., Hagberg, E., Hasert, F.J., Hayman, P., Heusse, P., Jaffre, M., Jacholkowska, A., Janata, F., Jancso, G., Johnson, A.S., Kabuss, E.M., Kaiser, R., Kellner, G., Kruger, A., Kruger, J., Kullander, S., Landgraf, U., Lanske, D., Loken, J., Long, K., Maire, M., Malecki, P., Manz, A., Maselli, S., Mohr, W., Montanet, F., Montgomery, H.E., Nagy,

E., Nassalski, J., Norton, P.R., Oakham, F.G., Osborne, A.M., Pascaud, C., Pawlik, B., Payre, P., Peroni, C., Peschel, H., Pessard, H., Pettingale, J., Pietrzyk, B., Pietrzyk, U., Pousgen, B., Potsch, M., Renton, P., Ribarics, P., Rith, K., Rondio, E., Sandacz, A., Scheer, M., Schlagbohmer, A., Schiemann, H., Schmitz, N., Schneegans, M., Scholz, M., Schroder, T., Schultze, K., Seidel, A., Sloan, T., Stier, H.E., Studt, M., Taylor, G.N., Thenard, J.M., Thompson, J.C., De La Torre, A., Toth, J., Urban, L., Wallucks, W., Whalley, M., Wheeler, S., Williams, W.S.C., Wimpenny, S.J., Windmolders, R., Wolf, G., and Ziemons, K., Phys. Lett. B211:493, 1988.

[7] Arvidson, A., Badelek, B., Calen, H., Dahlgren, S., Dobinson, R., Grafstrom, P., Gustafsson, L., Hagberg, E., Kullander, S., and Watson, E., Nucl. Instrum. Methods A251:437, 1986.

[8] Arvidson, A., Badelek, B., Calen, H., Dahlgren, S., Grafstrom, P., Gustafsson, L., Hagberg, E., Kabuss, E.M., and Kullander, S., Uppsala University Preprint ISV-PH 2/87, April 1987.

[9] Ashman, J., Badelek, B., Baum, G., Beaufays, J., Bee, C.P., Benchouk, C., Bird, I.G., Brown, S.C., Caputo, M.C., Cheung, H.W.K., Chima, J., Ciborowski, J., Clifft, R.W., Coignet, G., Combley, F., Court, G., D'Agostini, G., Drees, J., Duren, M., Dyce, N., Edwards, A.W., Edwards, M., Ernst, T., Ferrero, M.I., Francis, D., Gabathuler, E., Gajewski, J., Gamet, R., Gibson, V., Gillies, J., Grafstrom, P., Hagberg, E., Hamacher, K., Harrach, D.V., Hayman, P., Holt, J.R., Hughes, V.W., Jacholkowska, A., Jones, T., Kabuss, E.M., Korzen, B., Kruner, U., Kullander, S., Landgraf, U., Lanske, D., Lettenstrom, F., Lindqvist, T., Matthews, M., Mizuno, Y., Monig, K., Montanet, F., Nassalski, J., Niinikoski, T., Norton, P.R., Oakham, G., Oppenheim, R.F., Osborne, A.M., Papavassiliou, V., Pavel, N., Peroni, C., Peschel, H., Piegaia, R., Pietrzyk, B., Pietrzyk, U., Povh, B., Renton, P., Rieubland, J.M., Rith, K., Rondio, E., Ropelewski, L., Salmon, D., Sandacz, A., Scheer, M., Schroder, T., Schuler, K.P., Schultze, K., Shibata, T.-A., Sloan, T., Staiano, A., Stier, H.E., Stock, J., Taylor, G.N., Thompson, J.C., Walcher, T., Wheeler, S., Williams, W.S.C., Wimpenny, S.J., Windmolders, R., and Womersley, W.J., Phys. Lett. B202:603, 1988.

[10] Aubert, J.J., Bassompierre, G., Becks, K.H., Best, C., Bohm, E., de Bouard, X., Brasse, F.W., Broll, C., Brown, S., Carr, J., Clifft, R.W., Cobb, J.H., Coignet, G., Combley, F., Court, G.R., D'Agostini, G., Dau, W.D., Davies, J.K., Declais, Y., Dobinson, R.W., Dosselli, U., Drees, J., Edwards, A.W., Edwards, M., Favier, J., Ferrero, M.I., Flauger, W., Gabathuler, E., Gamet, R., Gayler, J., Gerhardt, V., Gossling, C., Haas, J., Hamacher, K., Hayman, P., Henckes, M., Korbel, V., Landgraf, U., Leenen, M., Maire, M., Minssieux, H., Mohr, W., Montgomery, H.E., Moser, K., Mount, R.P., Norton, P.R., McNicholas, J., Osborne, A.M., Payre, P., Peroni, C., Pessard, H., Pietrzyk, U., Rith, K., Schneegans, M., Sloan, T., Stier, H.E., Stockhausen, W., Thenard, J.M., Thompson, J.C., Urban, L., Villers, M., Wahlen, H., Whalley, M., Williams, D., Williams, W.S.C., Williamson, J., and Wimpenny, S.J., Phys. Lett. 123B:275, 1983.

[11] Bailey, J., Botterill, D.R., Montgomery, H.E., Norton, P.R., Del Guerra, A., Giazotto, A., Giorgi, M.A., and Stefanini, A., Nucl. Phys. B151:367, 1979.

[12] Benvenuti, A.C., Bollini, D., Bruni, G., Navarria, F.L., Lohmann, W., Voss, R., Genchev, V.I., Krivokhizhin, V.G., Lednicky, R., Nemecek, S., Savin, I.A., Smirnov, G.I., Sultanov, G., Meyer-Berkhout, U., Staude, A., Teichert, K.-M., Zupancic, C., Milsztajn, A., Ouraou, A., Smadja, G., and Virchaux, M., Phys. Lett. B237:599, 1990.

[13] Benvenuti, A.C., Bollini, D., Bruni, G., Navarria, F.L., Argento, A., Lohmann, W., Piemontese, L., Strachota, J., Zavada, P., Baranov, S., Genchev, V.I., Golutvin, I.A., Kiryushin, Yu.T., Krivokhizhin, V.G., Kukhtin, V.V., Lednicky, R., Nemecek, S., Reimer, P., Savin, I.A., Telyukov, E., Smirnov, G.I., Sultanov, G., Todorov, P., Volodko, A.G.,

Jamnik, D., Kopp, R., Meyer-Berkhout, U., Staude, A., Teichert, K.-M., Tirler, R., Voss, R., Zupancic, C., Cribier, M., Feltesse, J., Milsztajn, A., Ouraou, A., Sacquin, Y., Smadja, G., and Virchaux, M., Phys. Lett. B237:592, 1990.

[14] Berger, Edmond L., and Qiu, Jianwei, In Proc. of Topical Conf. on Nucl. Chromodynamics, eds. J. Qiu and D. Sivers, pp. 119-129, Singapore, World Scientific Publishing Co., 1988.

[15] Bhatti, A., Burnett, T., Davisson, R., Jansen, D., Krzywdzinski, S., Lord, J., Lubatti, H., Rees, D., Wilkes, J., and Zieber, G., *Seattle MWPC System (PCF Detector)*, E665 Internal Report FS011, 1985.

[16] Bilchak, C.L., Schildknecht, D., and Stroughair, J.D., Phys. Lett. B214:441, 1988.

[17] Bilchak, C.L., Schildknecht, D., and Stroughair, J.D., Phys. Lett. B233:461, 1989.

[18] Bjorken, J.D., Phys. Rev. 179:1547, 1969.

[19] Bjorken, J.D., and Paschos, E.A., Phys. Rev. 185:1975, 1969.

[20] Bloom, E.D., Coward, D.H., DeStaebler, H., Drees, J., Miller, G., Mo, L.W., Taylor, R.E., Breidenbach, M., Friedman, J.I., Hartmann, G.C., and Kendall, H.W., Phys. Rev. Lett. 23:930, 1969.

[21] Breidenbach, M., Friedman, J.I., Kendall, H.W., Bloom, E.D., Coward, D.H., DeStaebler, H., Drees, J., Mo, L.W., and Taylor, R.E., Phys. Rev. Lett. 23:935, 1969.

[22] Brodsky, Stanley J., and Lu, Hung Jung, Phys. Rev. Lett. 64:1342, 1990.

[23] Caldwell, D.O., Elings, V.B., Hesse, W.P., Morrison, R.J., Murphy, F.V., and Yount, D.E., Phys. Rev. D7:1362, 1973.

[24] Caldwell, D.O., Cumalat, J.P., Eisner, A.M., Lu, A., Morrison, R.J., Murphy, F.V., Yellin, S.J., Davis, P.J., Donnelly, M.G., Egloff, R.M., Luste, G.J., Martin, J.F., Prentice, J.D., and Nash, T., Phys. Rev. Lett., 42:553, 1979.

[25] Castorina, P., and Donnachie, A., Phys. Lett. B215:589, 1988.

[26] Castorina, P., and Donnachie, A., Z. Phys. C45:141, 1989.

[27] Close, F.E., and Roberts, R.G., Phys. Lett. B213:91, 1988.

[28] Close, Frank E., Qiu, Jianwei, and Roberts, R.G., Phys. Rev. D40:2820, 1989.

[29] Collins, John, and Kwiecinski, Jan, Nucl. Phys. B335:89, 1990.

[30] Dasu, S., de Barbaro, P., Bodek, A., Harada, H., Krasny, M.W., Lang, K., Riordan, E.M., Arnold, R., Benton, D., Bosted, P., Clogher, L., deChambrier, G., Lung, A., Rock, S.E., Szalata, Z.M., Walker, R.C., Filippone, B.W., Jourdan, J., Milner, R., McKeown, R., Potterveld, D., Para, A., Dietrich, F., Van Bibber, K., Button-Shafer, J., Debebe, B., Hicks, R.S., Gearhart, R., Whitlow, L.W., and Alster, J., Phys. Rev. Lett. 61:1061, 1988.

[31] DePalma, M., Favuzzi, C., Maggi, G., Ranieri, A., Selvaggi, G., Spinelli, P., Gebauer, H.J., Fent, J., Freund, P., Seyboth, J., and Seyerlein, J., Nucl. Instrum. Methods 217:135, 1983.

[32] Ditzler, W.R., Breidenbach, M., Friedman, J.I., Kendall, H.W., Poucher, J.S., Bloom, E.D., Cottrell, R.L.A., Coward, D.H., DeStaebler, H., Jordan, C.L., Piel, H., and Taylor, R.E., Phys. Lett. 57B:201, 1975.

[33] Eickmeyer, J., Michalowski, S., Mistry, N., Talman, R., and Ueno, K., Phys. Rev. Lett., 36:289, 1976.

[34] Fenker, H., *A Standard Beam PWC for Fermilab*, Technical Report TM-1179 2557.000, Fermilab, February 1983.

[35] Feynman, R.P., *The Behavior of Hadron Collisions at Extreme Energies*, In Proc. 3^{rd} Topical Conference on High Energy Collisions, eds. Yang, C.N., Cole, J.A., Good, M., Hwa, R., and Lee-Franzini, J., New York, Gordon and Breach, pp. 237-258, 1969.

[36] Frankfurt, L.L., and Strikman, M.I., Nucl. Phys. B316:340, 1989.

[37] Franz, J., Guzielski, G., Huber, G., Mecklenbrauck, G., Mecklenbrauck, W., Rossle, E., Glawe, U., Strohbusch, U., Johnsson, B., Jonsson, G.G., and Petersson, R., Z. Phys. C10:105, 1981.

[38] Gebauer, H.J., *The Vertex Proportional Chamber PCV*, E665 Internal Report VS012, October 1985.

[39] Gell-Mann, M., Phys. Lett. 8:214, 1964.

[40] Goodman, M.S., Hall, M., Loomis, W.A., Pipkin, F.M., Wilson, R., Thornton, R.K., Hicks, R., Kirk, T., Macallister, J., Quirk, T., Wright, S.C., Brandenburg, G., Young, C., Francis, W.R., and Kostoulas, I., Phys. Rev. Lett. 47:293, 1981.

[41] Grammer, Garland Jr., and Sullivan, Jeremiah D., In Electromagnetic Interactions of Hadrons, eds. A. Donnachie and G. Shaw, New York, Plenum Press, pp. 195-352, 1977.

[42] Gribov, L.V., Levin, E.M., and Ryskin, M.G., Phys. Rep. 100C:1, 1983.

[43] Lietzke, C. and Wimpenny, S.J., University of California Preprint UCR/DIS-89-06, Sept. 1989.

[44] Malensek, A., and Morfin, J.G., *The Tevatron Muon Beam : A High Intensity Beam with Well Defined Polarization*, Technical Report TM1193 2966.00, Fermilab, July 1983.

[45] May, M., Aslanides, E., Lederman, L., Limon, P., Rapp, P., Entenberg, A., Jostlein, H., Kim, I.J., Konigsman, K., Kostoulas, I.G., Melissinos, A.C., Gittleson, H., Kirk, T., Murtagh, M., Tannenbaum, M.J., Sculli, J., White, T., and Yamanouchi, T., Phys. Rev. Lett. 35:407, 1975.

[46] Melanson , H., Kirk, T., and Wolbers, S., *Fermilab Drift Chamber System*, E665 Internal Report FS010, 1985.

[47] Miller, M., Moskowitz, B., LeBritton, J., McCal, D., Metcalf, W., Melissinos, A.C., Alspector, J., Borenstein, S., Kalbfleisch, G.R., Sharanguivel, J., Strand, R.C., and Abashian, A., Phys. Rev. D24:1, 1981.

[48] Montgomery, H.E., *Beam Tagging for E665*, E665 Internal Report BT007, July 1984.

[49] Mo, L.W., and Tsai, Y.S., Rev. Mod. Phys. 41:205, 1969.

[50] Morfin, J.G., and Tung, W.K., ***Parton Distributions from a Global QCD Analysis of Deep Inelastic Scattering and Lepton-Pair Production***, Fermilab Preprint FERMILAB-Pub-90/74, April 1990.

[51] Mueller, A.H., and Qiu, J.,Nucl. Phys. B268:427, 1986.

[52] Nicolaev, N.N., and Zakharov, V.I., Phys. Lett. 55B:397, 1975.

[53] Qiu, Jianwei, Nucl. Phys. B291:746, 1987.

[54] Ramberg, Erik J., ***Data Correction, Calibration and Resolution of the Calorimeter***, E665 Internal Report AN061, February 1990.

[55] Schmitt, Michael, ***Using the Calorimeter to Remove Electromagnetic Background***, E665 Internal Report AN058, November 1989.

[56] Shaw, G., Phys. Lett. B228:125, 1989.

[57] Stodolsky, L., Phys. Rev. Lett. 18:135, 1967.

[58] Tsai, Y.S., SLAC-PUB-848, 1971.

[59] Zhu, W., and Shen, J.G., Phys. Lett. B235:170, 1990.

VITA

NAME:	Stephen Magill
EDUCATION:	B.S., Physics, University of Maryland, College Park, Maryland, 1976
	M.S., Physics, DePaul University, Chicago, Illinois, 1979
	Ph.D., Physics, University of Illinois at Chicago, Chicago, Illinois, 1990
WORK EXPERIENCE:	Assistant Engineer, Argonne National Laboratory, 9700 South Cass Avenue, Argonne, Illinois, 1979-1982
CONFERENCE PRESENTATIONS:	Magill, S.R., Xe/D_2 Cross Section Ratios at Low x_{Bj} from Muon Scattering at 490 GeV/c, DPF90 - Rice University, 04-Jan-1990
	Magill, S.R., Xe/D_2 Cross Section Ratios at Low x_{Bj} from Muon Scattering at 490 GeV/c, APS General Meeting - Washington, D.C., 16-Apr-1990
PUBLICATIONS:	M. R. Adams et al., A Spectrometer for Muon Scattering at the Tevatron, Nucl. Instrum. Methods, 23:848, 1990
	Norem, J.H., et al., The Argonne Plasma Engineering Experiment (APEX) Tokamak, Nucl. Instrum. Methods, 198, 1-47, 1982
	Romero, J.B., et al., Nuclear Activation Techniques for Wall Material Transport Measurements in Tokamaks, Nucl. Instrum. Methods, 198, 425-431, 1982